Thermal transport in porous composite phase change materials

By

Shuai Zhang

Thesis submitted to the University of Nottingham for the degree of
Doctor of Philosophy

February 2023

Abstract

Inorganic salts are widely used medium- and high-temperature phase change materials (PCM). However, their thermal conductivity is low, and since salts are highly corrosive, many conventional heat transfer enhancement methods do not apply. In this research, the ceramic foam was used to enhance the heat transfer of salts. The ceramic foam is open-cell, and its pore size is large (~mm), which enables the natural convection of PCM and benefits thermal transport. And it is fabricated alone and is integrated with molten salt easily; hence, the foam and salt can be maintained separately (rather than the whole CPCM), and the maintenance cost is reduced. This research covers property measurement, material preparation, compatibility test, and performance analysis.

The thermo-physical properties of nitrate salts with various component fractions were measured. Mixing nitrate salts can decrease the melting point without impairing the latent heat; a molecular dynamics simulation was performed to provide microscopic insights.

The ceramic foam/salt composite phase change material (CPCM) with excellent compatibility was fabricated; the thermal transport in the porous CPCM was studied experimentally and numerically. The melting front is significantly curved, indicating natural convection is strong, which is attributed to the low viscosity of salts. The melting rate of the CPCM with a pore density of 10 PPI (Pores Per Inch) is increased by 51.5%, and the porosity has a more significant effect than pore density on the melting performance. For the shell-and-tube heat storage unit, the ceramic foam with varying outer diameters is optimal in melting rate, total stored energy, and energy storage rate. The thermal performance under solar fluctuation is also studied; strong solar radiation not only improves the energy storage rate but also increases the total stored energy; compared to pure PCM, ceramic foam/salt CPCM is more sensitive to solar fluctuation.

Acknowledgments

I would like to thank my supervisor, Prof. Yuying Yan. He provides great help with research direction and methodology. Without him, I could not have gotten into this research field. He is the guide in my way of research. I can still remember the scene we first met in 2018. It is my great luck to meet him. He also cares about my life and career a lot and manages to provide opportunities and support. I admire his enthusiasm and persistence in running. I also would like to thank my additional supervisor, Dr Mark Alston and internal examiner, Dr Jie Zhu for the guidance and suggestions.

I want to give thanks to Dr Yuanpeng Yao. He helped me a lot with the CFD simulation. We have many topics to talk about and it is a joyful time. I also appreciate Prof. Limei Tian who provides support in experiments. I am grateful to Ziyuan Li and Huan Wang. It is happy and unforgettable working with them. Finally, I would like to thank my wife and parents for their understanding and support.

Table of Contents

List of Publications

Journal publications

1. **S. Zhang**, D. Feng, L. Shi, L. Wang, Y. Jin, L. Tian, Z. Li, G. Wang, L. Zhao, Y. Yan, A review of phase change heat transfer in shape-stabilized phase change materials (ss-PCMs) based on porous supports for thermal energy storage, *Renewable and Sustainable Energy Reviews*, 135 (2021) 110127.
2. **S. Zhang**, Y. Yan, Melting and thermodynamic properties of nanoscale binary chloride salt as high-temperature energy storage material, *Case Studies in Thermal Engineering*, 25 (2021) 100973.
3. **S. Zhang**, Y. Jin, Y. Yan, Depression of melting point and latent heat of molten salts as inorganic phase change material: Size effect and mechanism, *Journal of Molecular Liquids*, 20 (2021) 117058.
4. **S. Zhang**, Z. Li, H. Wang, L. Tian, Y. Jin, M. Alston, Y. Yan, Component-dependent thermal properties of molten salt eutectics for solar thermal energy storage: experiments, molecular simulation and applications, *Applied Thermal Engineering*, (2022) 118333.
5. **S. Zhang**, Z. Li, Y. Yao, L. Tian, Y. Yan, Heat transfer characteristics and compatibility of molten salt/ceramic porous composite phase change material, *Nano Energy*, 100 (2022) 107476.
6. **S. Zhang**, Y. Yao, Y. Jin, Z. Shang, Y. Yan, Heat transfer characteristics of ceramic foam/molten salt composite phase change material (CPCM) for medium-temperature thermal energy storage, *International Journal of Heat and Mass Transfer*, 196 (2022) 123262.

7. **S. Zhang**, Y. Yan, Evaluation of discharging performance of molten salt/ceramic foam composite phase change material in a shell-and-tube latent heat thermal energy storage unit, *Renewable Energy*, 198 (2022) 1210-1223.
8. **S. Zhang**, H. Gao, Y. Yan, Atomic insights into melting behaviours of phase change material confined in nanospace, *Journal of Molecular Liquids*, 366 (2022) 120298.
9. **S. Zhang**, Y. Yan, Thermal performance of latent heat energy storage system with/without enhancement under solar fluctuation for Organic Rankine power cycle, *Energy Conversion and Management*, 270 (2022) 116276.
10. **S. Zhang**, Y. Yan, Energy, exergy and economic analysis of ceramic foam-enhanced molten salt as phase change material for medium- and high-temperature thermal energy storage, *Energy*, 262 (2023) 125462.

Conference papers

1. **S. Zhang**, Y. Yan, A molecular dynamics study on melting behaviour and size-dependent thermodynamic properties of nanoscale nitrate salts for thermal energy storage. *Sino-Japan-UK Frontiers in Phase Change Heat Transfer and Its Applications in Energy*, July 27-29, Xi'an, China, 2020.
2. Y. Yao, **S. Zhang**, Y. Yan, H. Wu, Boundary heat flux bifurcation for low Reynolds number fluid convection through high porosity open-cell metal foam, *17th UK Heat Transfer Conference*, April 4-6, Manchester, UK, 2022.

List of Figures

List of Tables

Chapter 1 - Introduction

1.1 Background

Currently, fossil fuels (coal, oil and gas) still dominate the global energy consumption. According to bp (The British Petroleum Company plc) statistics, fossil fuels have been accounting for over 80% of global primary energy consumption in the recent 20 years (Figure1.1). However, using renewable energy has more long-term benefits. Renewable energy is naturally replenished on a human timescale, removing the worry about exhaustion. And they are environmentally friendly and help cut CO_2 emissions to achieve net zero. Moreover, they are available within a nation and do not depend on imports from other nations, which is very important to national energy security. Nevertheless, some renewable energy sources, such as solar energy, have unsteady and intermittent nature, difficult to meet the practical requirement. To address the mismatch between heat supply and demand, thermal energy storage (TES) is proposed [1].

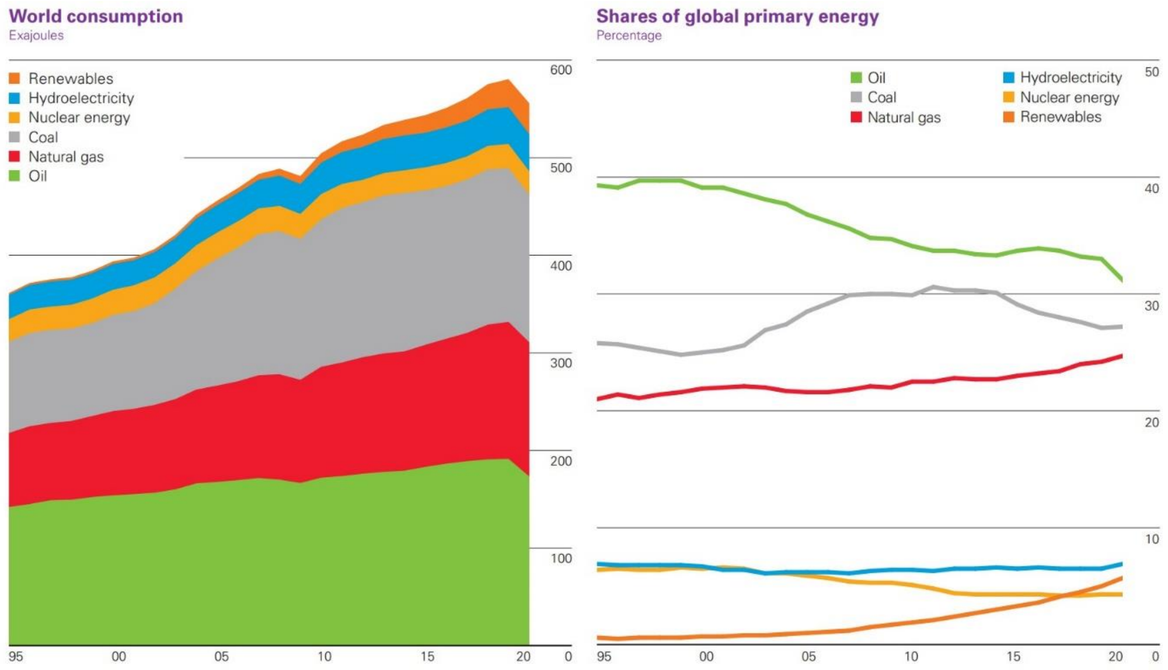

Figure 1.1: World energy consumption from 1995 to 2020 and shares of global primary energy [2].

1.2 Thermal energy storage

Burning fuels is a direct and convenient method to get heat, but it needs fuels, i.e. cost, and emits greenhouse gases. Utilizing free available thermal energy from renewable sources such as solar radiation and industrial activities has both economic and environmental benefits. TES technology stores heat or cold in the medium for a later use [3]. It addresses the following issues [4]:

- Time gap between thermal energy supply and consumption
- Distance between source of thermal energy and place of heat demand
- Fluctuation of heat sources

Additionally, in some regions, the price of electricity between peak and off-peak hours is different; TES stores heat/cold during off-peak hours and releases it during peak hours, shifting the electricity peak load and achieving economic savings [5]. Some typical TES applications are as follows.

- Domestic hot water supply. Solar heat is stored in a water tank for use in the evening (Figure 1.2a). These systems usually operate in a low-temperature range (between 20 °C to 100 °C [4]) with advantages of simpleness, small size, low cost and safety. They have been extensively used in individual households and large residential buildings in China. By using the solar thermal energy, the consumption of electricity and natural gas is reduced.
- Industrial waste heat recovery. Industrial activities emit a great amount of waste heat to the environment [6]. Recovering industrial waste heat can prevent this heat being emitted into the environment, which mitigates global warming. Moreover, it increases the energy supply. The mobile TES system addresses the geographical mismatch between the heat source and heat demand (Figure 1.2b).

- Solar power generation. Solar thermal energy stored during the day provides heat to generate power to meet the electricity demand in the evening [7]. Additionally, the TES system buffers solar fluctuation by storing unsteady solar energy and releasing steady heat, so the power generation system can operate under design conditions (Figure 1.2c).
- Space heating/cooling. Sustainable buildings with TES materials in walls and ceilings absorb heat during the day and release it during the night (Figure1.2 d-e), keeping a comfortable indoor environment with reduced energy consumption. Moreover, TES-based space heating/cooling technology does not generate noise, which improves the thermal comfort [8].

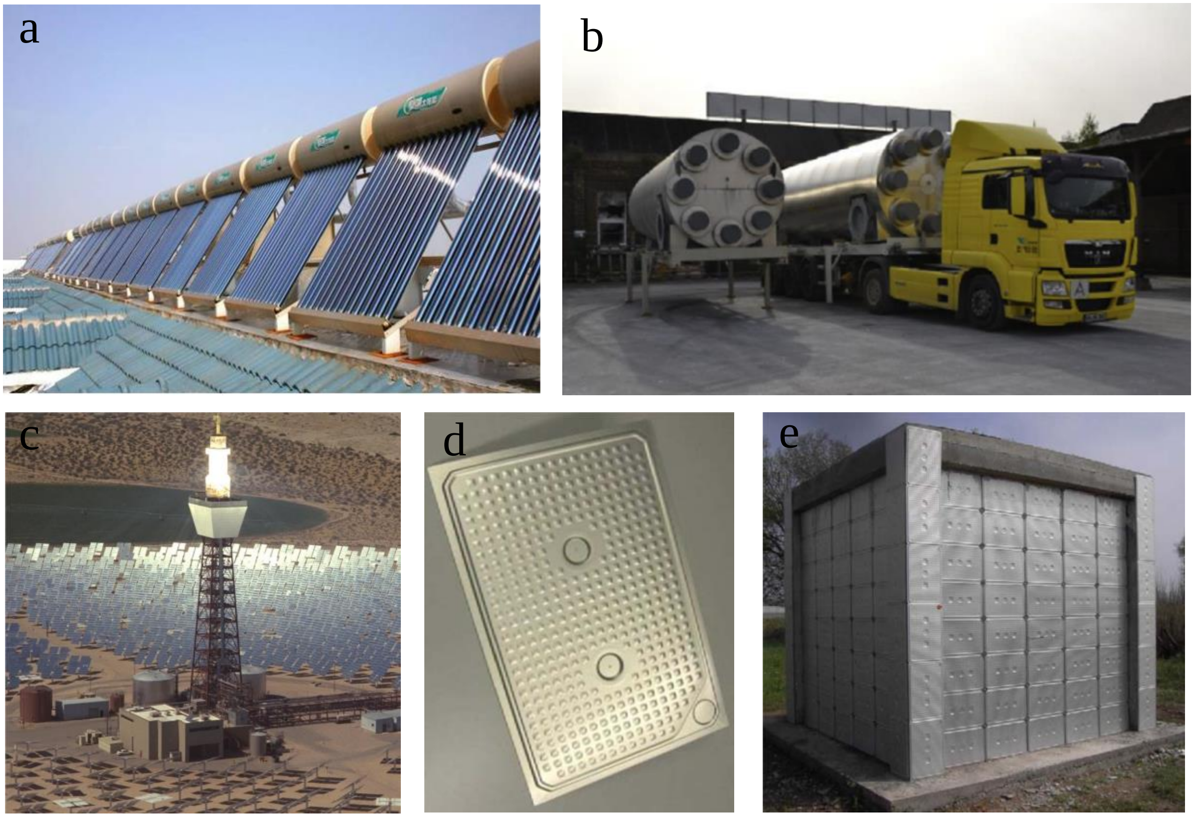

Figure 1.2: Various thermal energy storage applications. (a) Domestic hot water supply; (b) industrial waste heat recovery [6]; (c) solar power generation [9]; (d)-(e) sustainable building [10].

According to the heat storage mechanism, the TES technology is generally classified into sensible heat thermal energy storage (SHTES), latent heat thermal energy storage (LHTES) and thermochemical reaction thermal energy storage (TCTES) [11]. Table 1.1 summarizes the principle, advantages and typical materials of three TES technologies. TCTES remains in the preliminary research stage of the laboratory [12]. SHTES stores thermal energy by changing the temperature of materials. The amount of stored heat depends on the temperature change and the specific heat of sensible heat storage materials (SHM). The advantage of SHTES is that the raw materials are widely accessible and low-cost. LHTES stores heat through the phase change such as solid-liquid phase change, solid-solid phase change, solid-gas phase change and liquid-gas phase change [13]. For the solid-solid phase change, heat is stored when the material is transformed from one crystalline to another. The disadvantage is that the latent heat is low. For solid-gas and liquid-gas phase change, although the latent heat is high, the volume change is great, making the system complex and dangerous, which rules out their practical applications. For solid-liquid phase change, heat is stored when the solid material is melted; heat is released when the liquid material is solidified. Solid-liquid phase change materials (PCM) have relatively small volume change (10% or less) and large latent heat, so they are reliable and efficient heat storage media. (As this thesis focuses on solid-liquid phase change energy storage, "LHTES" and "PCM" in the following thesis refer to solid-liquid latent heat thermal energy storage and solid-liquid phase change material)

Compared to SHTES, the energy storage density of LHTES is higher. For example, the latent heat of $NaNO_3$ is 172 kJ/kg, and the specific heat is 1.1 kJ/(kg · °C) [14], meaning that the amount of energy stored by the phase change in LHTES is more than that by increasing the 150 °C temperature of materials in SHTES. Moreover, the temperature keeps almost constant during charging/discharging, which is very important to stabilize the temperature in some applications. These advantages not only reduce system requirements (size, temperature resistance, etc.) but also improve thermal storage performance. As a result, LHTES is more attractive than SHTES.

Table 1.1: Principle, advantages and typical materials of three TES technologies [13, 15, 16].

TES technology	Principle	Advantage	Typical material
Sensible heat storage	Temperature change	1) Widely accessible raw materials 2) Low cost	Water, stone, brick
Latent heat storage	Phase change	1) High energy storage density 2) Almost constant temperature during charging/discharging	Paraffin, salt
Thermochemical reaction storage	Chemical reaction	1) High energy storage density 2) Negligible heat loss	Zeolite

1.3 Phase change material

Phase change material (PCM) is the core of LHTES. During the phase change process, the temperature of PCM almost keeps unchanged while the energy is increased. A simple example is the melting of ice. During the melting (solid-to-liquid phase change), the temperature of ice remains at 0 °C but ice still absorbs heat and its energy is increased. It is normal that the energy of a material will be increases if its temperature rises. For PCM, the energy is increased without increasing the temperature; vice versa, the energy is reduced without decreasing the temperature. This characteristic is very important to some applications which require constant temperature. For example, in thermal management of chips, PCM with an suitable melting point absorbs heat generated by chips so that the temperature of chips would not increase; when the ambient is cold, PCM releases heat so that chips work in a warm environment [17]. Unlike conventional thermal management technologies such as heat pipes, PCM not only dissipates heat but releases heat, so chips can always work around a suitable temperature. In terms of TES applications, the characteristic of constant temperature also plays an important role. For example, PCM with ~26°C melting point (human comfort temperature) is embedded in building materials so that the indoor temperature can keep a thermal comfort level [8]. In addition, the energy capacity during the phase change is large. As mentioned in the last section, the latent heat of $NaNO_3$ is 172 kJ/kg and the specific heat is 1.1 kJ/(kg·°C) [18], meaning that the energy stored during the phase change is more than the energy by increasing 150 °C temperature.

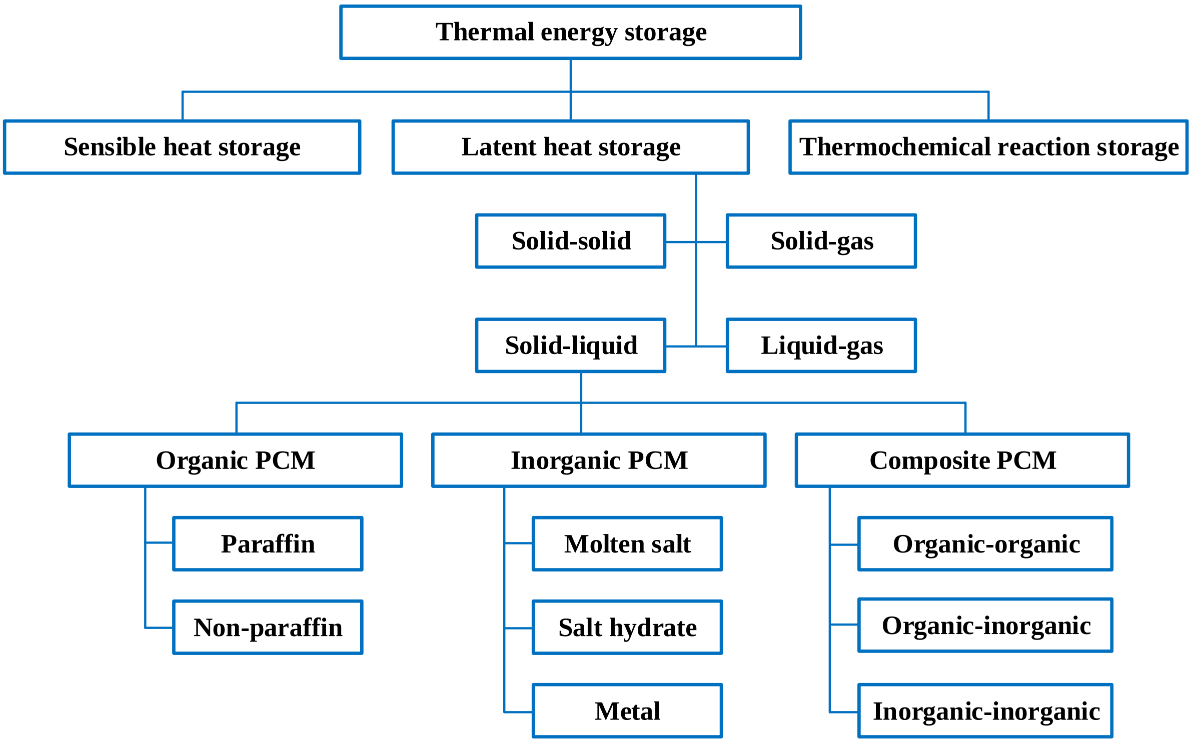

Figure 1.3: Classification of TES technologies and materials.

There are many types of PCMs and they can be classified based on different criteria. According to the melting point, PCMs are classified into low-temperature (melting point < 100°C), medium-temperature (melting point 100°C ~ 300°C) and high-temperature (melting point > 300°C) ones [19]. According to the chemical nature, they are classified into organic PCMs, inorganic PCMs, and eutectic PCMs [18]. Organic PCMs are further classified into paraffin and non-paraffin (fatty acid, polymer, etc). Inorganic PCMs include salts, salt hydrate, and metal (Figure 1.3). Their advantages are high latent heat per unit volume, non-flammable and low cost. Eutectic PCMs, including organic eutectics, inorganics eutectics, and organic-inorganic eutectics, are a mixture of two or more soluble ingredients [18, 20].

However, almost all pure PCMs except metals suffer from low thermal conductivity [22]. The thermal conductivity of organic PCMs is about 0.1 - 0.4 W/(m·K) while that of inorganic

PCMs is about 0.4 - 1 W/(m·K) [23], much lower than the thermal conductivity of SHM (sensible heat storage material), as indicated in Table 1.2. The poor thermal conductivity results in slow charging/discharging rate and low energy storage efficiency. Thus, the heat transfer enhancement is required.

Table 1.2: Comparison of thermal conductivity between sensible heat storage materials (SHM) and phase change materials (PCM) [23-26].

SHM	Thermal conductivity, W/m K	PCM	Thermal conductivity, W/m K
Basalt	3.2	Paraffin	0.167 (liquid)
Granite	1.73-3.98		0.346 (solid)
Gneiss	2.7-3.1	Fatty acid	0.149 (liquid)
Marble	2.07-2.94		0.153 (solid)
Quartzite	2	Solar salt	0.48 (liquid)
Sandstone	1.83		0.59 (solid)

1.4 Heat transfer enhancement of PCM

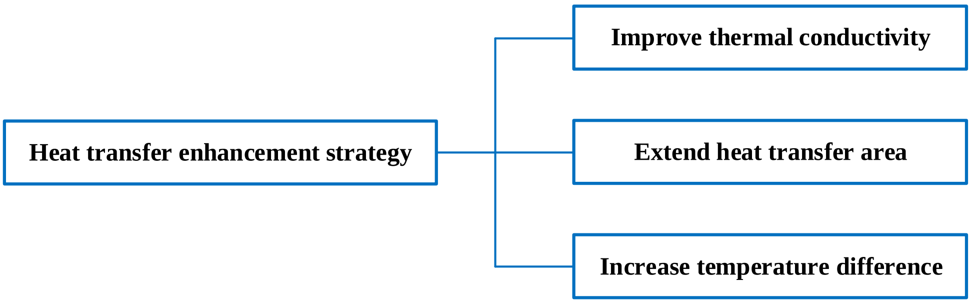

Figure 1.4: Three heat transfer enhancement strategies.

Generally, the heat transfer can be enhanced through three strategies (Figure 1.4): improving the thermal conductivity of PCM, extending the heat transfer area and increasing the temperature difference between PCM and HTF (Heat Transfer Fluid). Based on these strategies, several heat transfer enhancement methods have been proposed: fins, heat pipes, nanoparticles, multiple PCMs and porous CPCMs [22] (Figure 1.5).

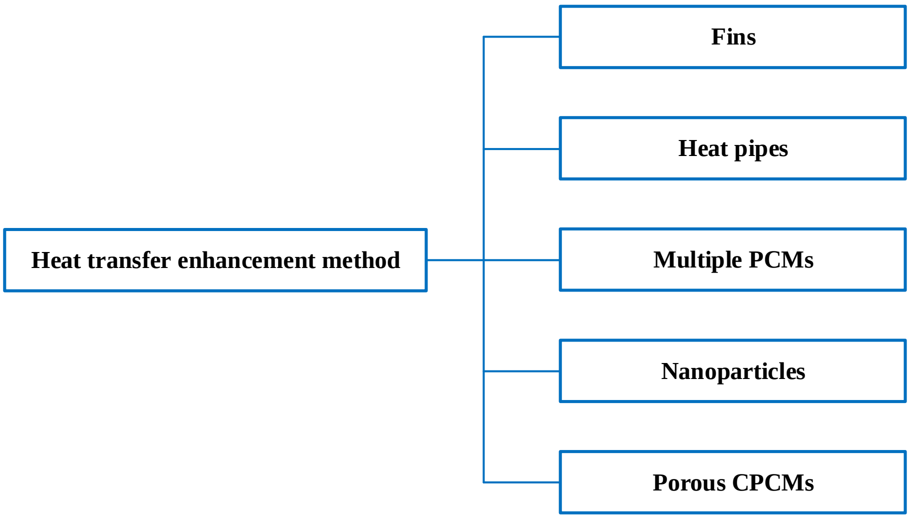

Figure 1.5: Several heat transfer enhancement methods.

- Fins. Fins are used to increase the heat transfer area between HTF and PCM. Some typical fins include longitudinal fins [27], annular fins [28], tree-shaped fins [29] and ladder-shaped fins [30].
- Heat pipes. Heat pipes act as the thermal carrier between HTF and PCM. One suitable TES configuration for the use of heat pipes is the shell-and-tube system where HTF flows through the inner tube and PCM occupies the annulus space [22].
- Multiple PCMs. In a shell-and-tube system, multiple PCMs are arranged in order of the melting point along the axial direction [31]. The principle is that the HTF temperature decreases along the flow direction; at the end of the system, the melting point of PCM is low so the difference between the HTF temperature and PCM melting point is still large.
- Nanoparticles. Highly conductive nanoparticles such as Al_2O_3 nanoparticles [32] are added to PCM to improve the thermal conductivity.
- Porous CPCMs. The porous skeleton increases the heat transfer area between PCM and HTF. Moreover, the thermal conductivity of the porous skeleton is much large, which improves the effective thermal conductivity of PCM.

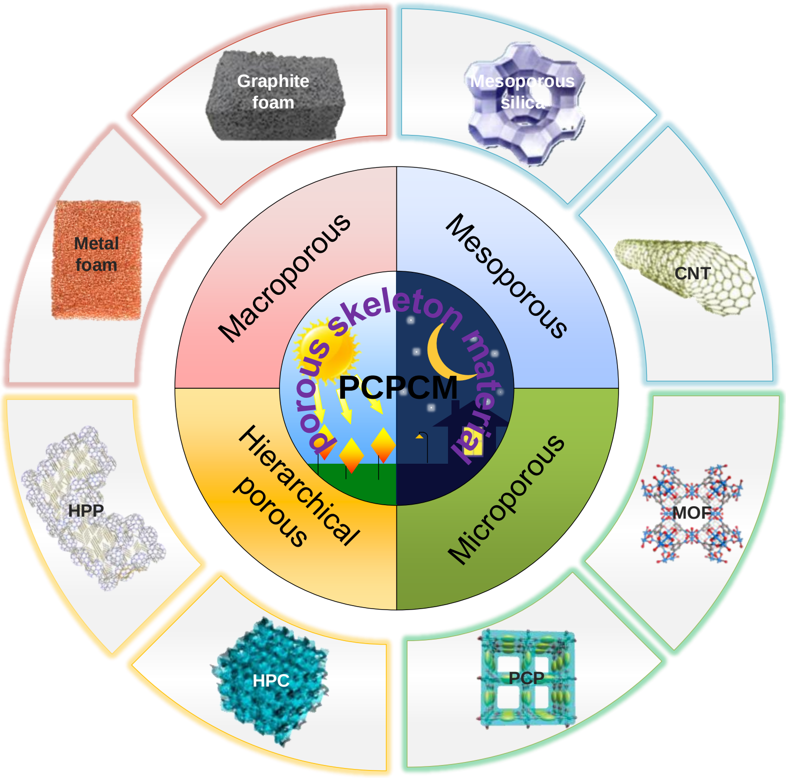

Figure 1.6: Skeleton materials of porous CPCMs.

*: CNT: carbon nanotube; MOF: metal-organic framework; PCP: porous coordination polymer; HPC: hierarchical porous carbon; HPP: hierarchical porous polymer

Fabricating porous CPCMs is a popular and attractive method to enhance the heat transfer of PCM. According to the pore size, porous skeletons are classified into macroporous (pore size > 50 nm), mesoporous (pore size: 2~50 nm), microporous (pore size < 2 nm) and hierarchical porous (pore size covers two or more length scales) ones [33]. The widely-used skeleton materials are shown in Figure 1.6.

1.5 Research aim and objectives

Thermal transport in porous CPCMs is very important to evaluate the performance and design LHTES systems [34]. The aim of the current research is to investigate the thermal transport in a novel ceramic foam/salt porous CPCM for medium-temperature thermal energy storage. The ceramic foam is employed to enhance the heat transfer of salts. This foam is open-cell, which enables natural convection of PCM and benefits thermal transport. And it is compatible with salts. The foam is fabricated alone and very easily integrated with/separated from salts so that if the foam or salt fails, only the single foam or salt needs to be maintained, rather than the whole CPCM, reducing the maintenance cost.

The main research objectives are:

- To review the literature on thermal transport in porous CPCMs.
- To fabricate the ceramic foam/salt CPCM using economically feasible technique and materials, removing the cost barriers in the way of applications.
- To test the compatibility between the prepared ceramic and salt through melting/solidification cycles and ensure the corrosion resistance of the ceramic.
- To evaluate the thermal transport performance of ceramic foam/salt CPCM both experimentally and numerically, considering multiple factors such as different containers, porosities, pore sizes, filling height, diameters and fluctuating heat source.

1.6 Methodology

Research methods used in the thesis include experiment, molecular dynamics (MD) simulation and computational fluid dynamics (CFD) simulation. The thesis structure is shown in Figure 1.7. The thermo-physical properties of salts ($NaNO_3$-KNO_3) with various component ratios are measured in Chapter 3, providing the fundamental thermal properties for later heat transfer study. Moreover, the MD simulation is performed to reveal the mechanism under the component-dependent properties. The preparation of ceramic foam/salt CPCM is introduced in Chapter 4. The wettability of the ceramic to salts is measured to determine the impregnation method. Then, in Chapter 5, the compatibility between the prepared ceramic and salt is tested through melting/solidification cycles. The corrosion experiment of Cu and Al (the common enhancement materials for low-temperature PCMs) is also conducted to make a comparison. Advanced characterization technologies are employed to analyse the corrosion behaviours.

And a reactive MD simulation is performed to provide microscopic insights into corrosion behaviours.

The above studies confirm the technical feasibility and corrosion resistance of ceramic foam, laying the foundation for the later heat transfer study. The thermal transport performance of CPCM is investigated in Chapters 6 – 8. The heat transfer characteristics in the cavity are studied through experiments and CFD simulation in Chapter 6. The energy and exergy analysis is carried out to comprehensively evaluate the ceramic foam/salt CPCM. The melting performance in a shell-and-tube unit is numerically studied in Chapter 7. Multiple factors including porosity, foam filling height, and outer diameter are considered and compared to provide an optimal configuration. In Chapter 8, the thermal performance of pure PCM and CPCM under solar fluctuation in Nottingham, the UK is numerically studied to better understand the practical energy storage process.

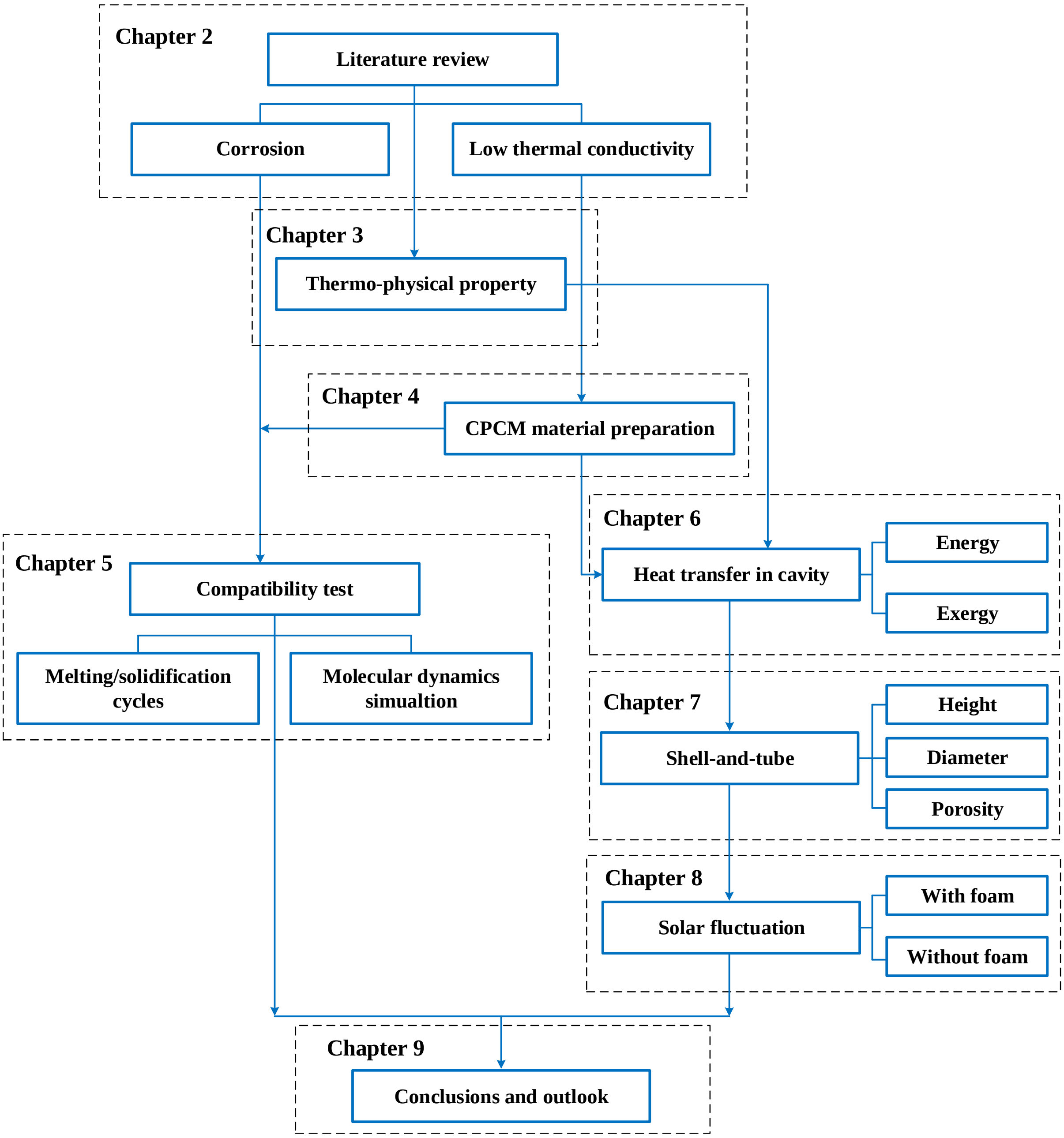

Figure 1.7: The thesis structure.

Chapter 2 - Literature review

Phase change heat transfer is very important to evaluate the performance of porous CPCMs and design LHTES systems. It has been extensively studied and significant advancements have been achieved. The critical experimental and numerical studies are reviewed in Section 2.1 and Section 2.2 respectively.

2.1 Experimental study on phase change heat transfer in porous CPCM

The experiment is the most direct method to study phase change heat transfer in porous CPCM. In Section 2.1.1, materials, i.e. PCMs and porous skeletons will be introduced. Then, some key findings from experimental studies will be presented in Section 2.1.2.

2.1.1 Materials

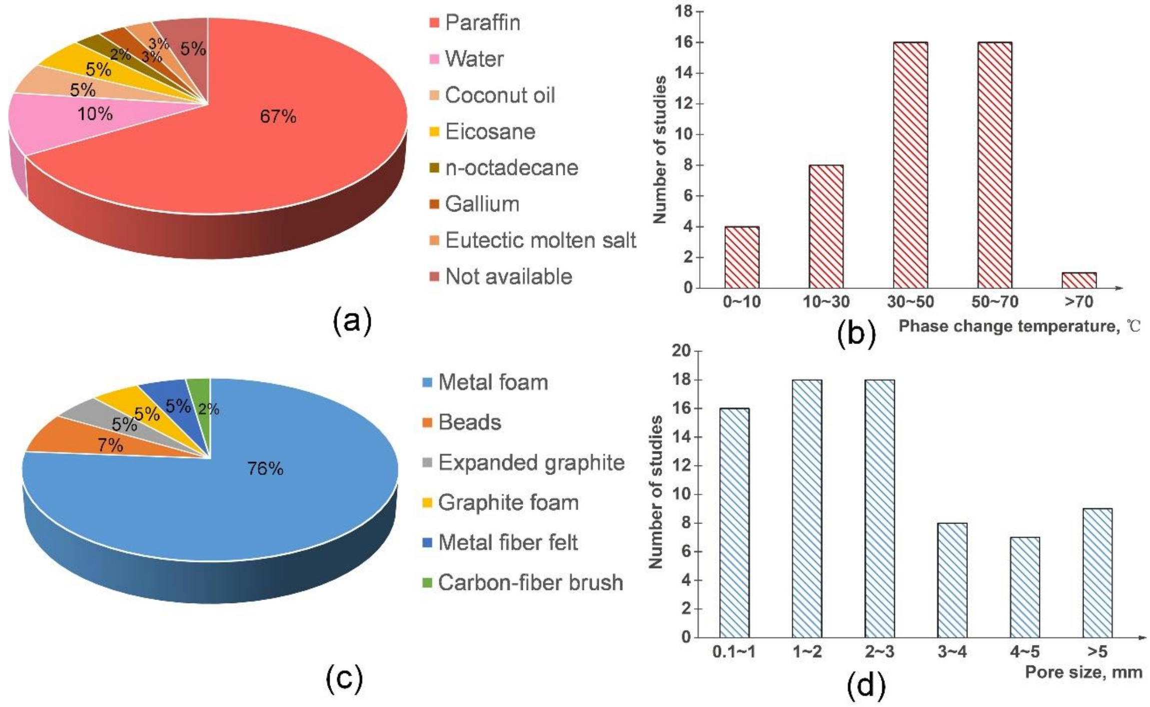

Figure 2.1: Statistic of porous CPCMs employed in studies on phase change heat transfer: (a) types of PCMs; (b) number of studies under different phase change temperature; (c) types of porous skeletons; (d) number of studies under different pore sizes.

To the author’s best knowledge, the first experimental study on the phase change heat transfer of porous CPCM was conducted by Weaver and Viskanta in 1986 [35]. In their research, water and glass beads were employed as PCM and porous skeleton, respectively. Since then, it has been over 35 years for studies in this field, and materials have changed a lot. Table 2.1 lists CPCMs and their properties in experimental studies from 1986 to 2019. And Figure 2.1 gives statistic of materials and properties. It can be seen that most researchers focus on low-temperature PCMs (the phase change temperature lower than 100 °C). The only study on medium-temperature PCM was carried out by Zhang et al. where the phase change temperature of PCM was 218 – 228 °C [36]. In addition, the pore size of porous skeletons is over 0.1 mm. In other words, all of them are macroporous.

The metal foam is the most used porous skeleton in the experimental studies. There are mainly two methods to fabricate metal foam-based CPCMs. The first one is the directly pouring method, which is adopted by Righetti et al. [37], Mallow et al. [38], etc. The procedure of this method is that the hot liquid PCM is directly poured into a container and mixed with the porous skeleton. This approach is simple and does not need extra device. However, due to the air existing in the porous skeleton, liquid PCM cannot infiltrate the skeleton completely. Thus more researchers employed the vacuum impregnation (or vacuum infiltration) method, such as Zhang et al. [34], Jin et al. [39], etc.

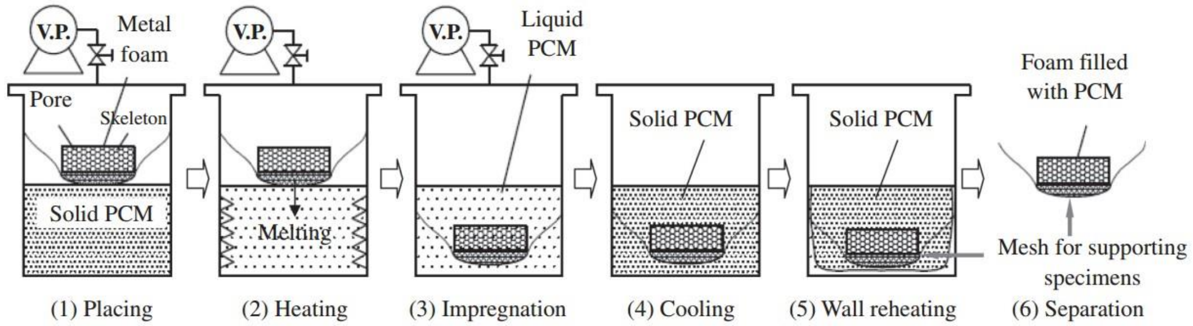

Figure 2.2: Flow chart of vacuum impregnation method to fabricate metal foam-based CPCM [40].

A typical flow chart of the vacuum impregnation method is presented in Figure 2.2. The procedure consists of six steps: firstly, the solid PCM, metal foam and a mesh which is used to support the foam are placed into a container. A vacuum pump is connected to the container and switched on to evacuate the air. Secondly, the container is heated and the metal foam sinks into the melted PCM. After the porous skeleton is fully impregnated by liquid PCM, the heating process is stopped and the vacuum pump is switched off at the same time. Then the container is cooled. When the PCM is completely solidified, the container is reheated slightly to make it easy to withdraw the sample. Finally, the CPCM is taken out and the surplus PCM on the surface is removed.

Table 2.1: Summary of porous CPCMs and properties in experimental studies on phase change heat transfer.

Ref.	PCM/porous skeleton	Porosity, -	Pore size, mm	Phase change point, °C	Latent heat, kJ/kg
[35]	Water/glass beads	0.36-0.38	-	0	-
[41]	Water/aluminum beads	0.39	-	0	-
[42]	Gallium/glass beads	0.385	-	29.78	-
[43]	Paraffin/copper foam	0.90-0.95	0.85-2.54	58	181
[44]	Paraffin/aluminum foam	0.9137	2.82	55-60	120
[45]	PureTemp® 25/aluminum foam	0.921-0.933	1.27-5.08	24.1-26.3	187
	PureTemp® 25/copper foam	0.947	1.27		
	PureTemp® 25/graphite foam	0.811	0.42		
[46]	Water/aluminium foam	0.946	0.64	0	315-333
[47]	Paraffin/aluminium foam	0.77-0.95	-	50-60	117
[48]	Paraffin/aluminium foam	0.859-0.958	-	52-57	200
[49]	Paraffin/copper foam	0.95	5.08	48.4-63.6	148.8
[50]	Paraffin/carbon-fibre brushes	0.992-0.9932	-	40-53	180
[51]	PCM/ aluminium foam	-	2.54	15	182

[52]	Water/copper foam	0.93-0.97	0.85-3.18	0	-
[53]	Paraffin/copper fibre sintered felt	0.75-0.95	0.15	48.6	217.9
[54]	Paraffin/copper foam	0.968	1.27	48-50	250
[55]	Coconut oil/ aluminium foam	0.88-0.96	5.08	24	103
[56]	Paraffin/copper foam	0.96	1.27	-	-
[57]	Paraffin /stainless-steel fibre felt	0.8-0.9	0.1-0.2	47.38	170.7
[58]	Paraffin/ aluminium foam	0.92-0.93	0.635-5.08	42-64	165-250
[59]	Coconut oil/ aluminium foam	0.88-0.96	1.27-5.08	24	103
[60]	Eicosane/copper foam	0.95	0.127-2.54	36.5	-
[61]	Paraffin/copper foam	0.90-0.98	0.64-2.54	46.48-60.39	102.1
[34]	Paraffin/copper foam	0.97	1.02	54.43-64.11	175.24
[62]	Paraffin/copper foam	0.92	1.27	48-50	136.4
[63]	Paraffin/copper foam	0.815, -	0.847	25-28,	184
	$CaCl_2\cdot 6H_20$/copper foam	0.815	0.847	29	190.8
	Paraffin/expanded graphite	-	-	25-28	184
[38]	Paraffin/aluminium foam	0.905-0.912	0.635-2.54	55.2	132.2
	PT37/aluminium foam	0.905-0.912	0.635-2.54	37	210
	Paraffin/graphite foam	-	-	55.2	132.2
[36]	$NaNO_3$ and KNO_3/copper	0.965	2.54	218-228	122.89
	$NaNO_3$ and KNO_3/nickel foam	0.975	2.54	218-228	122.89
[64]	Paraffin/copper foam	0.97	2.54	68	213
[65]	Paraffin/copper foam	0.98	1.69	52-54	-
[39]	Paraffin/copper foam	0.949-0.961	0.51-1.69	46.4	-
[66]	Paraffin/copper foam	0.95	0.635-5.08	52-60	-
[67]	Paraffin/ aluminium foam	0.7-0.9	-	46-52	-
[68]	Paraffin/expanded graphite	-	-	61.33-61.62	170.7-180.6

[69]	Paraffin/copper foam	0.974	2.54	26	179
[37]	Paraffin/ aluminium foam	0.893-0.948	0.635-5.08	40	165
[70]	n-octadecane/aluminium foam	0.87-0.96	0.635-5.08	28	243.5
[71]	Paraffin/copper foam	0.95-0.97	0.73-1.69	47-57	167
[72]	N-eicosane/copper foam	0.86	2.54	36.5	-
[73]	Paraffin /copper foam	0.91	2.54-5.08	35	230

2.1.2 Solid-liquid phase-change process

2.1.2.1 Phase interphase evolution

(a) 0s MF=0.00% (b) 1440s MF=2.27% (c) 3420s MF=34.68% (d) 4140s MF=48.89%

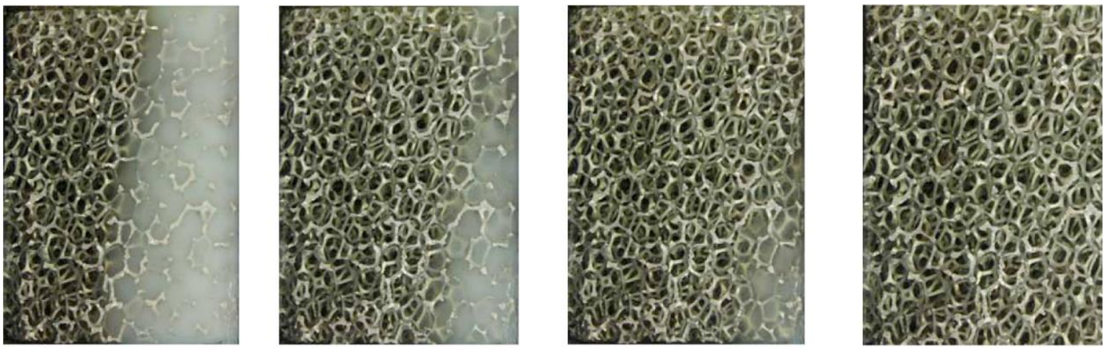

(e) 4320s MF=55.54% (f) 4860s MF=83.71% (g) 5040s MF=94.93% (h) 5400s MF=100%

Figure 2.3: Evolution of solid/liquid phase interface under the condition of left heated wall (MF: melting fraction) [55].

In 2012, Li et al. [61] experimentally studied the melting process of paraffin enhanced by copper foam in a 100 mm (length) × 45 mm (width) × 100 mm (height) rectangular cavity. The CPCM was heated on the left side. The solid/liquid interface at 3600 s and 3780 s presented a sloped shape. Zhang et al. [34] conducted an experiment to study the melting phase change in paraffin/copper foam CPCM. They found that at the initial stage, the melting front was almost parallel to the heating boundary, indicating that the heat conduction dominated the phase change heat transfer. With time elapsed, more PCM was melted and the hot liquid PCM flowed upwards under the buoyancy force, leading to a faster melting rate in the upper half. As a result, the melting front became slope-shaped. A similar phenomenon can be found in Al-Jethelah et al. [55]'s research and the results are shown in Figure 2.3. Al-Jethelah et al. classified the melting process into three stages according to the heat transfer mechanism:

(1) Conduction-dominated stage: the solid/liquid interface was parallel to the heating wall and the thermal energy was transferred to solid PCM in the form of sensible heat (Figure 2.3(b)).

(2) Conduction-convection-mixed stage: liquid PCM flowed upwards under the buoyancy force and a wide circulatory region was formed in the upper half, curving the interface; in the lower part, the interface was still vertical due to the conduction (Figure 2.3 (c), (d)).

(3) Convection-dominated stage: With time elapsed, more PCM was melted and was pushed by buoyancy force to flow upwards along the heating wall and downwards along the solid/liquid interface. A more sloped interface was formed (Figure 2.3 (e)-(g)).

Diani et al. [58] used paraffin as PCM and aluminum foam as porous skeleton to study the phase change heat transfer in a 20 mm (length) × 100 mm (width) × 100 mm (height) cavity. Venkateshwar et al. [59] investigated the melting process of aluminum foam/coconut oil with nanoparticles. The solid/liquid interface evolution obtained by these researchers is similar to that by Al-Jethelah et al. [55].

It should be noted that the above studies are under the condition of the left heating wall. Different heating position may lead to different solid/liquid interface. Zheng et al. [49] conducted an experiment where the paraffin/copper foam CPCM was heated by the left, bottom, and top wall, respectively. The interface propagation in the case of left heating wall was similar to Al-Jethelah et al. [55]'s results, while the other two cases were different. For the condition of the bottom heating wall, the melting front at the early stage was parallel to the heating boundary. However, at 4.5 h, the PCM in the middle was melted faster than on sides and two symmetrical annular flows were formed. For the case of top heating, the phase interface was always parallel to the heating wall because the influence of natural convection was insignificant.

The cylindrical container is another widely used enclosure for porous CPCMs. In 2008, Siahpush et al. [60] investigated the melting/solidification process of copper foam-based CPCM in a 155.5 mm (inner diameter) × 304.8mm (height) tube. During the experiment, the temperature of the outer wall of the container was kept constant. It was found that the curvature of solid/liquid interface in the case with metal foam was not as remarkable as the case without metal foam.

Yang et al. [62] studied the phase change process in a shell-and-tube unit. Copper foam and a fin were inserted into the paraffin to enhance heat transfer. For the PCM with copper foam, the interface was cone-shaped and developed from the inside to outside, while for the case with copper foam and fin, the melting interface was inversed funnel-shaped. Recently, Yang et al. [54] performed a visual experiment to investigate the melting process of PCM/metal foam in a shell-and-tube unit. It was found that at the initial stage (60 min), the inner interface was vertical, indicating that the conduction dominated the heat transfer. With the elapse of time, more PCM was melted and the natural convection remarkably contributed to the heat transfer. The hot liquid PCM was pushed upwards by buoyancy force and accelerated the phase change in the upper region, so forming a funnel-shaped interface. For the outer solid/liquid interface, it was horizontal during the whole phase change process.

2.1.2.2 Temperature distribution and variation

Thermocouples are widely used to record temperature distribution and variation during the phase change process. For instance, Zhou et al. [63] arranged four thermocouples at different positions in a rectangular cavity. They found that during the melting process, the temperature of PCM with metal foam was higher than that without metal foam, implying that the heat was transferred faster by metal foam. Wang et al. [67] studied the paraffin/aluminum foam CPCM in a battery. Their results showed that the existence of aluminum foam improved the temperature uniformity of PCM. Zhang et al. [36] experimentally investigated the phase change process of salt/metal foam CPCM. Thermocouples were fixed along the axis and wall of a cylindrical container (see Figure. 2.4(a)). During the experiment, the container was heated in the oil bath. The variation of temperature is shown in Figure 2.4(b). For the pure PCM, the temperature at point D was higher than that at point B and C, while for salt/metal foam CPCM, the temperature at point B was highest.

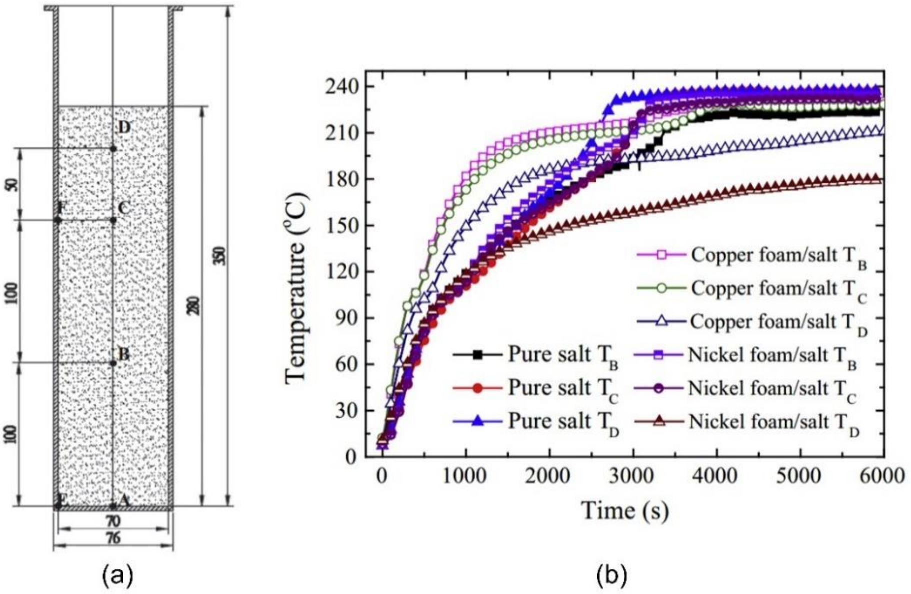

Figure 2.4: (a) Schematic of thermocouple distribution; (b) the variation of temperature with time [36].

Recently, the infrared camera was used by some researchers to capture the temperature field. In Zhang et al. [34]'s experiment, the cavity was heated by the left wall. It can be seen from Figure 2.5 that at the initial stage, the temperature contours were almost vertical. With the elapse of time, more PCM was melted and the natural convection became significant, which accelerated the interface propagation in the top region. Yao et al. [69] investigated the melting process of paraffin/copper foam using an infrared camera. Their results showed that the copper foam improved the temperature uniformity and increased the melting rate by 2 times.

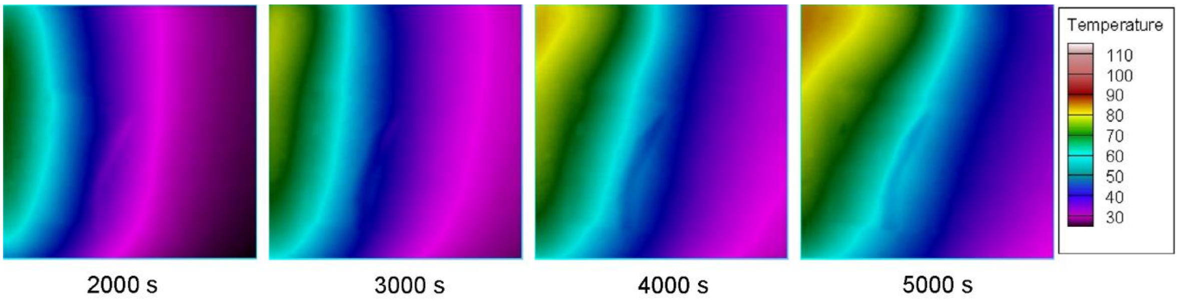

Figure 2.5: Variation of temperature field captured by an infrared camera [34].

2.2 Numerical investigation on phase change heat transfer in porous CPCM

The numerical simulation is time- and cost-saving and can provide detailed flow and heat transfer information. Generally, the numerical methods for phase change heat transfer in porous CPCMs can be classified into representative elementary volume (REV)-scale method and pore-scale method [74]. The schematic of the two methods is presented in Figure 2.6 and the comparison is listed in Table 2.2. The REV-scale simulation treats the porous CPCM as a uniformly mixed medium (see the typical computational domain in Figure 2.7(a)) and does not require an accurate description of the skeleton structure. In other words, it ignores the complex geometry of the skeleton. Instead, this method uses some statistical parameters, such as porosity, permeability, and effective thermal conductivity, to characterize the porous skeleton. Therefore, it suits the simulation of large-size systems. To account for the presence of the porous skeleton, terms based on semi-empirical models are added into the governing equations. Through choosing appropriate semi-empirical models, the REV-scale simulation can provide reasonable results. The REV-scale method includes the traditional CFD methods, such as finite-difference method (FDM), finite-volume method (FVM) and finite-element method (FEM), and the REV-scale lattice Boltzmann method (LBM).

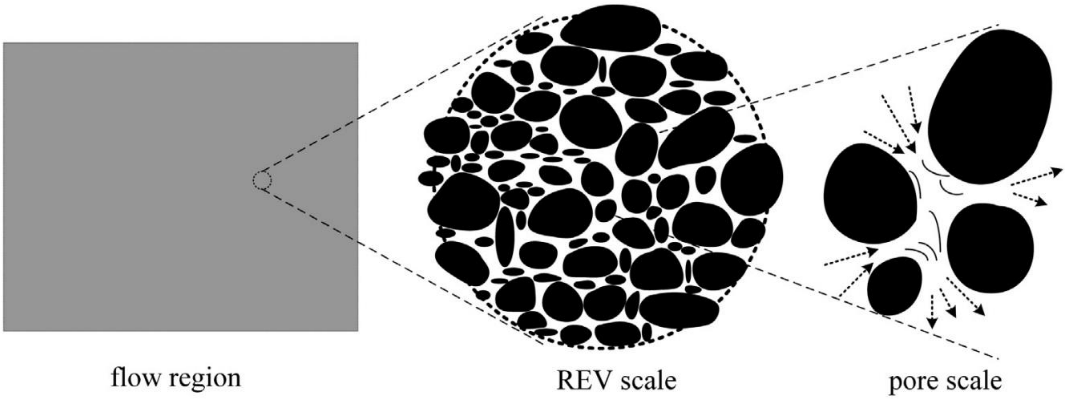

Figure 2.6: Schematic of REV-scale and pore-scale method [75].

Table 2.2: Comparison between REV-scale and pore-scale simulation.

Method	REV-scale simulation	Pore-scale simulation
Feature	Treat the porous CPCM as a uniform mixture by volume average and simulate the phase change of the mixture	Directly simulate the phase change of PCM in porous skeleton
Advantages	(1) Simple input (2) Less computational sources (3) Large simulated system	(1) Exhibiting flow and heat transfer in pores (2) Reflecting the effect of pore structure on phase change
Disadvantages	(1) Lack of flow and heat transfer characteristics in pores (2) Disability in revealing the effect of the pore structure	(1) High computational cost (2) Complex geometry input
Simulation approach	FVM FEM FDM LBM	LBM DNS

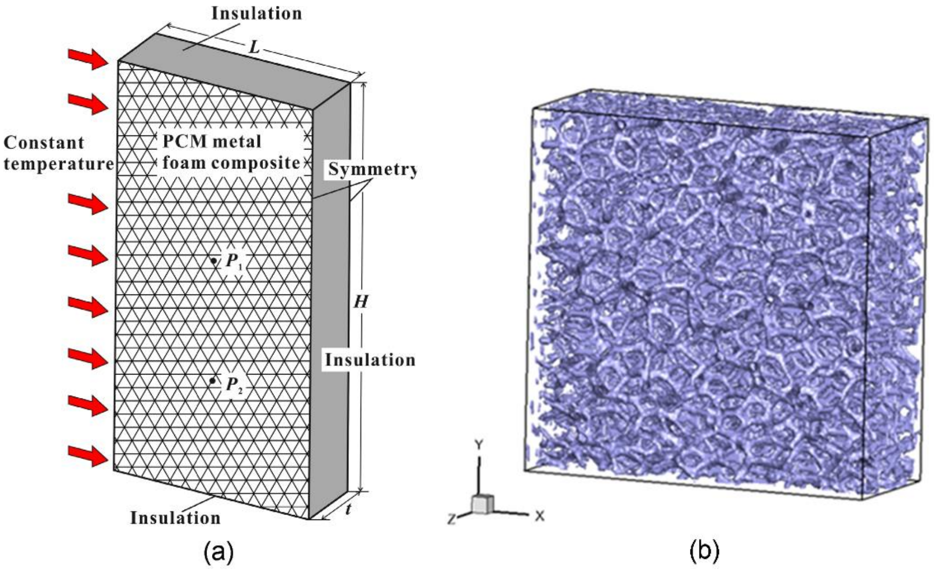

Figure 2.7: Typical computational domain in (a) REV-scale simulation and (b) pore-scale simulation [11].

The pore-scale method adopts the real porous structure as the computational domain, as Figure 2.7(b) shows. It directly models the flow of PCM in pores. Therefore, it can reflect the influence of pore structure on the phase-change process and provide more information than the REV-scale simulation. As Lattice Boltzmann Method (LBM) has the robust ability to handle complex boundaries, it has been widely used to perform the pore-scale simulation [76]. In this section, the REV-scale simulation by traditional CFD methods will be introduced in Section 2.2.1 and the pore-scale simulation based on the LB method in Section 2.2.2.

2.2.1 REV-scale simulation

2.2.1.1 Models and materials

According to the local thermal/non-thermal equilibrium, models used in the REV-scale method are classified into one-temperature model and two-temperature model [19]. The one-temperature model assumes there is a thermal equilibrium between the PCM and porous skeleton. This model was first applied to investigate the melting of ice in the porous medium by Weaver et al. [41]. In contrast, the two-temperature model takes into account the temperature difference between the PCM and porous skeleton. When the difference in thermal conductivity between PCM and porous skeleton is large, the two-temperature model is more accurate. A summary of REV-scale simulations is given in Table 2.3.

Table 2.3: Summary of REV-scale simulation.

Ref	Material	Porosity	Dimensional	Container
[50]	Paraffin/carbon-fiber brush	0.992-0.9932	3D	R
[77]	PCM/metal foam	0.385-0.8	2D	R
[43]	Paraffin/copper foam	0.95	2D	R
[78]	Paraffin/aluminum foam	0.90	2D	R
[79]	Paraffin/copper foam	0.85-0.95	2D	R
[61]	Paraffin/copper foam	0.90-0.98	2D	R
[80]	Paraffin/copper foam	0.90	2D	R
[81]	n-eicosane/aluminum foam	0.86-0.94	2D	R
[82]	NaNO3/copper foam	0.855-0.945	2D	R
[83]	Docosane/aluminum foam	0.757-0.9898	3D	R
[84]	Paraffin/aluminum foam	0.90	2D	R
[34]	Paraffin/copper foam	0.97	3D	R
[85]	Sodium acetate/aluminum foam	0.865-0.965	2D	R
[48]	Paraffin/aluminum foam	0.859-0.958	3D	R
[86]	Paraffin/aluminum foam	0.90	2D/3D	R
[87]	Succinonitrile/copper foam	0.8-0.95	2D	R
[88]	Paraffin/copper foam	0.9-0.97	2D	R
[60]	eicosane/copper foam	0.95	2D	C
[89]	Paraffin /graphite foam	0.85-0.97	2D	C
[90]	Li_2CO_3 and K_2CO_3/copper foam Li_2CO_3 and K_2CO_3/SiC foam Li_2CO_3 and K_2CO_3/Al_2O_3 foam Li_2CO_3 and K_2CO_3/ nickel foam	0.95 0.95 0.95 0.95	2D	C
[91]	Paraffin/copper foam	0.95	2D/3D	C
[92]	Li_2CO_3 and Na_2CO_3/metal foam	0.85-0.95	3D	C

[36]	$NaNO_3$ and KNO_3/ metal foam	0.965-0.975	3D	C
[93]	Paraffin/ metal foam	0.94	2D	C
[52]	PCM/copper foam	0.93-0.97	2D	R
[94]	Paraffin/copper foam	0.85-0.95	3D	R
[95]	RT82/copper foam	0.95-0.98	2D	C
[51]	PCM/aluminum foam	0.935-0.955	2D	C

*: “C” and “R” refer to cylindrical and rectangular, respectively.

Table 2.3 covers literature from 2000 to 2019. Figure 2.8 gives the statistics of types of porous skeleton and pore size. It is found that most skeletons are metal foam, and the pore size is over 0.1 mm (macroporous).

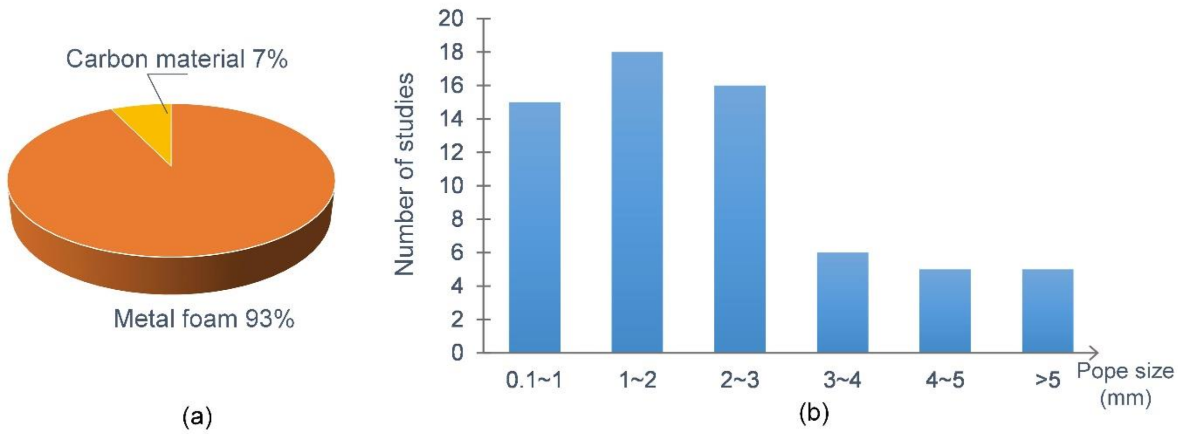

(a) (b)

Figure 2.8: Statistics of types of (a) porous skeleton and (b) pore size in REV-scale simulation.

According to the difference in geometry, PCM containers are classified into rectangular and cylindrical ones. The following two subsections will introduce REV-scale simulations in rectangular and cylindrical containers.

2.2.1.2 Rectangular container

In 2005, Krishnan et al. [77] investigated the melting process of PCM in a square container. They found that the metal foam accelerated the heat response of PCM because of the high thermal conductivity; on the other hand, it supressed the natural convection. Overall, it improved the thermal response. Later, Tian et al. [79] studied the phase change heat transfer of paraffin/copper foam in a 200 mm × 25 mm rectangular container. Their results showed that metal foam significantly enhanced the heat conduction, and although it suppressed the convection, the metal foam improved the overall heat transfer performance of PCM. Srivatsa et al. [81] numerically investigated the phase change of CPCM enhanced by aluminium foam in a 80 mm (length) × 62 mm (width) × 25 mm (height) container. It was found that the natural convection was strongest when PCM was melted completely.

In 2017, Zhang et al. [34] demonstrated several stages where different heat transfer mechanisms dominated. At the initial stage (1000 s), the melting interface was almost parallel to the left heating boundary, indicating that the conduction dominated the heat transfer. With time elapsed, more PCM was melted and high-temperature liquid PCM flowed upwards, accelerating the melting. As a result, a slope-shaped interface was formed. At this stage, the natural convection dominates the phase change heat transfer. In order to compare the temperature difference between PCM and porous skeleton, Zhang et al. [34] simulated the temperature field. The temperature of metal foam was generally higher than that of the PCM, especially in the solid region of PCM. When the PCM was melted completely, natural convection promoted the heat exchange between PCM and the porous skeleton, so the temperature difference became small. Li et al. [61] performed a numerical simulation on the melting process of porous CPCM in a 45 mm × 100 mm domain and they found that the temperature of porous skeleton was higher than that of PCM.

To compare the effect of heat conduction and natural convection, Yang et al. [86] conducted a simulation in a 76.2 mm (length) × 152.4 mm (height) × 25.4 mm (width) domain. Their results are presented in Figure 2.9. Without considering the natural convection, the melting front is always parallel to the heating wall. In contrast, taking into account the natural convection, a slope-shaped interface is formed. Yang et al. also compared contributions of the two heat transfer mechanisms and found that although the influence of natural convection was not negligible, heat conduction played a more important role. From this point of view, it also explains why the porous skeletonenhances the global heat transfer although it suppresses the natural convection.

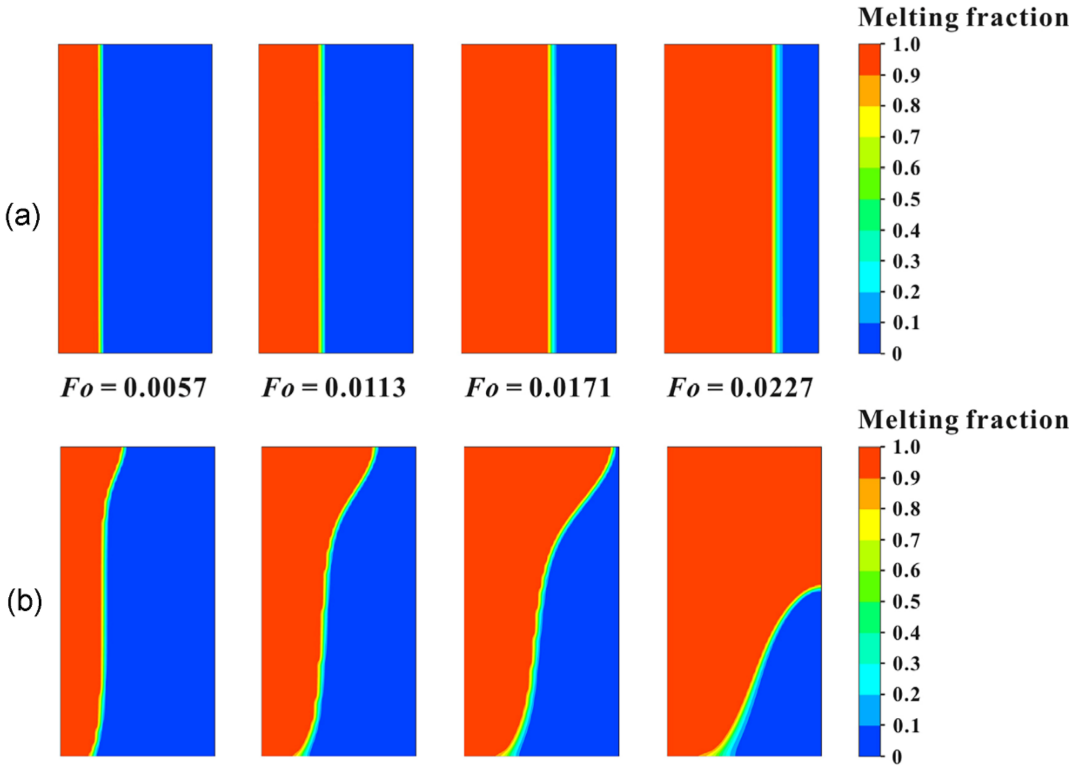

Figure 2.9: Solid/liquid interface propagation: (a) without considering natural convection (b) considering natural convection [86].

2.2.1.3 Cylindrical container

In 2008, Lafdi et al. [89] studied the phase change process of PCM/graphite foam in a cylindrical container. They found that the thermal performance of the system was improved significantly owing to the addition of high thermal-conductivity graphite foam. The average output power of the system was increased by more than 8 times. Liu et al. [91] performed a 3D simulation in a 40 mm (inner diameter) × 82 mm (inner diameter) × 250 mm (length) computational domain. In their study, the solid/liquid interface propagation and temperature distribution were predicted. The result shows that the temperature along the central tube decreased because the heat was absorbed by the surrounding PCM. A 335 K iso-surface moved from the inlet to the outlet during the melting process. Later, Zhang et al. [36] studied the melting/solidification of CPCM in a vertical cylindrical storage unit. They used $NaNO_3$ and

KNO_3 as PCM and found that the solid/liquid interface curved gradually during the melting process, indicating the increasing natural convection; for the solidification process, the phase interface was almost parallel to the cooling wall, implying that the heat conduction was dominant.

Some researchers optimized the configuration to improve thermal performance. For instance, Nithyanandam et al. [92] conducted a numerical study on the metal foam and heat pipe-enhanced TES unit. They simulated the melting/solidification process of four different configurations: (1) no heat pipe; (2) no heat pipe-metal foam; (3) 2 horizontal heat pipes-metal foam; (4) 2 vertical heat pipes-metal foam. Among, the 2 vertical heat pipes with metal foam was recommended to improve melting/solidification efficiency. Later, Xu et al. [90] evaluated and optimized the melting performance of a cylindrical TES unit partially filled with a porous skeleton. Their research showed that, to make the most of natural convection and save cost, the porous skeleton should be placed in the lower part of the tube and the optimal filling height ratio was 0.7.

2.2.2 Pore-scale LB simulation

Lattice Boltzmann method is a relatively new approach which is particle-based and employs a simple kinetic model [96]. The principle of this method is that, fluid is discretized into small particles and macroscopic heat and mass transfer are predicted by evolving thermal motion of fluid particles. LB method has three advantages: (1) simple calculation procedure; (2) parallel computation; (3) robust ability to handle complex geometries [96, 97]. LBM was first proposed by McNamara et al. [98]. Recently, many researchers have employed it to investigate phase change phenomena in porous skeleton [99]. LBM can perform the REV-scale simulation [100], however, its advantage of handling complex boundaries can be made the most by conducting the pore-scale simulation. This section will introduce the recent advancement of the pore-scale LBM simulation on the phase change heat transfer in porous CPCMs. A summary of related research is provided in Table 2.4.

Table 2.4: Summary of pore-scale LB simulation on phase change heat transfer in porous CPCMs.

Ref.	Porosity	Pore size, mm	Porous skeleton	PCM
[101]	0.9-0.94	-	Metal foam	Water
[102]	0.88	-	Metal foam	Gallium
[103]	0.9	-	Metal foam	Paraffin
[104]	0.95	0.75	Metal foam	Li_2CO_3-K_2CO_3
[44]	0.9137	2.82	Metal foam	Paraffin
[105]	0.9-0.98	0.5-1.25	Metal foam	Li_2CO_3-K_2CO_3
[106]	0.6-0.9	-	Metal foam	Paraffin
[107]	0.40-0.55	-	Soil	Water

2.2.2.1 Temperature field and phase interface

In 2018, Li et al. [101] studied the solid-liquid phase-change process in the metal foam. The structure-performance relation of PCM was analyzed under different gravity conditions. In their study, the computational domain was heated by the left wall. To compare the results between the pore- and REV-scale simulation, the author selected Zhang et al. [34]'s study where the physical model was also heated by the left wall. As Figure 2.10 shows, the overall distribution of the temperature field predicted by pore- and REV-scale method is similar: at the initial stage, the temperature contours were approximately parallel to the heating wall. With the elapse of time, more PCM was melted and the effect of the natural convection was significant, leading to slope-shaped contours.

Compared to the REV-scale simulation, the pore-scale simulation can reflect the influence of the pore structure. As seen from Figure 2.10, the temperature contours predicted by the pore-scale method were not as smooth as those by the REV-scale method. In the pore-scale simulation, some parts of the contours were parallel to the skeleton (see the marked area in Figure 2.10(a)). However, this phenomenon cannot be revealed by the REV-scale method.

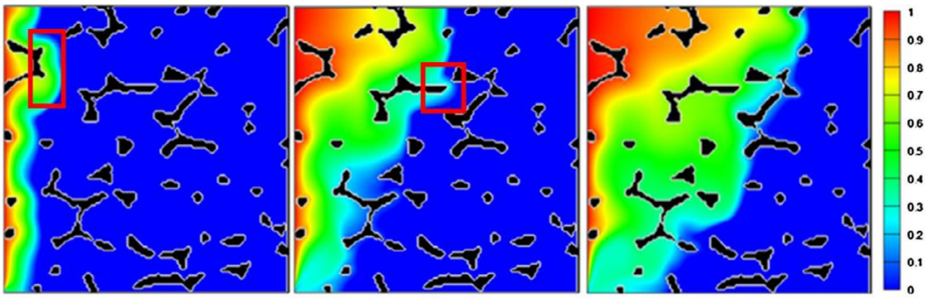

$Fo = 0.01$ $Fo = 0.04$ $Fo = 0.06$

(a) Pore-scale simulation

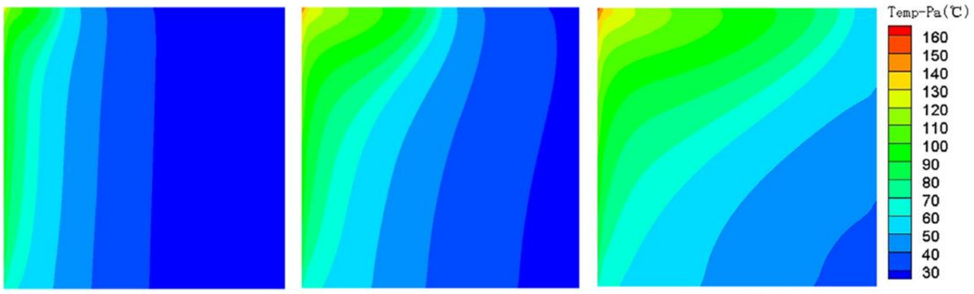

1000s 2000s 4000s

(b) REV-scale simulation

Figure 2.10: Comparison of temperature fields predicted by different methods [34, 101].

2.2.2.2 Flow field

Ren et al. [105] simulated the flow field of the phase change process, as shown in Figure 2.11(a). It can be seen that liquid PCM passed through the gap between the ligaments. At $Fo = 0.06$, the natural convection was further developed and a large vortex was formed in the middle region. The typical flow field simulated by the REV-scale method [86] is presented in Figure 2.11(b). It can be observed that the detailed flow through pores was ignored and the flow field was simplified.

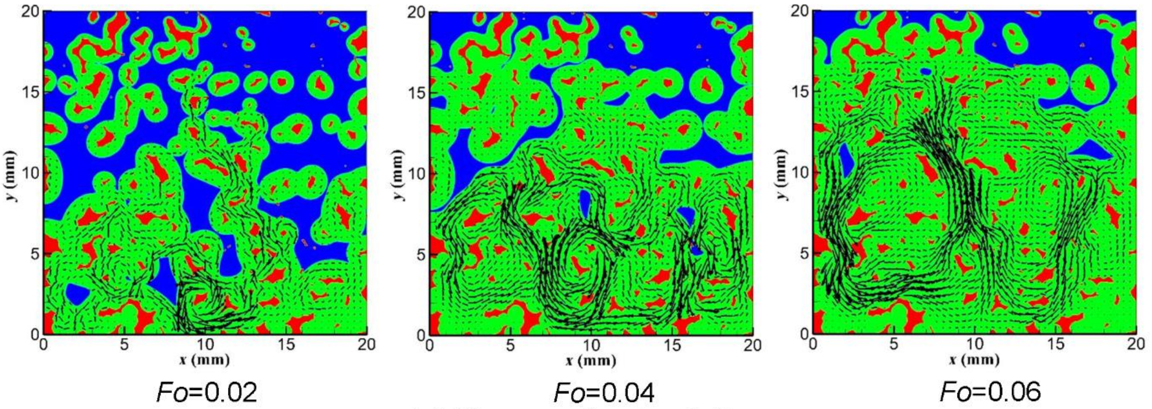

(a) Pore-scale simulation

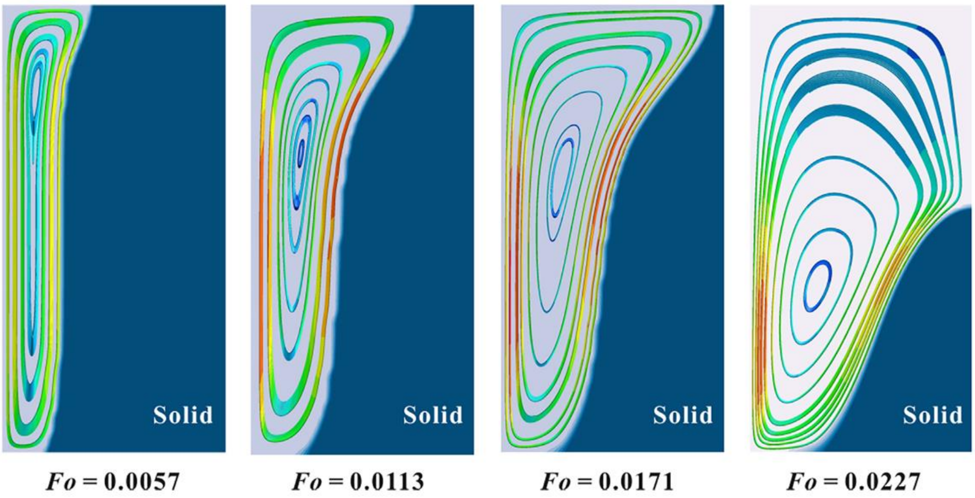

(b) REV-scale simulation

Figure 2.11: Comparison of flow fields predicted by different methods [86, 105].

2.3 Summary

In summary, metal foam is the most used porous skeleton in both experimental and numerical studies. The skeletons in all the reports are macroporous, in other words, studies on mesoporous, microporous and hierarchical porous CPCMs are very few. It may be because mesoporous, microporous and hierarchical porous CPCMs are shape-stabilised phase change materials (ss-PCMs). They are like bricks and the heat transfer in them can be regarded as single heat conduction, which makes the study on heat transfer relatively simple. Metal foam belongs to the macroporous skeleton. Actually, its pore size (> 0.1mm) is much larger than the classification limit, so natural convection can occur, beneficial to heat transfer. Moreover, foam and PCM can be produced in large sizes, which is suitable for large-scale applications. And they are produced separately; if the foam or PCM fails, we only need to maintain the single foam or salt. In contrast, for ss-PCMs, the skeleton and PCM are integrated together and cannot separate, thus the whole ss-PCM needs to be maintained, which obviously increases the maintenance cost. As a result, foam-typed skeletons are widely applied and investigated.

Paraffin is the most used PCM. The coverage of PCMs used in the previous research is very narrow. The phase change temperature of most PCMs is from 0 °C to 70 °C, falling in the range of low temperature. Studies on the medium- and high-temperature PCMs are very few. Inorganic salts are widely used PCMs in medium- and high-temperature applications due to their high melting point, large energy storage density, low cost and excellent chemical stability. However, salts also suffer from low thermal conductivity, like most PCMs. And they are highly corrosive, which makes many conventional heat transfer enhancement methods fail. Ceramic has inherently high thermal conductivity and corrosion resistance, but the potential of ceramic foam as the thermal enhancer of salts is poorly known, which hampers its practical applications. A comprehensive study covering material preparation, compatibility test, and thermal performance evaluation of ceramic foam/salt porous CPCMs is needed.

Chapter 3 - Thermo-physical properties of nitrate salts

3.1 Introduction

Thermo-physical properties of salts are fundamental information for the research on heat transfer. The melting point and latent heat are very important because the melting point determines the application range of salts and the latent heat determines the energy storage capacity. In this chapter, the melting point and latent heat of salts are investigated. Nitrate salts ($NaNO_3$, KNO_3 and their eutectics) are selected because they are the widely used salt in medium- and high-temperature thermal energy storage. First, the melting point and latent heat of nitrate salts are experimentally measured. The effect of components on thermo-physical properties is analysed. Then, a molecular dynamics (MD) simulation is performed to reveal the mechanism underlying the variation of thermal properties from the atomic point of view.

3.2 Experiments

$NaNO_3$ and KNO_3 (purity ≥ 99.0%) were purchased from China National Pharmaceutical Co., Ltd. The preparation of $NaNO_3$-KNO_3 eutectics is as follows: first, the pure $NaNO_3$ and KNO_3 were weighed and mixed together, followed by the full dissolution in the excess distilled water; then the solution was dried at 150 °C for more than 48 h; finally, the salt was ground for the later differential scanning calorimetry (DSC) measurement. The mole fraction of $NaNO_3$ in samples is listed in Table 3.1 and the photograph is shown in Figure 3.1.

The DSC measurement was conducted using Discovery DSC25 (TA Instruments, USA). The accuracy of the temperature control is ±0.01°C. The accuracy of the calorimeter (indium, the standard metal) is ±0.1%. The baseline reproducibility is < 40 μW. Nitrogen was employed as the cooling gas and the flow rate was 50 ml/min. Before the DSC measurement, the device was calibrated using the standard metal. The sample (10 mg) was placed in the alumina crucible while the empty crucible act as the reference. The sample was first heated to 150 °C and then subjected to a heating-cooling cycle with a rate of 6 °C /min. The first cycle was discarded and the data was acquired from the second cycle. Each salt was tested at least three times.

Table 3.1: Nitrate salts employed in the experiment.

No.	Name	Mole fraction of $NaNO_3$
0#	Na_0-K_1	0
1#	$Na_{0.1}$-$K_{0.9}$	0.1
2#	$Na_{0.2}$-$K_{0.8}$	0.2
3#	$Na_{0.3}$-$K_{0.7}$	0.3
4#	$Na_{0.4}$-$K_{0.6}$	0.4
5#	$Na_{0.5}$-$K_{0.5}$	0.5
6#	$Na_{0.6}$-$K_{0.4}$	0.6
7#	$Na_{0.7}$-$K_{0.3}$	0.7
8#	$Na_{0.8}$-$K_{0.2}$	0.8
9#	$Na_{0.9}$-$K_{0.1}$	0.9
10#	Na_1-K_0	1

Figure 3.1: Photograph of nitrate salts used in the experiment. From left to right is sample 0#, 1#, …, 10#.

3.3 Molecular dynamics simulation

A molecular dynamics simulation was performed to understand the variation of thermos-physical properties from atomic point of view. The simulation system consists of 5040 atoms.

The initial crystal structure is obtained from Ref. [108]. Then the cell is replicated to generate the final geometry. The mole fraction of $NaNO_3$ is the same as that in the experiment.

The Buckingham potential is used to reproduce the pairwise interaction between atoms [109, 110]:

$$E_{buck} = Ae^{-r/\tau} - \frac{C}{r^6} \tag{3-1}$$

where r is the distance between two atoms; A, τ and C are Buckingham parameters which are listed in Table 3.2.

Table 3.2: Buckingham potential parameters for $NaNO_3$ and KNO_3 [108].

	q /e	A /kcal mol^{-1}	τ /Å	C /kcal mol^{-1} Å^6
Na	+1	9778.06	0.3170	24.18
K	+1	35833.47	0.3370	349.9
N	+0.95	33652.75	0.2646	259.1
O	-0.65	62142.9	0.2392	259.4
N-O	k_b /kcal mol^{-1} Å^{-2} = 525.0		r_o / Å = 1.2676	
O-N-O	k_θ/kcal mol^{-1} rad^{-2} = 105.0		θ_0 /°= 120.0	
O-N-O-O	k_Ψ/kcal mol^{-1} rad^{-2} = 60.0		Ψ_0 /°= 0.0	

The intra-molecular force field is used to describe the force within the nitrate ion, where the bond stretching is computed as [108]:

$$V_b = k_b\ (r - r_0)^2 \tag{3-2}$$

Angle bending is computed as:

$$V_\theta = k_\theta\ (\theta - \theta_0)^2 \tag{3-3}$$

Improper motion is computed as:

$$V_\psi = k_\psi\ (\psi - \psi_0)^2 \tag{3-4}$$

Coulombic interaction is computed as:

$$E_{coul} = \frac{q_i q_j}{r} \tag{3-5}$$

where q_i and q_j are the charge of ions i and j.

For different types of atoms (such as Na and N), the pair coefficient is generated by the following mixing rules [109]:

$$A_{ij}=\sqrt{A_{ii}\cdot A_{jj}} \tag{3-6}$$

$$C_{ij}=\sqrt{C_{ii}\cdot C_{jj}} \tag{3-7}$$

$$\frac{1}{\tau_{ij}}=\frac{1}{\tau_{ii}}+\frac{1}{\tau_{jj}} \tag{3-8}$$

All the simulations were performed using the open-source MD software LAMMPS. The Buckingham and Coulombic interactions were truncated at 11 Å, with the long-range corrections being applied [108]. The particle-particle-particle-mesh (pppm) solver was used to compute long-range Coulombic interactions. Newton's motion equations were solved through the Verlet algorithm with a time step of 1 fs [111].

The system was first subjected to an energy minimization. Then it was equilibrated in the NPT ensemble for 2 ns to relax the system to the desired pressure and temperature [109]. The pressure was fixed as 0.1 MPa while the temperature ranged from 300 K to 800 K, so both the solid and liquid state can be covered. The temperature increment is 50 K; near the melting point, it is set as 10 K. During the simulation process, Nose-Hoover thermostat and barostat were employed to control the pressure and temperature.

In all the simulations, the "multi constant temperature" method rather than the "gradually heating and cooling" method was adopted so that the system can be equilibrated at each specific temperature for a long enough time [112].

3.4 Results and discussions

3.4.1 Melting point

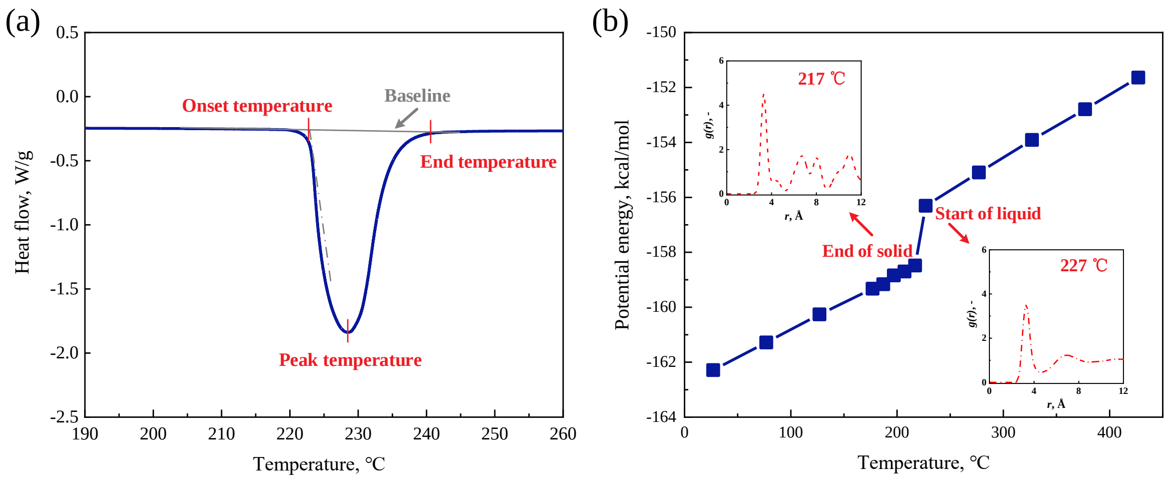

Figure 3.2: Determining the melting point of $Na_{0.5}$-$K_{0.5}$ using (a) DSC measurement and (b) MD simulation.

The schematic of determining the melting point using the DSC curve and potential energy curve is shown in Figure 3.2. For the DSC method, three melting temperatures are identified: the extrapolated onset temperature, peak temperature and end temperature [113]. For the MD method, the melting point is determined by the jump in the potential energy curve [114]. It is noted that in Figure 3.2(b), the potential energy jumps at 217 °C; the salt shows the solid characteristic, as seen from the Na-N radial distribution function (RDF). At 227 °C, the jump ends, and the salt shows the liquid feature, indicating the salt has been melted completely. Herein, the temperature where the jump starts is denoted as T_{solid} which means the end of the solid state; the temperature where the jump ends is denoted as T_{liquid} which means the start of the liquid state. For the $Na_{0.5}$-$K_{0.5}$, T_{solid} and T_{liquid} are 217 °C and 227 °C respectively.

The melting point determined by the DSC measurement and MD simulation is presented in Figure 3.3. It is seen that the pure $NaNO_3$ and KNO_3 have the highest melting point. And the melting point first decreases and then increases with the increasing ratio of $NaNO_3$, and the melting point of salt mixtures is lower than that of each component. The melting point in Ref. [115-117] is also plotted in Figure 3.3 and they show the same trend.

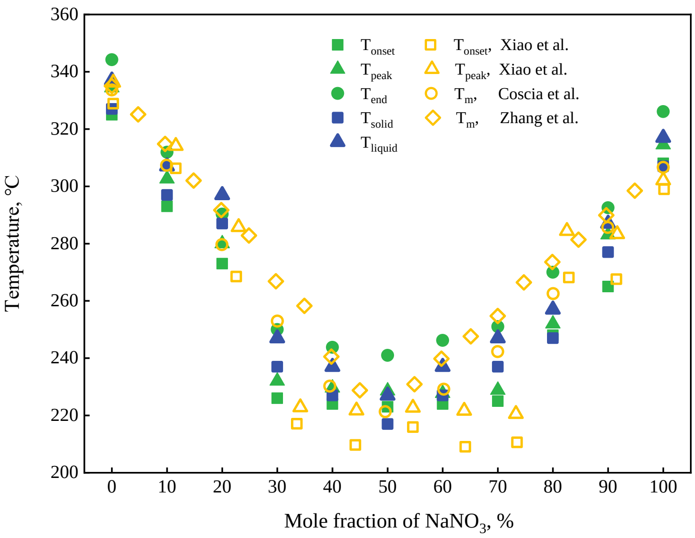

Figure 3.3: Variation of melting point with the mole fraction of $NaNO_3$.

The results indicate that $Na_{0.5}$-$K_{0.5}$ has the lowest melting point and the melting point is 100 °C lower than that of pure salt. To understand the component-dependent melting point, the structure of nitrate salts was analysed. The nitrate salt is a type of ionic crystal [118]. Na^+/K^+ are bonded with NO_3^- by the coulombic force, as shown in Figure 3.4. The coulombic force is the attractive force because the charge of Na^+/K^+ and NO_3^- are opposite. From the atomic point of view, the melting process is that, as the temperature increases, Na^+, K^+ and NO_3^- vibrate more intensively until they overcome the coulombic force and escape from the lattice point [119]. The coulombic force acts as the resistance for melting.

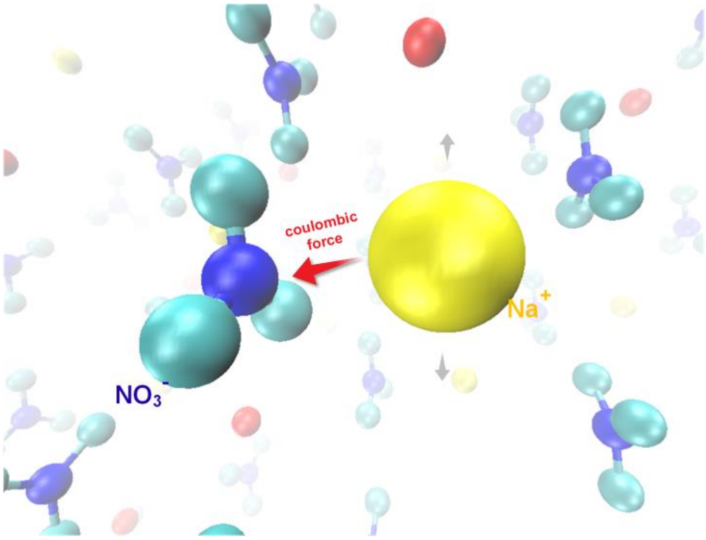

Figure 3.4: Schematic of the coulombic interaction in $NaNO_3/KNO_3$ eutectic. Yellow, red, blue and cyan spheres represent Na, K, N and O atoms respectively.

The coulombic energy computed from the MD simulation is presented in Figure 3.5. It is seen that $Na_{0.5}$-$K_{0.5}$ has the smallest coulombic energy. This suggests that the “resistance” for melting is small, so Na^+, K^+ and NO_3^- can shake out of the lattice point at a relatively low temperature, which may lead to the lowest melting point.

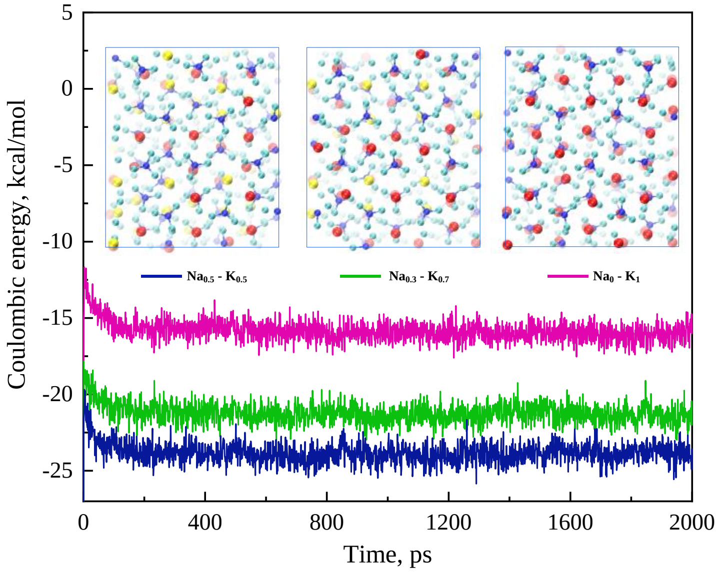

Figure 3.5: Computed coulombic bonding energy of Na_0-K_1, $Na_{0.3}$-$K_{0.7}$ and $Na_{0.5}$-$K_{0.5}$. Yellow, red, blue and cyan spheres represent Na, K, N and O atoms respectively.

3.4.2 Latent heat

The DSC curve describes the power difference between the tested sample and the reference. Since the empty crucible is used as the reference in the current experiment, the DSC curve indicates the amount of energy required by salt to reach the pre-set temperature. The schematic of determining the latent heat using the DSC curve is presented in Figure 3.6(a). The latent heat is obtained by integrating the area between the DSC curve and the baseline from the onset temperature to the end temperature [113]. Actually, the latent heat obtained by this method is the “pure” latent heat because the specific heat has been extracted. It reflects the energy increment induced by the phase change.

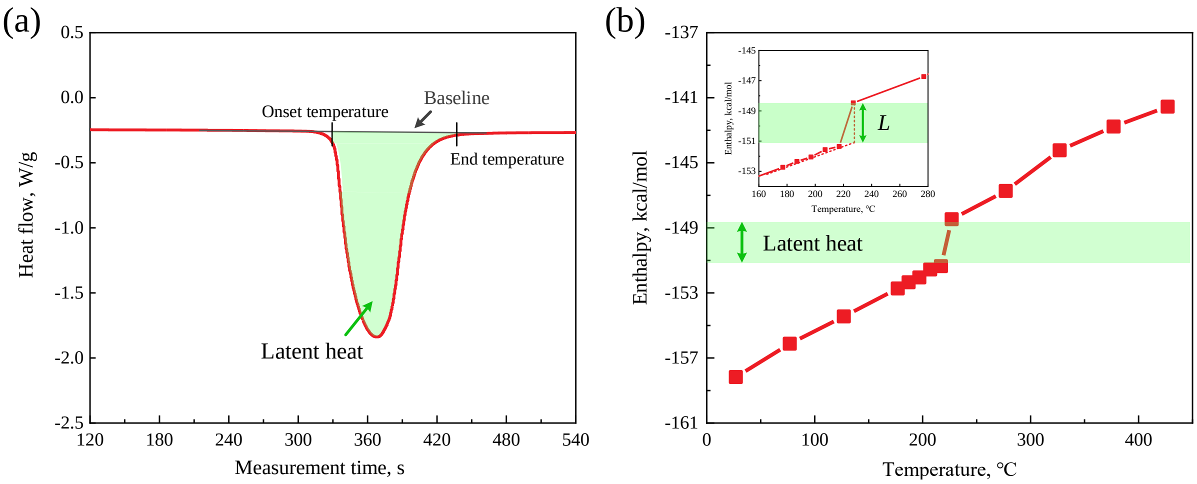

Figure 3.6: Determining the latent heat of $Na_{0.5}$-$K_{0.5}$ using (a) DSC measurement and (b) MD simulation.

The MD method determines the latent heat by identifying the jump in the enthalpy curve. Before melting, the enthalpy increases stably with temperature, which is mainly due to the specific heat. When the temperature reaches the melting point, the phase change occurs and the enthalpy jumps due to the phase change. The latent heat is obtained by computing the enthalpy difference before/after melting. The specific heat is extracted by extrapolating the enthalpy curve to T_{liquid}.

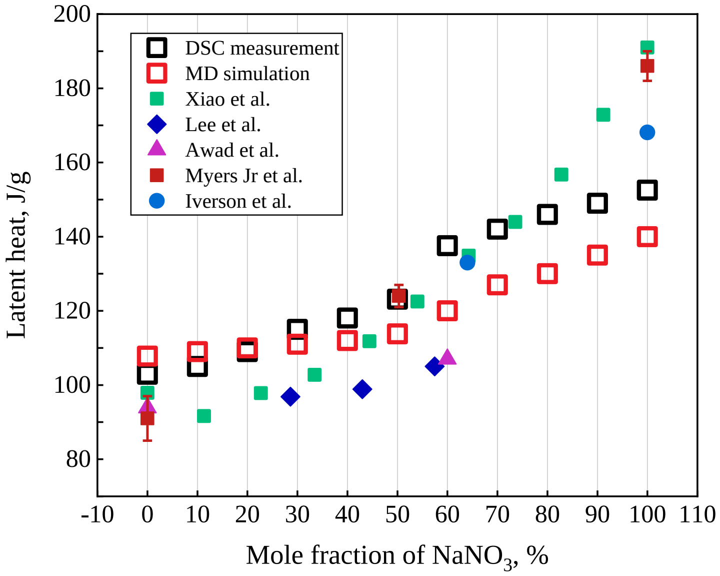

Figure 3.7: Variation of latent heat with the mole fraction of $NaNO_3$.

The latent heat of nitrate salts is presented in Figure 3.7. Different from the melting point, the latent heat increases with the increasing ratio of $NaNO_3$. It is proportional to the component. The latent heat in Ref. [115, 120-123] shows the same trend. The variation of latent heat with components is very important because through mixing pure salts, the melting point of the mixture is decreased while the energy storage density is not impaired.

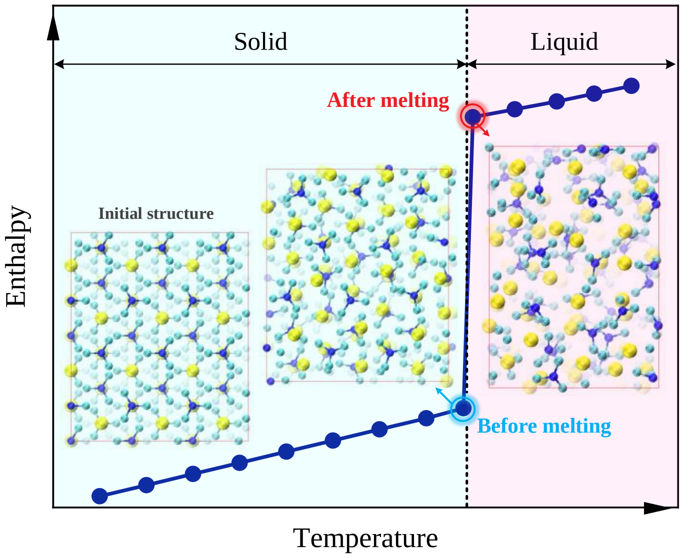

Figure 3.8: Schematic of the structure of $NaNO_3$ before/after melting. Yellow, blue and cyan spheres represent Na, N and O atoms respectively.

Latent heat is the energy difference before/after melting. Since the property of matter is determined by its structure, the component-dependent latent heat is explained from the salt structure. The initial structure of $NaNO_3$ is regular, as shown in Figure 3.8. Na^+ and NO_3^- are located at the lattice point and the structure has the characteristic of “point by point”. At the solid state, atoms vibrate “in place”; although the structure becomes a bit disordered, Na^+ and NO_3^- are still locked near the lattice point. The structure is overall “point by point”. However, after melting, Na^+ and NO_3^- distribute randomly; the structure is quite disordered.

The coordination number describes the number of atoms surrounding the central atom. It is calculated by [111]:

$$N = 4\pi p_j \int_0^r g_{ij}(r) r^2 dr \tag{3-9}$$

where i and j denote i–type and j–type atom, respectively; p_i is the number density of j–type atom; r is the distance between i–type and j–type atoms; g_{ij} is the radial distribution function. Taking $r = r_{\min}$ ($r_{\min}$ is the first valley position of the RDF curve), the coordination number is obtained. Figure 3.9 shows the coordination number curves of Na$_1$-K$_0$, Na$_{0.5}$-K$_{0.5}$, and Na$_0$-K$_1$. The temperature of "before melting" and "after melting" for Na$_1$-K$_0$, Na$_{0.5}$-K$_{0.5}$, and Na$_0$-K$_1$ is 580 K and 590 K, 490 K and 500 K, 600 K and 610 K respectively. The solid line represents the coordination number curve "before melting" while the dashed line represents "after melting". The first valley position of the RDF curves is located at around 4.75 Å. The height of the red, black and blue rectangular in Figure 3.9 represents the difference in the coordination number before/after melting. It is seen that the difference in coordination number before/after melting is Na$_1$-K$_0$, Na$_{0.5}$-K$_{0.5}$, and Na$_0$-K$_1$ in order from large to small. The larger the difference in coordination number, the greater the change in the local structure, the more the energy is required to meet the change in the structure, which may lead to the larger latent heat.

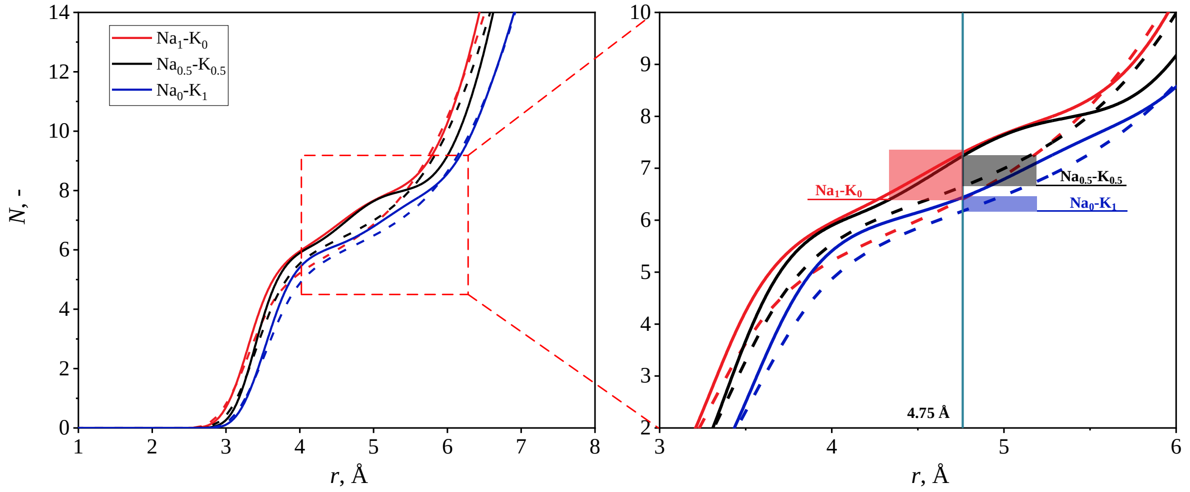

Figure 3.9: Coordination number curve of Na$_1$-K$_0$, Na$_{0.5}$-K$_{0.5}$, and Na$_0$-K$_1$.

3.4.3 Potential application

In addition to providing the fundamental thermal properties for later research on heat transfer, the potential application of the current research is to improve the efficiency of solar power plants. From the above discussion, it can be concluded that mixing pure salts can decrease the melting point and does not impair the latent heat. It is very important especially for cloudy days and winter because the sunshine is not strong on these days. If the melting point of salt is too high, the weak sunshine cannot heat the salt to melt, so the energy storage through phase change cannot be achieved. The method of mixing pure salts extends the application range of salts as PCM. A potential application is using the low-melting-point eutectic salt in solar power plants (Figure 3.10, the detailed working flow is introduced in Chapter 8). Although the sunshine is weak on cloudy days or winter, since the melting point of the eutectic salt is low, the concentrated solar energy is still possible to melt the salt. Thermal energy is stored in the form of latent heat, which provides heat to generate power, improving the efficiency of power plants.

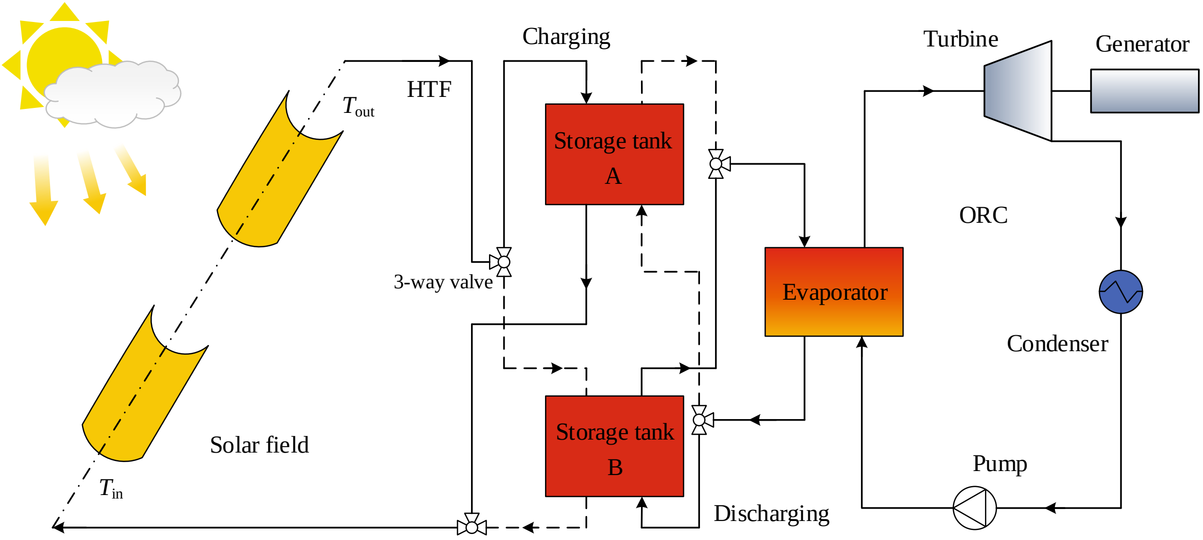

Figure 3.10: Schematic of the application of the low-melting-point eutectic salt in solar power plant on cloudy days.

3.5 Summary

The component-dependent thermo-physical properties of nitrate salts were measured and analysed. The mole fraction of $NaNO_3$ is 0, 0.1, …, 1. A molecular dynamics simulation was performed to explore the mechanism. It is found that the melting point first decreases and then increases with the increasing ratio of $NaNO_3$. The melting point of all eutectic salts is lower than pure salt and the maximum decrease is over 100 °C. By contrast, the latent heat is almost proportional to components and is not impaired by mixing pure salts. The molecular dynamics simulation results indicate that low coulombic bonding energy may lead to the decreased melting point while the difference in coordination number before/after melting is correlated with the variation in latent heat.

Chapter 4 - Preparation of ceramic foam/salt CPCM

4.1 Introduction

Ceramic has inherently high thermal conductivity and corrosion resistance. And its cost is much lower than that of metal. So, the ceramic foam can be a suitable thermal enhancer for salts. This chapter introduces the preparation of ceramic foam/salt CPCM. The dipping method is used as the preparation technique and the industrial SiC ceramic powder as the base material to reduce the cost. And the wettability of the prepared ceramic is tested to determine the impregnation method. This work provides the material for later research on compatibility and thermal transport.

4.2 Materials

The polyurethane (PU) foam was purchased from Yueyang Sponge Co., Ltd. Industrial grade SiC ceramic powder (particle size:10 μm - 13 μm) was supplied by Xianfeng Material Co., Ltd. It was used as the base material of the ceramic foam. Kaolin, alumina, yttrium oxide and polyvinyl alcohol were purchased from Yousuo Chemical Co., Ltd. N-octanol were purchased from Kermel Chemical Co., Ltd. $NaNO_3$ and KNO_3 (purity $\geq$ 99.0%) were supplied by China National Pharmaceutical Co., Ltd. The nitrate salts were utilised to prepare solar salt (60wt% $NaNO_3$ + 40wt% KNO_3) which is a widely used salt in medium-temperature thermal energy storage.

4.3 Preparation process

The dipping method was employed to prepare the ceramic foam. This technique is able to fabricate large sized products, which is suitable for practical applications. And PU foam can be cut into various shapes such as cubic and annular so that ceramic foam with the corresponding shape can be produced and applied in the cavity or shell-and-tube containers.

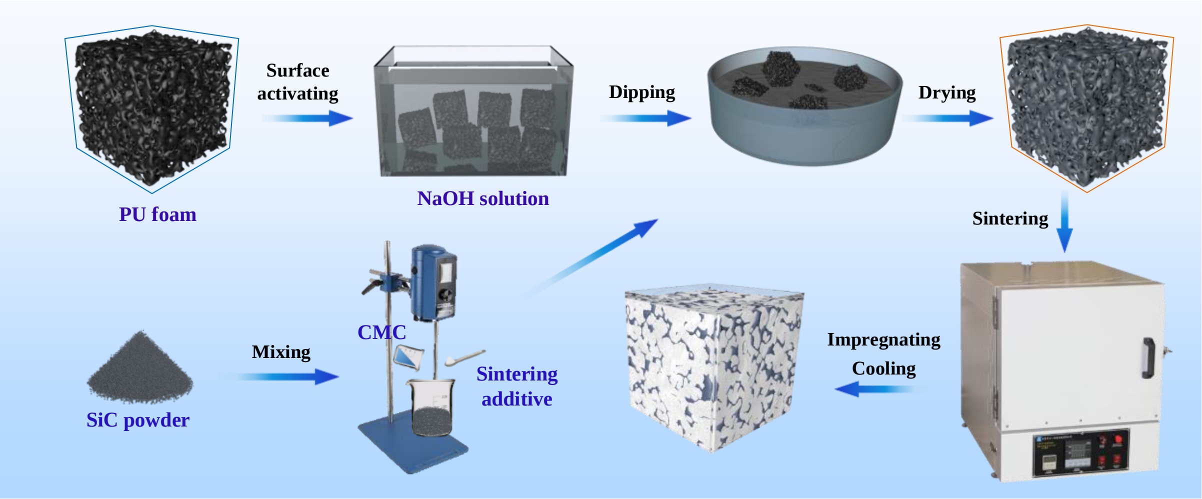

Figure 4.1: Schematic of the preparation process of ceramic foam/salt CPCM.

Table 4.1: Components of ceramic slurry.

	Component	Mass fraction, %	Role
Solid phase	SiC powder	67.0	Base material
	Kaolin	5.5	Sintering additive
	Alumina	3.1	Sintering additive
	Yttrium oxide	2.3	Sintering additive
Liquid phase	CMC	17.8	Tackifier
	Sodium polyacrylate	0.2	Dispersant
	N-octanol	0.1	Defoamer
	Silica sol	3.7	Adhesive
	Polyvinyl alcohol	0.3	Adhesive

The schematic of preparation process of ceramic foam/salt CPCM is shown in Figure 4.1. First, the PU foam (dimension: 50 mm × 50 mm × 50 mm) was submerged in NaOH solution (concentration: 10wt%) for 12 hours to activate the surface [124]. Then, it was dipped in the ceramic slurry. The solid phase of the slurry includes SiC powder, kaolin, alumina and yttrium oxide. Their mass fractions are listed in Table 4.1. Next, carboxymethylcellulose sodium (CMC) was added to increase the viscosity. Sodium polyacrylate and N-octanol were added as the dispersant and defoamer respectively. Silica sol and polyvinyl alcohol were added to improve the adhesion of the ceramic slurry to PU foam. All the components, mass fractions and roles are listed in Table 4.1.

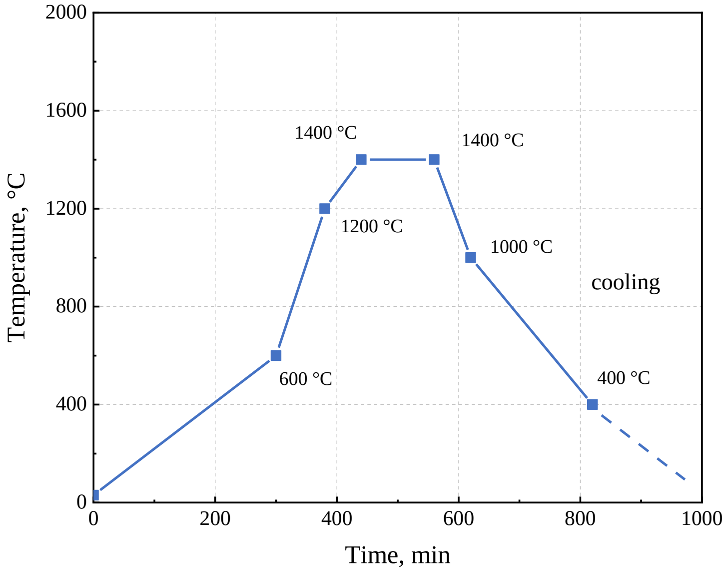

Figure 4.2: The sintering curve of ceramic foam (the dashed line means natural cooling).

The ceramic slurry was first let stand for 24 hours. Subsequently, PU foams were dipped in the slurry and then squeezed using a roller machine to remove the excess slurry. Next, they were dried at 80 °C for 6 hours, followed by sintering in a furnace. The sintering curve is shown in Figure 4.2. Both the drying and the sintering are in the air atmosphere. Figure 4.3 shows the photograph of prepared ceramic foams (porosity = 0.85).

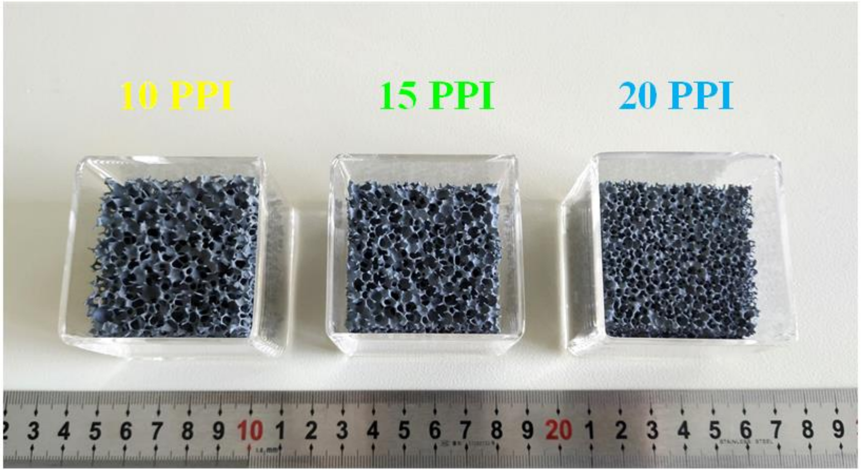

Figure 4.3: Photograph of ceramic foams with pore density of 10 PPI (Pores Per Inch), 15 PPI and 20 PPI.

4.4 Wettability test

The wettability of the prepared ceramic to salts is very important because it determines the impregnation method. If the ceramic is hydrophobic, vacuum impregnation is required to achieve a high loading. Since only at a high temperature can salt be melted, the vacuum condition along with the high temperature no doubt increases the cost of production. In contrast, if the ceramic is hydrophilic, the atmospheric impregnation is enough to achieve a high loading. The requirement on the equipment is lowered and the cost of production would be reduced.

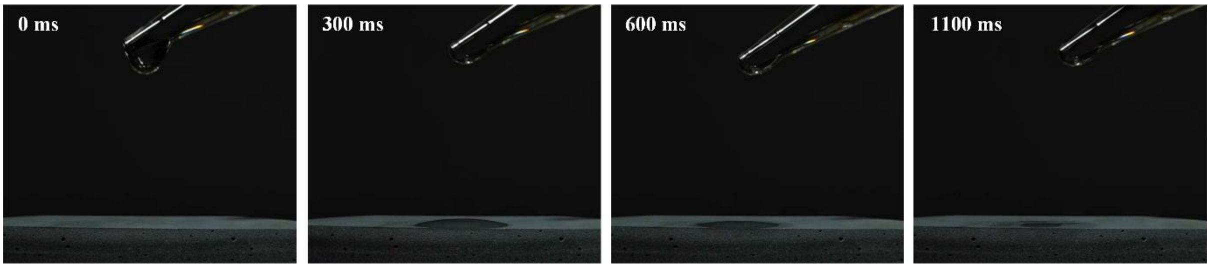

Figure 4.4: Wetting behaviour of the melted salt drop on the ceramic substrate.

The wettability was tested by dropping the liquid salt drop on the ceramic substrate. The bulk ceramic was sintered and was cut into a 5 cm × 5 cm × 1 cm piece. Then it was placed on a copper plate heater. The temperature of the cooper heater was kept at 300 °C which was higher than the upper limit of the melting point of solar salt (246 °C). This setting makes sure that the solar salt on the ceramic substrate is in a liquid state. The solar salt in a beaker was heated to melt. Then a straw was used to suck up the liquid salt. Next, the liquid salt was dropped on the ceramic substrate. As Figure 4.4 shows, the drop infiltrates into the ceramic substrate easily, indicating the ceramic has excellent wettability to solar salt.

The excellent wettability should be attributed to two factors. First, both ceramic and salt are inorganics, so the ceramic is prone to have good wettability to salt. Second, there are many pores at the surface of the ceramic, as shown in Figure 4.5. The size of the large pore exceeds 100 μm while that of the small pore is less than 1 μm. Although the ceramic piece has been polished, the surface is still uneven. The porous structure also improves the wettability.

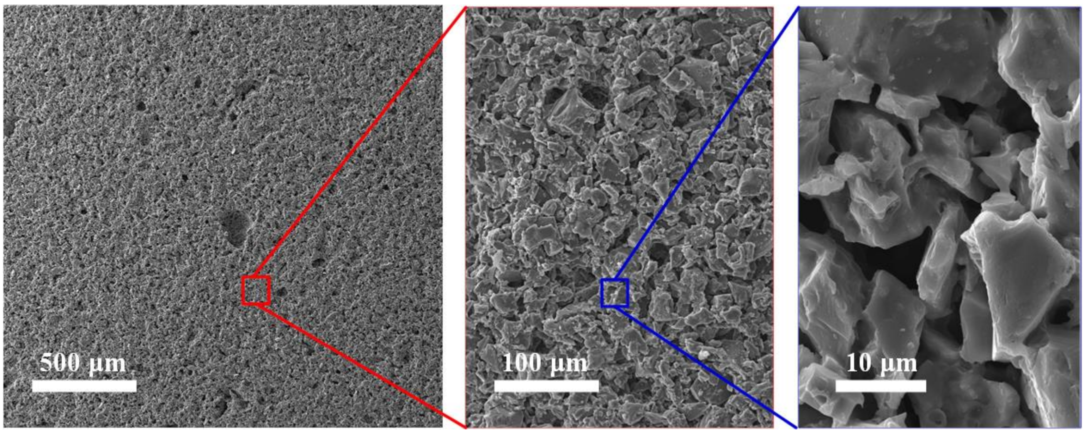

Figure 4.5: Surface morphology of the ceramic.

The wettability is very important for integrating PCM with foam. Vacuum impregnation (the schematic of the process is shown in Figure 2.2) is usually employed to integrate low-temperature PCMs with metal foam to improve the loading [11]. However, for salts, it is difficult to obtain the vacuum condition along with the high-temperature environment; and the equipment cost will be increased greatly. The excellent wettability of ceramic enables the atmospheric impregnation to achieve a high loading so the cost of the impregnation process can be reduced.

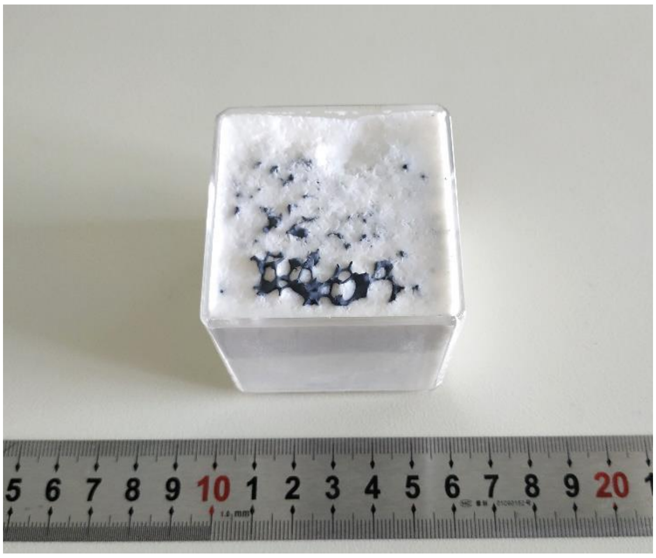

Figure 4.6: Photograph of ceramic foam/salt CPCM.

The ceramic foam was placed in a quartz cavity. The solar salt was heated to melt and then poured into the cavity. After cooling, the ceramic foam/salt CPCM was obtained. The dimension of CPCM is 50 mm × 50 mm × 50 mm and the impregnation ratio is over 95%. The photograph of ceramic foam/salt CPCM is shown in Figure 4.6.

4.5 Summary

Ceramic foams with different pore configurations were fabricated. The dipping method and industrial SiC power were employed to reduce the cost, removing the economic barriers in the way of potential applications. Additionally, the wettability of ceramic to salts was tested. The prepared ceramic shows excellent wettability to salt, which enables atmospheric impregnation to achieve a high loading, reducing the requirement on equipment and the impregnation cost. The ceramic foam/salt CPCMs were prepared, which provides the material for later research on compatibility and thermal transport.

Chapter 5 - Compatibility between ceramic and salt

5.1 Introduction

One of the challenges of salt-based PCM is corrosion. As not all ceramics are corrosion resistant [125, 126], it is essential to check the corrosion resistance of the prepared ceramic first before evaluating its heat transfer enhancement performance. In this chapter, the compatibility between the prepared ceramic and salt is tested through 50, 100 and 200 melting/solidification cycles. Corrosion behaviours of ceramic are analysed using various characterising technologies, such as scanning electron microscope (SEM), energy-dispersive spectroscopy (EDS), X-ray diffraction (XRD) and Raman. The corrosion experiment of Cu and Al is also conducted to make a comparison. In addition, a reactive molecular dynamics simulation is performed to provide microscopic insights into corrosion behaviours of ceramic. This study confirms the compatibility between ceramic and salt, laying the foundation for later research on thermal transport.

5.2 Experiments

PU (polyurethane) foam is used as the carrier of ceramic slurry to help form the porous geometry during the preparation process of ceramic foam. At about 500 °C, PU foam decomposes completely, as Figure 5.1 shows. So the component of ceramic foam is only the ceramic, without PU. The bulk ceramic was fabricated using the same raw materials and technique as the ceramic foam. And as corrosion is mainly a chemical reaction, the corrosion behaviours of the bulk ceramic should be the same as that of the ceramic foam. The bulk ceramic was cut into pieces with the size of 10 mm × 10 mm × 2 mm. Ceramic pieces were used in the compatibility test. Compared to ceramic foam, the advantage of a ceramic piece is that it is very easy to obtain a plane. Before the test, the sample needs to be polished; after the test, the sample needs to be characterised. The advantage makes the two steps achieved very easily.

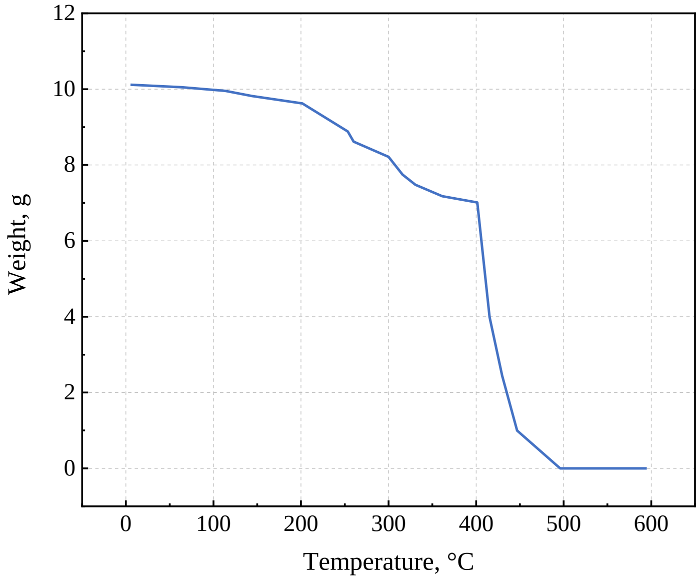

Figure 5.1: Thermogravimetric analysis of PU foam.

Figure 5.2 presents the flow chart of the corrosion test. Ceramic pieces were first polished and dried. Then, they were placed into alumina crucibles and buried by the solar salt (60wt% $NaNO_3$ + 40wt% KNO_3). The crucibles were transferred to the furnace and heated from 150 °C to 300 °C with a heating rate of 10 °C /min. Then the temperature was kept at 300 °C for 30 min to melt the solar salt completely. Subsequently, samples were cooled to 150 °C with a rate of 4 °C /min, followed by cooling at 150 °C for 60 min.

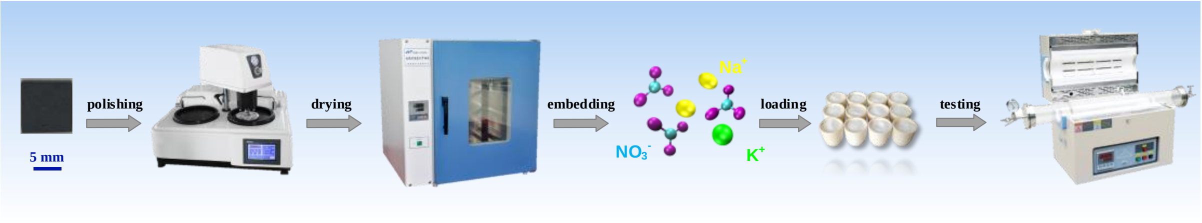

Figure 5.2: Schematic of the corrosion test process.

There are four groups in the experiment: the first is the reference group with 0 melting/solidification cycle; the second, third and fourth group had 50, 100 and 200 cycles respectively. When the melting/solidification cycles were finished, samples were first washed using the flowing water to remove the salt on the surface. Then they were ultrasonically washed in the distilled water for 5 min to further remove the salt. Finally, they were dried at 40 °C for

3 h. SEM, EDS (VEGA3, Tescan Instrument Co., Ltd), XRD (MAXima XRD-7000, Shimadzu Technology Co., Ltd) and Raman spectrometer (DXR SmartRaman, Thermo Fisher Scientific Inc.) were used to characterise ceramic pieces. The corrosion experiment of Cu and Al were also conducted to make a comparison. Each metal also had four groups: reference group (0 cycle), 50 cycles group, 100 cycles group and 200 cycles group. The experimental condition of the metal was the same as ceramic.

5.3 Molecular dynamics simulation

5.3.1 ReaxFF method

A ReaxFF reactive molecular dynamics (MD) simulation was performed to provide microscopic insights into corrosion behaviours of SiC ceramic. It allows the breaking and forming of bonds and is specifically designed to describe chemical reactions [127-130].

The ReaxFF energy term is given by [131]:

$$E_{\text{total}} = E_{\text{bond}} + E_{\text{under}} + E_{\text{over}} + E_{\text{val}} + E_{\text{tors}} + E_{\text{lp}} + E_{\text{H-bond}} + E_{\text{vdW}} + E_{\text{Coulomb}} \qquad (5\text{-}1)$$

where E_{bond} is the bond energy; E_{under} and E_{over} are the undercoordination penalty energy and overcoordination penalty energy respectively; E_{val} is the valence angle energy; E_{tors} is torsion angle energy; E_{lp} is long-pair energy; $E_{\text{H-bond}}$ is hydrogen-bond energy. These terms are bond-order dependent. E_{vdW} and E_{Coulomb} are van der Waals energy and coulombic energy, which are bond-order independent. E_{Coulomb} is taken into account for all atom pairs. Charge values are determined at each time step, which makes it possible to describe charge transfer during a chemical reaction.

5.3.2 Computational details

Since the main component of ceramic is SiC, only SiC was considered in the reactive MD simulation. The simulation box contains a slab of SiC in the presence of solar salt. The SiC slab consists of 12 layers and each layer has 32 atoms. The vacuum region with 19.5 Å is filled with $NaNO_3$ and KNO_3 molecules. Previous studies have confirmed that the size effect of SiC can be ignored when the slab is larger than 11 layers with a 12.5 Å vacuum region [132]. One end of the SiC slab is Si-terminated while the other is C-terminated. $NaNO_3$/KNO_3 is placed at the end sides of the SiC slab. This configuration enables the possible chemical reaction of both Si and C species. The salt system at each end consists of 45 $NaNO_3$ molecules and 25 KNO_3 molecules. The mass ratio is about 6: 4, which is consistent with the real solar salt. A snapshot of the simulation box is shown in Figure 5.3.

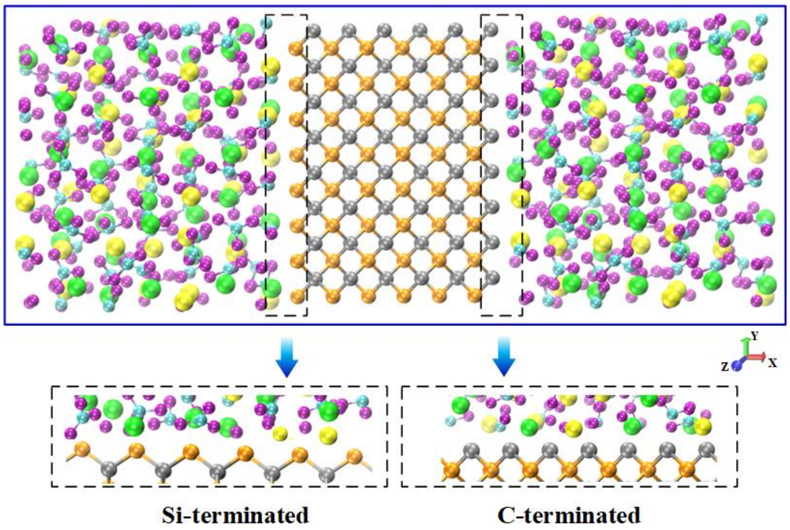

Figure 5.3: A snapshot of the simulation box. Gray, orange, yellow, green, purple and cyan spheres represent C, Si, Na, K, O and N atoms respectively.

The LAMMPs package was used to conduct all the simulations [133]. Simulations were carried out in NVT ensemble with a timestep of 0.25 fs and Nosè-Hoover thermostat. Periodic boundary conditions were employed in three dimensions and the conjugate gradient algorithm was used for energy minimization. The ReaxFF force field developed by Newsome et al. [134] was adopted in this study. The system was first heated to 300 °C and kept for 1 ns; then it was cooled to 150 °C. Finally, the system was kept at 150 °C for 1 ns. The heating/cooling was carried out 50, 100, 150 and 200 times to reproduce the melting/solidification process. The damping parameter which determines how rapidly the temperature was relaxed was set as 100 fs.

5.4 Results and discussions

5.4.1 Corrosion analysis

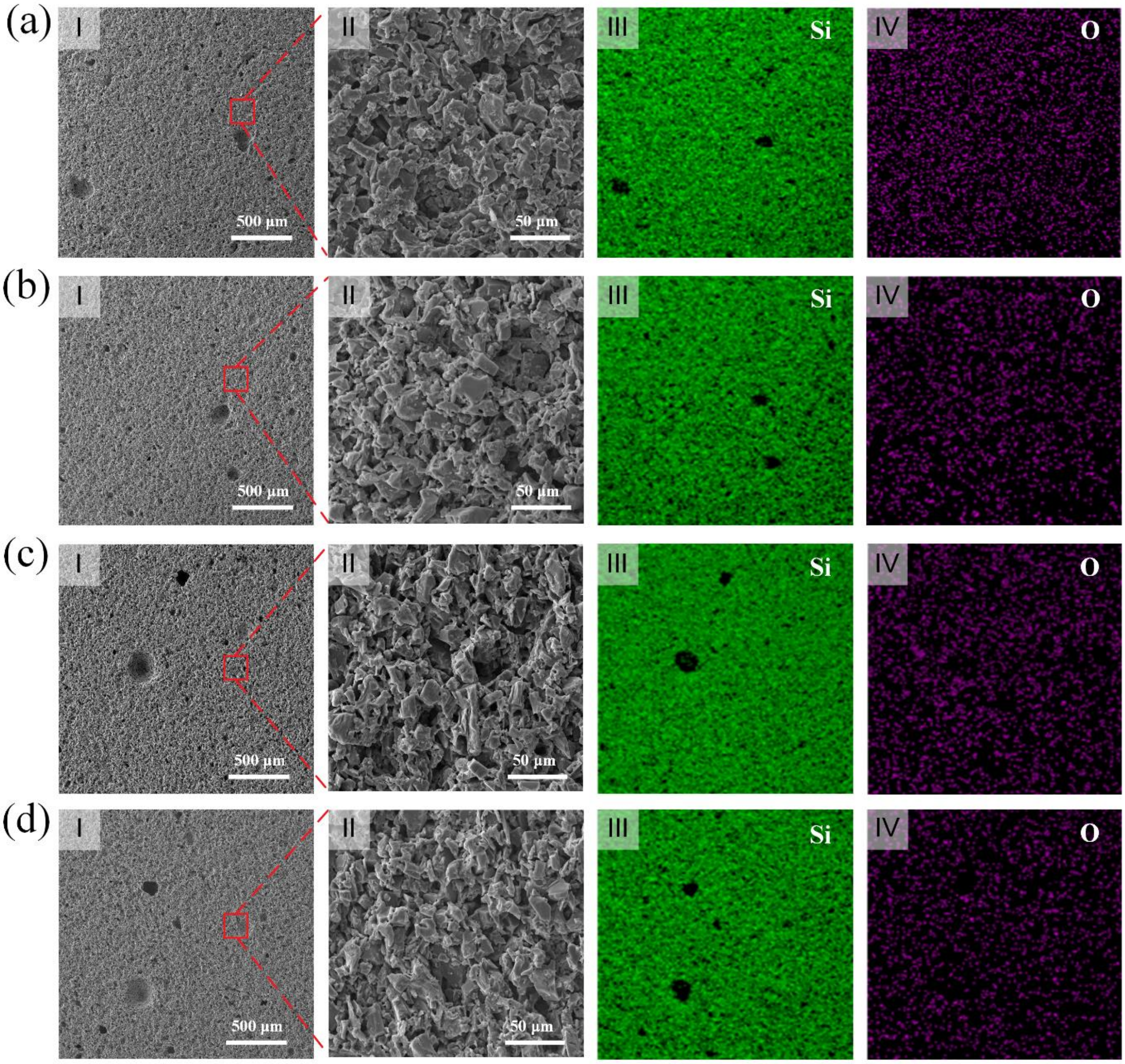

Figure 5.4: Surface morphology and EDS mappings of ceramic pieces: (a) the reference group, (b) 50 melting/solidification cycles group, (c) 100 cycles group and (d) 200 cycles group.

The surface morphology of ceramic pieces under different melting/solidification cycles is presented in Figure 5.4. It is seen that all the ceramic pieces have many pores on the surface. The high magnification images show that the edges of SiC grains are sharp. The angular structure of SiC grains can be observed in both the reference group and the test groups, suggesting that SiC grains are not corroded by solar salt. It is seen from EDS mappings that Si and O elements distribute uniformly on the ceramic surface; other elements including C, Na, K and N also distribute uniformly, as Figures 5.5-5.7 show. These elements do not aggregate significantly, indicating that there are no or little corrosion products on the surface.

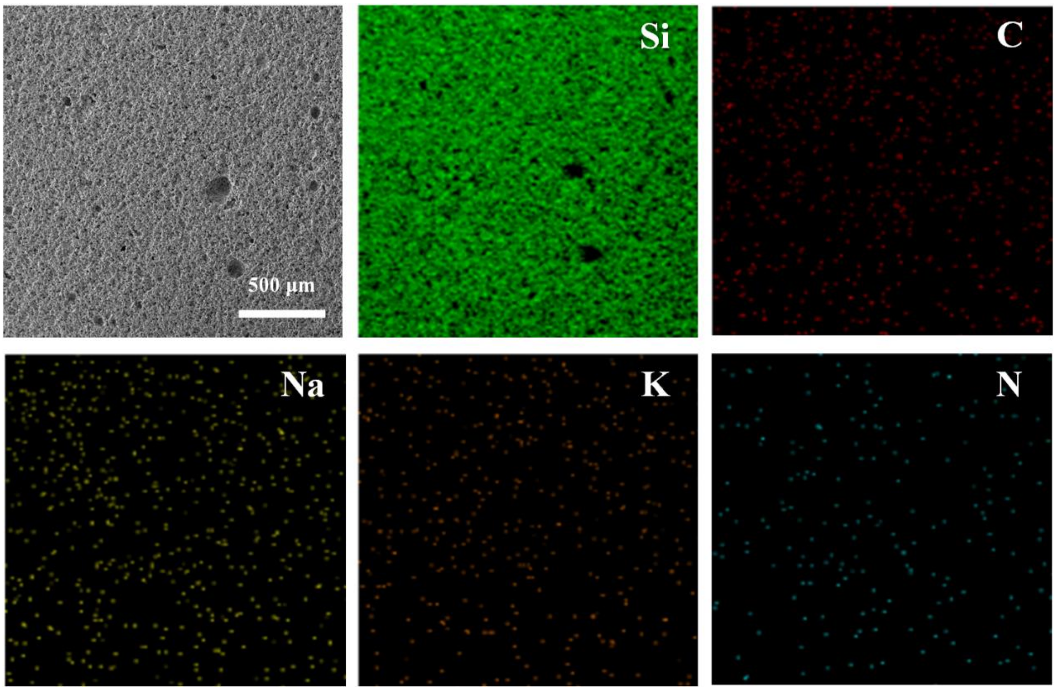

Figure 5.5: Surface morphology and EDS mappings of ceramic piece after 50 melting/solidification cycles.

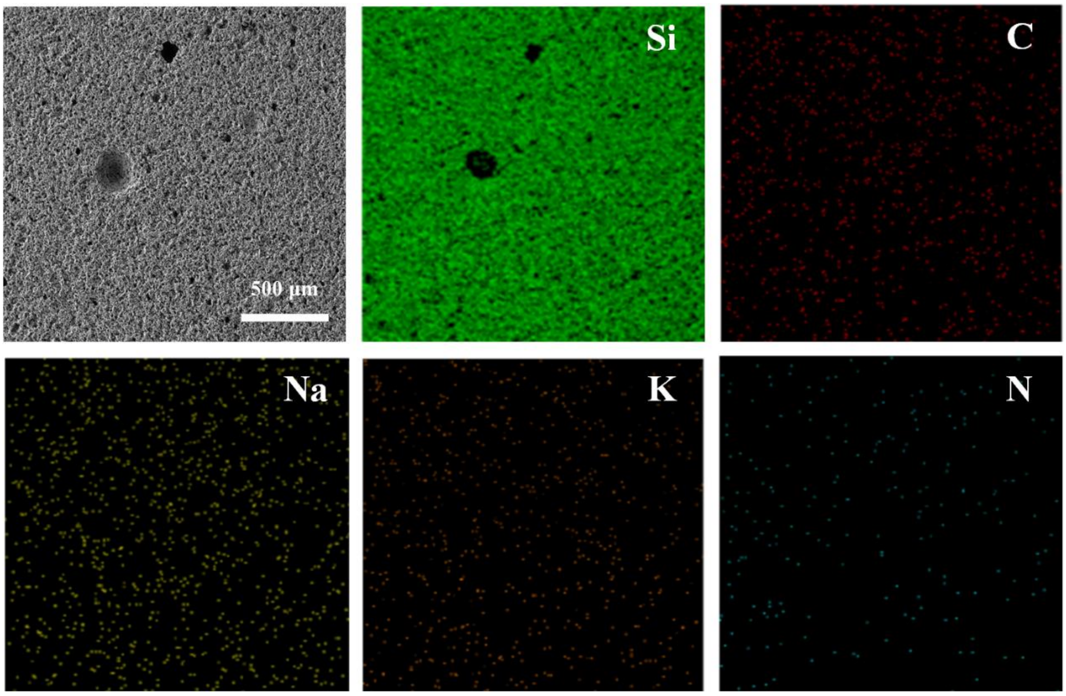

Figure 5.6: Surface morphology and EDS mappings of ceramic piece after 100 melting/solidification cycles.

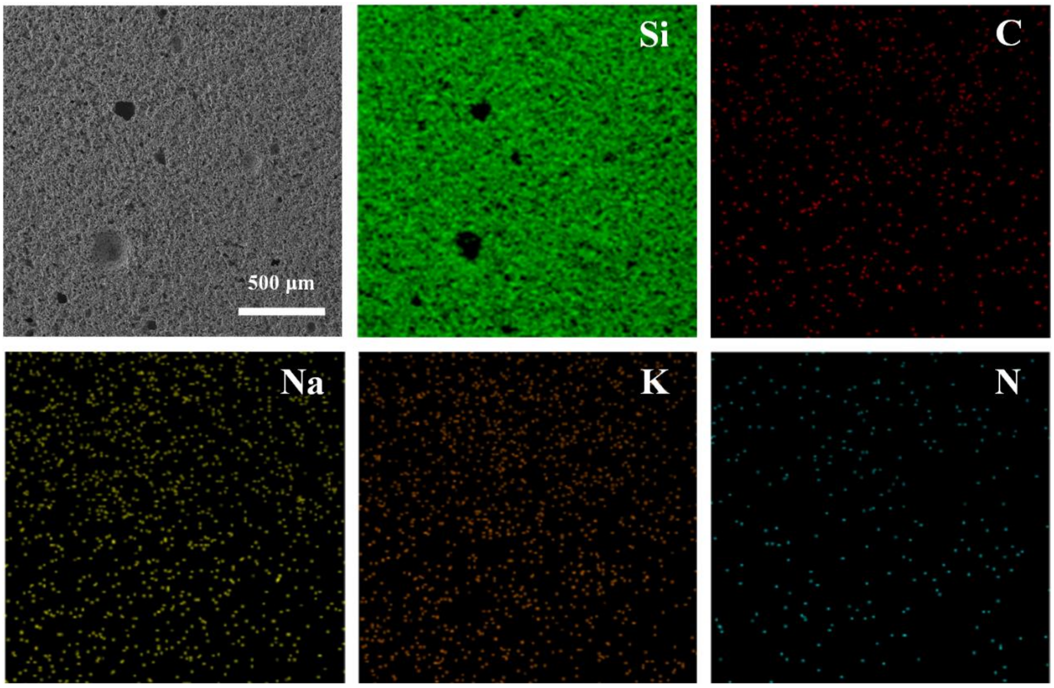

Figure 5.7: Surface morphology and EDS mappings of ceramic piece after 200 melting/solidification cycles.

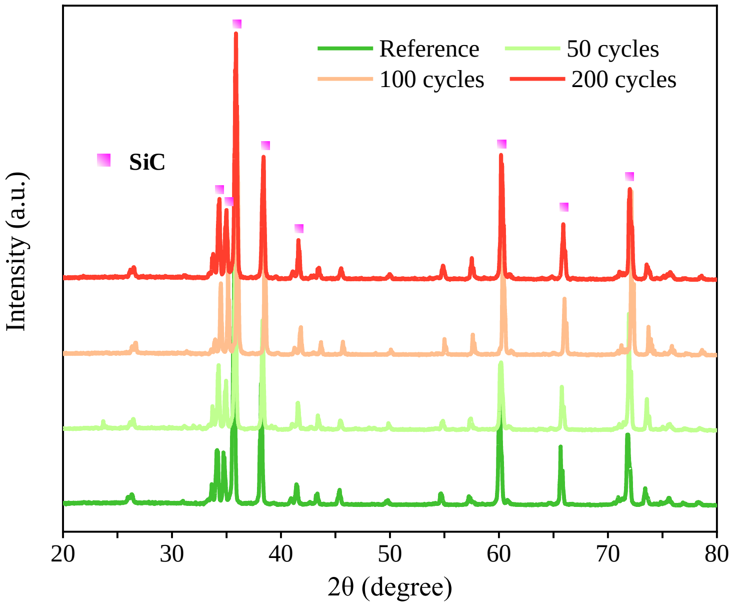

Figure 5.8: XRD patterns of the ceramics in reference group and melting/solidification cycles groups.

The XRD patterns of ceramics are presented in Figure 5.8. The peak at 2θ = 34.09°, 34.72°, 35.65°, 38.13°, 41.38°, 59.99°, 65.62° and 71.74° corresponds to the surface (3 1 1), (1 0 1), (0 0 4), (1 0 2), (4 0 0), (1 1 0), (1 0 6) and (1 1 4) of SiC respectively [135]. The diffraction peaks are narrow and sharp, indicating high crystallinity. After the corrosion test, there is no new phase and the main phase is still SiC. And the diffraction peaks remain sharp, indicating there are no defects caused by corrosion and the crystal structure is stable.

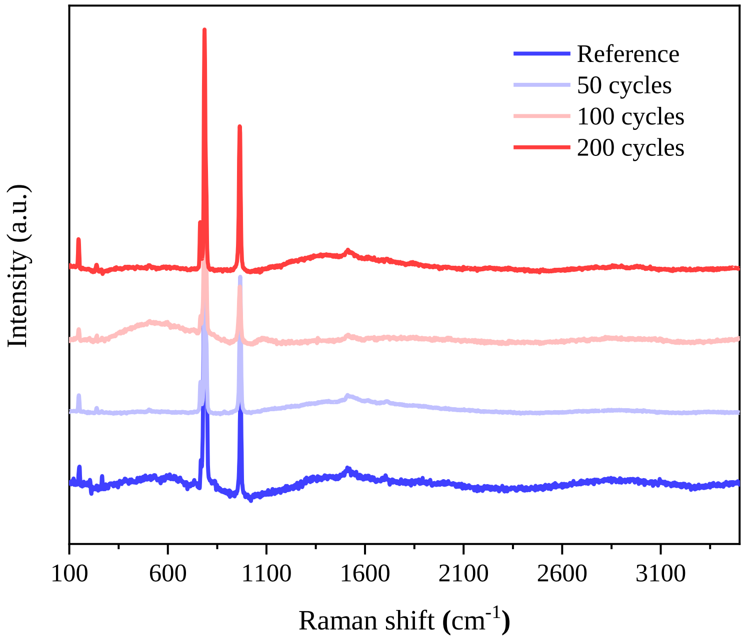

Figure 5.9: Raman spectroscopy of the ceramics in reference group and melting/solidification cycles groups.

Figure 5.9 shows the Raman spectroscopy. In the reference group, the Raman scattering mainly occurs at shifts = 786 cm^{-1} and 964 cm^{-1}. Some weak Raman bands are found at 147 cm^{-1} and 766 cm^{-1}, which should be attributed to disorder crystals and impurities. After the corrosion test, the Raman spectroscopy of ceramics is almost unchanged, indicating the low degree of reaction between the ceramic and solar salt.

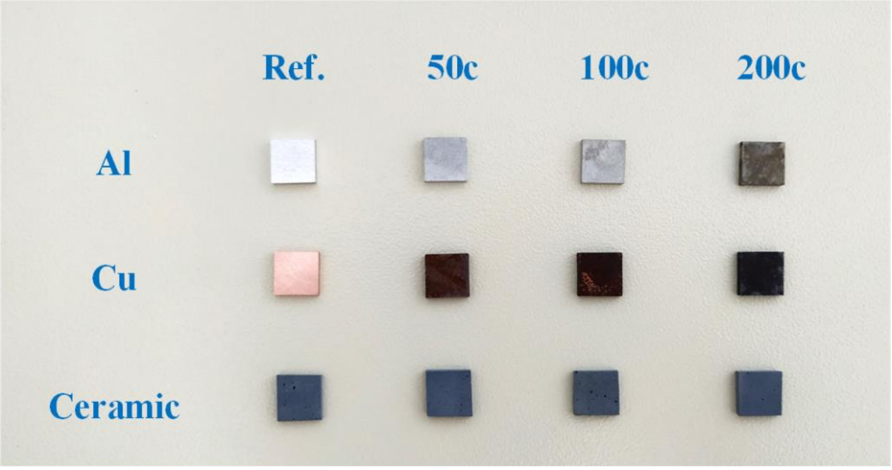

Figure 5.10: Photographs of ceramic, Al and Cu pieces under different melting/solidification cycles.

Cu and Al – the widely used thermal enhancers in low-temperature PCMs – are also tested and the results are shown in Figure 5.10. After 50 cycles, the surface of Al and Cu pieces becomes dull. As the cycle increases, the metal is corroded more seriously. In contrast, the surface of the ceramic keeps almost unchanged. It can be concluded that the prepared ceramic has excellent corrosion-resistant performance.

5.4.2 Microscopic insights

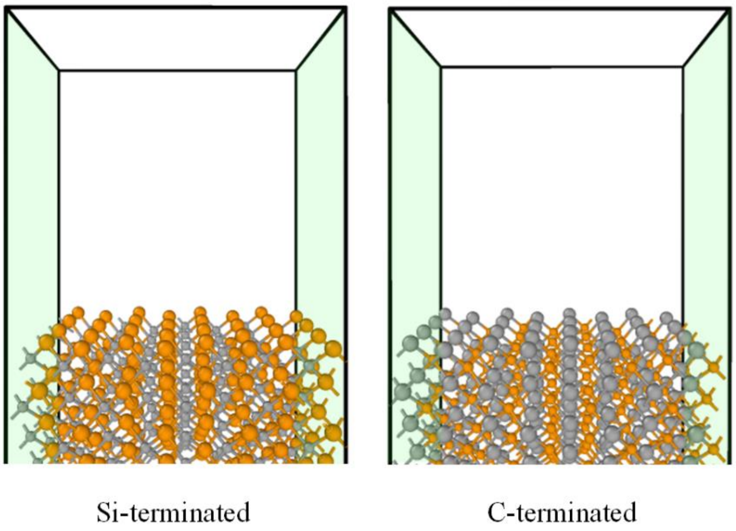

Figure 5.11: Morphology of SiC after 200 melting/solidification cycles. Orange and grey spheres represent Si and C atoms respectively.

Figure 5.11 shows the morphology of SiC after 200 melting/solidification cycles from the MD simulation. It is seen that Si and C atoms do not physically dissolve into the salt. It is because SiC is a covalent compound and the bonding energy is very high, up to 135 kcal/mol [136, 137]. The strong covalent bond makes it difficult for Si and C atoms to separate from the bulk.

Figure 5.12 presents the radial distribution functions (RDFs) of Si-N and Si-O pairs in the Si-terminated domain and C-N and C-O pairs in the C-terminated domain. Since atoms at the surface are more likely to react, only those atoms are counted in the calculation of RDFs. The salt domain is divided into five layers according to the distance from the SiC surface. Atoms of salt in the nearest layer are counted.

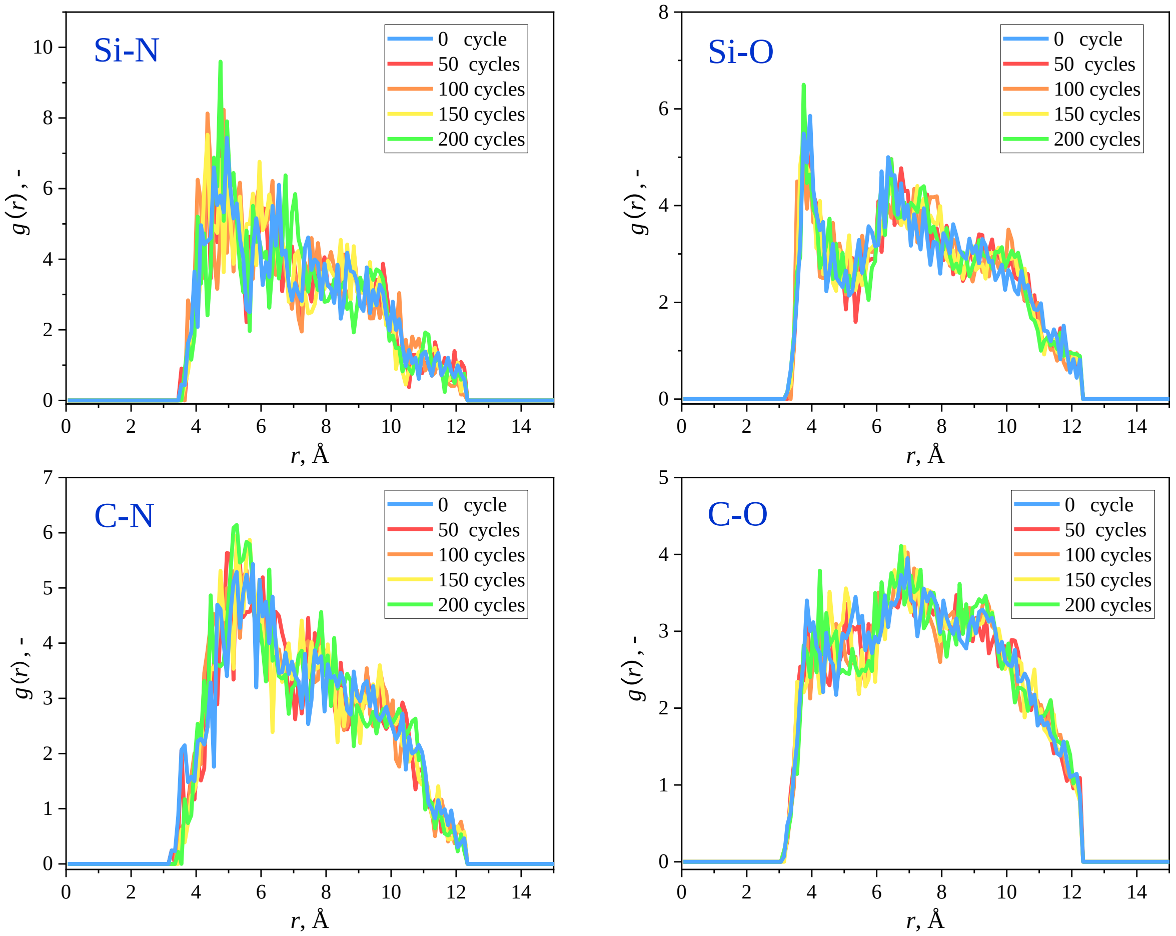

Figure 5.12: Radial distribution functions of Si-N and Si-O pairs in the Si-terminated domain and C-N and C-O pairs in the C-terminated domain.

It is seen from Figure 5.12 that the minimum distance of Si-N pairs at the initial state is 3.55 Å. After 50, 100, 150 and 200 cycles, the distance of Si-N pairs does not get shortened. For the possible products, i.e. Si_3N_4, the length of the Si-N bond is 1.75 Å [138]. It indicates that the Si and N species are not bonded. The minimum distance of Si-O pairs is 3.25 Å. The bond length of Si-O in SiO_2, the possible product, is 1.61 Å [139], suggesting that the Si and O species are also not bonded. In the C-terminated domain, the minimum distance of C-N and C-O pairs does not change after melting/solidification cycles. All the RDF results indicate that there are no new bonds formed between SiC and solar salt.

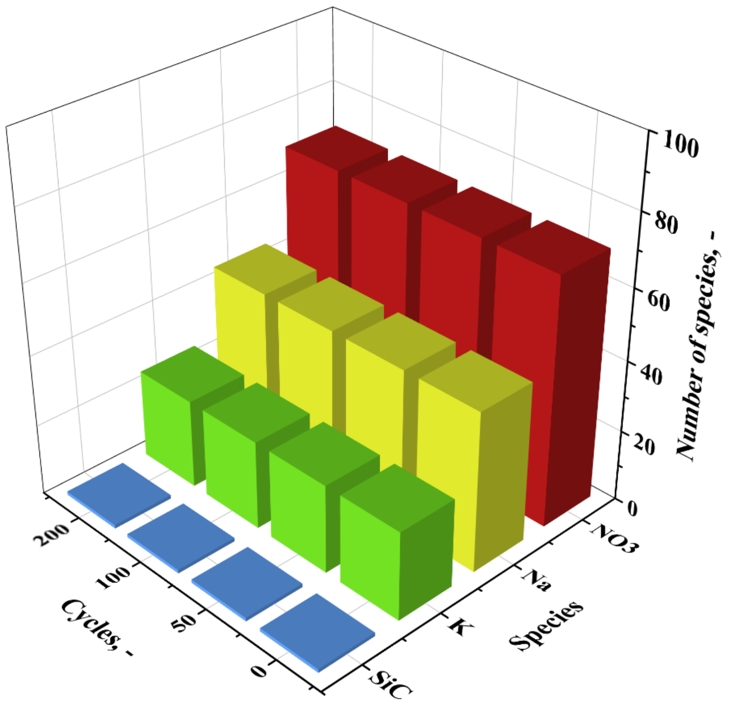

Figure 5.13: The number of various species under different melting/solidification cycles.

The possible chemical reaction was also monitored by detecting the number of chemical species. It is seen from Figure 5.13 that the number of SiC is constant 1. This is because SiC is a covalent compound [136]: one Si atom bonds with the neighbouring four C atoms; and each C atom also bonds with the neighbouring four Si atoms, resulting in a covalent network. So, they are identified as one molecule (Si192C192). During the simulation, the number of various species does not change, indicating there is no chemical reaction occurring between SiC and salt.

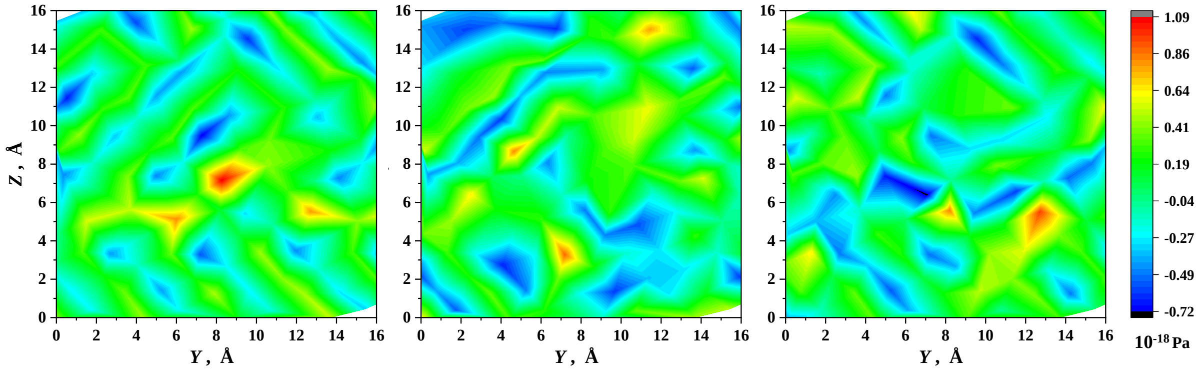

Figure 5.14: Distribution of the shear stress at the SiC surface during the cooling process. Figures from left to right denote the condition at 300 °C, 220 °C and 150 °C respectively.

The thermal stress induced by melting/solidification cycles would accelerate the corrosion [140]. Therefore, the effect of thermal stress on corrosion behaviours is analysed. Figure 5.14 shows the shear stress field at the SiC surface during the cooling process. It is seen that the stress field does not change significantly when the temperature decreases from 300 °C to 220 °C and finally to 150 °C. It may be attributed to the excellent thermal conduction of SiC. Heat can be transferred efficiently from the surface to the internal and the temperature difference between the surface and the internal is small, which would not generate a large stress gradient. Moreover, the coefficient of thermal expansion of SiC is only 3.69×10^{-6} /°C (150 °C) [141], which further weakens the influence of thermal stress. A snapshot of SiC after 200 cycles is presented in Figure 5.15. Although some atoms slightly deviate from the initial lattice point, there are no dislocations and defects, which indicates the stable structure of SiC.

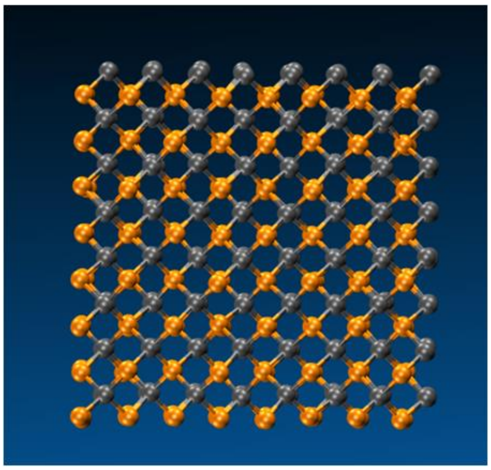

Figure 5.15: A snapshot of SiC after 200 cycles. Orange and grey spheres denote Si and C atoms respectively.

5.5 Summary

In this chapter, the compatibility between ceramic and salt is analysed. 50, 100 and 200 melting/solidification cycles were conducted to test the corrosion resistance of the prepared ceramic in solar salt. Various characterising technologies including scanning electron microscope (SEM), energy-dispersive spectroscopy (EDS), X-ray diffraction (XRD) and Raman were used to analyse the corrosion behaviours. The corrosion experiments of Cu and

Al were also conducted to make a comparison. Results indicate that the prepared ceramic has excellent corrosion-resistant performance.

In addition, a reactive molecular dynamics simulation was performed to provide microscopic insights into corrosion behaviours of ceramic, including the possible physical dissolution, chemical reaction and thermal stress failure. The results obtained from the molecular dynamics simulation are consistent with the corrosion behaviours of ceramic in solar salt.

Chapter 6 - Heat transfer characteristics of porous CPCM

6.1 Introduction

The above chapters introduce the preparation of salt/ceramic foam porous CPCMs and the compatibility. In this chapter, the heat transfer characteristics of porous CPCMs are studied. A visualised experimental setup is built and a numerical model is developed. The melting front is captured, and the temperature response is recorded. Effects of pore configurations, namely pore density and porosity on the melting performance are discussed. Moreover, the energy and exergy analysis is carried out to comprehensively evaluate the salt/ceramic foam porous CPCM.

6.2 Experiments

6.2.1 Materials and experimental setup

Three CPCMs with the pore density of 10 PPI (Pores Per Inch), 15 PPI and 20 PPI were used in the experiment. CPCM is in a quartz cavity and its dimension is 50 mm × 50 mm × 50 mm. The inner dimension of the quartz cavity is 50 mm (length) × 50 mm (width) × 55 mm (height) and the wall thickness is 2 mm. A gap of 5 mm was left between the top surface of CPCM and the cavity to allow the thermal expansion of CPCM.

The melting performance was investigated using the experimental setup shown in Figure 6.1(a). The setup comprises four parts: the test section, heating system, data collection system and visualization module. The whole test section was covered by thermal insulation materials to reduce heat loss to the environment. An aluminium plate was used to heat the test section and controlled by a temperature controller (AI-516P, Yudian Technology Co., Ltd). Three K-type thermocouples (WRNK-191, Jiayi Electric Co., Ltd) with a data collection system (KSA12A0R, Keshun Instrument Co., Ltd) were employed to record the local temperature. An infrared camera (HM-TPH16-6VF/W, Hikvision Technology Co., Ltd) and a digital camera were utilised to capture the temperature field and solid-liquid phase interface.

Three small holes were drilled in the centre of CPCM. The depth is 25 mm and the distance from the left wall of the cavity is 5 mm (point P1), 25 mm (point P2) and 45 mm (point P3) respectively. Thermocouples were inserted into the holes to measure the local temperature at P1, P2 and P3. The thermocouples were calibrated against a standard thermometer. The distribution of thermocouples is shown in Figure 6.1(b).

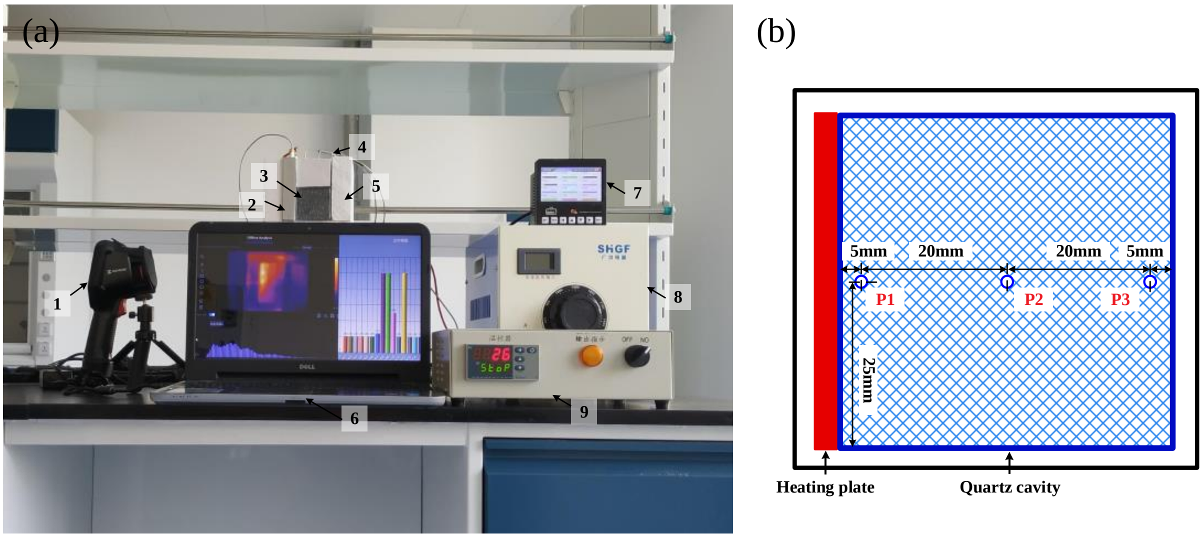

Figure 6.1: (a) Picture of the experimental setup for the melting performance test (1 – infrared camera, 2 – aluminium heating plate, 3 – quartz cavity with CPCM, 4 – K-type thermocouple, 5 – insulation, 6 – computer, 7 – data collection system, 8 – variable transformer, 9 – temperature controller). (b) Schematic of the distribution of thermocouples.

The infrared camera was used to capture the temperature field of the front surface of the quartz cavity. The spectral range of the infrared camera is 8 ~ 14 μm while the field of view is 25×19°. The optical resolution is 1600×1200 pixels and the noise equivalent temperature difference is 0.05 K. The infrared camera was calibrated using a pre-calibrated thermocouple. During the calibration process, the temperature ranged from 25 °C - 300 °C, which covered the temperature range in the actual experiment. By comparing the infrared-based temperature and the thermocouple-based temperature, the surface emissivity of the quartz cavity was identified to be 0.956.

6.2.2 Experimental procedure

During the experiment, the quartz cavity was heated by the left aluminium plate which was kept at 300 °C. The accuracy of the temperature controller is ±0.25%. The digital camera was used to capture the solid-liquid phase interface. The front insulation material was removed every 10 minutes to obtain the phase images. Thermocouples were employed to measure the local temperature at P1, P2 and P3. The uncertainties of all parameters are summarised in Table 6.1.

Table 6.1: Summary of the uncertainty.

Parameters	Uncertainty
Size of PCM, mm	1
Position of three points, mm	1
Temperature controlled by temperature controller, %	0.25
Temperature measured by thermocouples, %	0.3
Temperature measured by infrared camera, °C	2
Porosity of the skeleton, %	0.6
Pore size of the skeleton, PPI	0.5

6.3 Numerical simulation

A representative elementary volume (REV)-scale simulation was performed to help understand the melting process. The REV-scale simulation treats the porous CPCM as a uniformly mixed medium and does not require an accurate description of the porous skeleton. In other words, it ignores the complex geometry of the porous skeleton. This method uses some statistical parameters, such as porosity, permeability and effective thermal conductivity, to characterize the porous structure. The disadvantage is that it cannot reveal the flow and heat transfer characteristics in pores. But due to the simple input and low computational cost, it is a powerful tool for simulating large-scale systems [75]. The modelling process will be introduced in the following subsections.

6.3.1 Physical and mathematical model

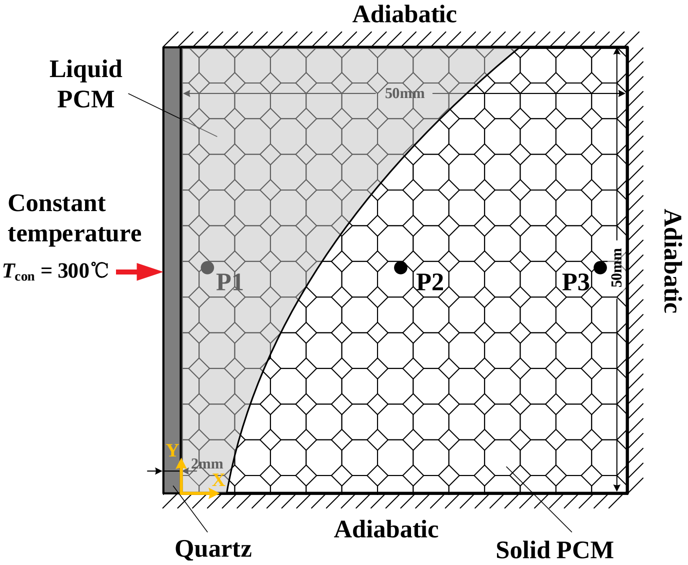

Figure 6.2: Physical model used in the numerical simulation.

During the experiment, it is observed that the solid-liquid interface is almost the same in the thickness direction. Moreover, the wall thickness of the quartz cavity is much smaller than the CPCM dimension. Thus, a two-dimensional numerical model is established. The physical model is shown in Figure 6.2. The dimensions of the quartz plate and the CPCM domain are 50 mm × 2 mm and 50 mm × 50 mm respectively. The temperature of the left side of the quartz plate is set as 300 °C. The top and bottom sides of the quartz plate and the top, bottom and right sides of the CPCM domain are set as adiabatic.

The following assumptions are made in the simulation: (1) the ceramic foam and PCM are homogenous and isotropic; (2) the flow of liquid PCM is laminar and incompressible; (3) the liquid PCM is subjected to the Boussinesq approximation; (4) the local thermal equilibrium exists between PCM and ceramic foam; (5) the volume difference of PCM before/after melting is neglected and (6) thermo-physical properties are temperature-independent.

The governing equations are summarised as follows:

Continuity equation [61]:

$$\nabla \cdot \vec{U} = 0 \tag{6-1}$$

Momentum equations [80]:

$$\frac{\rho_{\mathrm{PCM}}}{\varepsilon}\frac{\partial u}{\partial t}+\frac{\rho_{\mathrm{PCM}}}{\varepsilon^2}\left(\vec{U}\cdot\nabla u\right)=-\frac{\partial p}{\partial x}-\frac{\mu_{\mathrm{PCM}}}{K}u-\frac{\rho_{\mathrm{PCM}}F_1}{\sqrt{K}}|u|u+\frac{\mu_{\mathrm{PCM}}}{\varepsilon}\nabla^2 u-\frac{(1-\varphi)^2}{(\varphi^3+\omega)}A_{\mathrm{mushy}}u \quad (6\text{-}2)$$

$$\frac{\rho_{\mathrm{PCM}}}{\varepsilon}\frac{\partial v}{\partial t}+\frac{\rho_{\mathrm{PCM}}}{\varepsilon^2}\left(\vec{U}\cdot\nabla v\right)=-\frac{\partial p}{\partial y}-\frac{\mu_{\mathrm{PCM}}}{K}v-\frac{\rho_{\mathrm{PCM}}F_1}{\sqrt{K}}|v|v+\frac{\mu_{\mathrm{PCM}}}{\varepsilon}\nabla^2 v+\rho_{\mathrm{PCM}}\,g\,\beta(T-T_{\mathrm{m1}})$$

$$-\frac{(1-\varphi)^2}{(\varphi^3+\omega)}A_{\mathrm{mushy}}v \quad (6\text{-}3)$$

where ρ_{PCM} is the PCM density; u and v are the velocities in x and y directions, respectively; p is the pressure; μ_{PCM} is the PCM viscosity; g is the gravitational acceleration; β is PCM thermal expansion coefficient; T is the temperature; T_{ml} is the lower limit of PCM melting point; φ is the melting fraction in each cell; ω is a small number (0.001) to prevent being divided by zero; A_{mushy} is the mushy zone constant (10^5) [21]. ε is the porosity; K is the permeability; F_{l} is the inertia coefficient. The second term on the right side of momentum equations denotes the Darcy effect; the third term explains the Forchheimer-extended Darcy effect [11]. $\rho_{\mathrm{PCM}}\,g\,\beta(T-T_{\mathrm{m1}})$ represents the Boussinesq approximation. The last term in momentum equations is the damping term [21]. The melting fraction φ quantifies the percentage of liquid PCM in the mushy zone and is evaluated by [51]:

$$\varphi=\frac{T-T_{\mathrm{m1}}}{T_{\mathrm{mu}}-T_{\mathrm{ml}}}=\begin{cases}0 & \text{for } T<T_{\mathrm{m1}}\\ 0-1 & \text{for } T_{\mathrm{m1}}\le T\le T_{\mathrm{mu}}\\ 1 & \text{for } T>T_{\mathrm{mu}}\end{cases} \quad (6\text{-}4)$$

where T_{mu} is the upper limit of PCM melting point.

Local thermal equilibrium is adopted because the temperature difference between the ceramic foam and salt is very small (< 0.52 °C) according to a previous study [142]. Energy equation is given by [90]:

$$\left[(1-\varepsilon)\rho_{\mathrm{ps}}c_{\mathrm{p,\,ps}}+\varepsilon\,\rho_{\mathrm{PCM}}\,c_{\mathrm{p,\,PCM}}\right]\frac{\partial T}{\partial t}+\rho_{\mathrm{PCM}}\,c_{\mathrm{p,\,PCM}}\left(\vec{U}\cdot\nabla T\right)=k_{\mathrm{ef}}\nabla^2 T-\varepsilon\rho_{\mathrm{PCM}}L\frac{df_{\mathrm{l}}}{dt} \quad (6\text{-}5)$$

where $c_{p,\,\mathrm{PCM}}$ and $c_{p,\,\mathrm{ps}}$ are the specific heat of PCM and porous skeleton respectively; k_{PCM} is the thermal conductivity of PCM; L is the latent heat; ρ_{ps} is the density of porous skeleton; k_{ef} is the effective thermal conductivity, which will be introduced in the next subsection.

6.3.2 Thermo-physical properties

The melting point and latent heat of solar salt were measured using the same methodology in Chapter 3. The specific heat was measured using Discovery DSC25 (TA Instruments Co., Ltd). The accuracy of the temperature control of the equipment is ± 0.01°C. The accuracy of the calorimeter (indium, the standard metal) is ± 0.1%. The baseline reproducibility is < 40 Mw. Nitrogen was employed as the cooling gas and the flow rate was 50 ml/min. Thermal conductivity was measured using Hot Disk 2500S (Hot Disk AB Co., Ltd). The accuracy is ± 3%. Other parameters are adopted from Ref. [26]. The thermo-physical properties of solar salt, ceramic and quartz are listed in Table 6.1.

The effective thermal conductivity is calculated using Yao et at.'s model [143]:

$$k_{\mathrm{ef,\,ps}} = \frac{1-\varepsilon}{3} k_{\mathrm{ps}} \tag{6-6}$$

$$k_{\mathrm{ef,\,PCM}} = \frac{2+\varepsilon}{3} k_{\mathrm{PCM}} \tag{6-7}$$

$$k_{\mathrm{ef}} = k_{\mathrm{ef,\,ps}} + k_{\mathrm{ef,\,PCM}} \tag{6-8}$$

where k_{ps} and k_{PCM} are the thermal conductivity of ceramic and salt, respectively.

The above correlations were developed based on the direct simulation of thermal conduction over a wide range of thermal conductivity ratios (0.001-1000) between the porous skeleton and filling medium. They have been compared with experimental data and show high accuracy [143]. Moreover, the correlations have a simple and elegant form of expression and can be very easily used in modelling. Therefore, they were adopted in the current simulation.

Table 6.2: Thermo-physical properties of solar salt, ceramic and quartz.

Material	Parameter	Value

Solar salt	Density, kg/m^3	1980
	Latent heat, J/kg	140,000
	Melting point, °C	222.9 – 246.0
	Specific heat, J/(kg·K)	1575
	Thermal conductivity (solid/liquid), W/(m·K)	0.59/0.48
	Viscosity, mPa·s	4.61
	Thermal expansion coefficient, K^{-1}	5.47×10^{-5}
Ceramic	Thermal conductivity, W/(m·K)	20.7
	Specific heat, J/(kg·K)	800
	Density, kg/m^3	2327
Quartz	Thermal conductivity, W/(m·K)	1.65
	Specific heat, J/(kg·K)	892.5
	Density, kg/m^3	2200

The permeability K and inertia coefficient F_l are calculated by [21]:

$$K=\frac{\varepsilon^2\left(d_\mathrm{fp}\sqrt{\kappa_\mathrm{tor}/3\varepsilon}\right)^2}{36(\kappa_\mathrm{tor}-1)\kappa_\mathrm{tor}} \tag{6-9}$$

$$F_\mathrm{l}=0.00212(1-\varepsilon)^{-0.132}\left(d_\mathrm{fs}/d_\mathrm{fp}\right)^{-1.63} \tag{6-10}$$

$$d_\mathrm{fp}=\frac{25.4\times10^{-3}}{\mathrm{PPI}} \tag{6-11}$$

$$d_\mathrm{fs}=1.18\sqrt{\frac{1-\varepsilon}{3\pi}}\left[\frac{1}{1-e^{(\varepsilon-1)/0.04}}\right]d_\mathrm{fp} \tag{6-12}$$

$$\frac{1}{\kappa_\mathrm{tor}}=\frac{3}{4\varepsilon}+\frac{\sqrt{9-8\varepsilon}}{2\varepsilon}\cos\left\{\frac{4\pi}{3}+\frac{1}{3}\cos^{-1}\left[\frac{8\varepsilon^2-36\varepsilon+27}{(9-8\varepsilon)^{1.5}}\right]\right\} \tag{6-13}$$

These correlations are suitable for the solid-liquid phase change of PCM in porous foam [21].

6.3.3 Initial and boundary conditions

For the wholee computational domain, the initial conditions are:

$$u=v=0,\ \ T=T_i \tag{6-14}$$

where T_i is the initial temperature (27 °C).

The boundary condition of the left wall of the quartz cavity is:

$$T_{\mathrm{quartz}}\Big|_{x=-2} = T_{\mathrm{con}} \tag{6-15}$$

where T_{con} is the constant heating temperature (300 °C).

The boundary conditions of the adiabatic walls:

$$\left.\frac{\partial T_{\mathrm{PCM}}}{\partial x}\right|_{x=50} = 0 \tag{6-16}$$

$$\left.\frac{\partial T_{\mathrm{PCM}}}{\partial y}\right|_{y=0} = \left.\frac{\partial T_{\mathrm{quartz}}}{\partial y}\right|_{y=0} = \left.\frac{\partial T_{\mathrm{PCM}}}{\partial y}\right|_{y=50} = \left.\frac{\partial T_{\mathrm{quartz}}}{\partial y}\right|_{y=50} = 0 \tag{6-17}$$

At the interface of the quartz plate and PCM domain, the continuity conditions of temperature and heat flux are:

$$T_{\mathrm{PCM}}\,|_{x=0} = T_{\mathrm{quartz}}\,\Big|_{x=0} \tag{6-18}$$

$$(-k_{\mathrm{PCM}}\,\nabla T_{\mathrm{PCM}})\cdot\boldsymbol{n}|_{x=0} = (-k_{\mathrm{quartz}}\,\nabla T_{\mathrm{quartz}})\cdot\boldsymbol{n}|_{x=0} \tag{6-19}$$

6.3.4 Numerical procedure

The above numerical model was solved using ANSYS Fluent 18.0 package. The governing equations were discretized using the finite volume method. The SIMPLE scheme was used to couple pressure and velocity. The second-order upwind method was implemented to discretise pressure, momentum and energy terms. The under-relaxation factors for pressure, density, body forces, momentum, liquid fraction update and energy were set as 0.3, 1, 1, 0.7, 0.9 and 1 respectively. The convergence criteria for conservation equations of mass, momentum and energy were 10^{-4}, 10^{-4} and 10^{-6} respectively.

To balance the computational accuracy and cost, different mesh sets and time steps were tested. First, under the fixed time step of 0.5 s, three mesh sets (100 × 100, 200 × 200 and 400 × 400 cells) were tested; it is found that the maximum deviation in the melting fraction is less than 0.02. Then, under the fixed mesh of 200 × 200 cells, three time steps (0.1 s, 0.5 s and 1.0

s) were tested and the maximum deviation is less than 0.01. The mesh set of 200 × 200 cells and the time step of 0.5 s were used as the final settings.

6.4 Results and discussions

6.4.1 Melting front

The evolution of the melting front of pure salt and salt/ceramic foam CPCMs is presented in Figure 6.3. For the pure salt, the solid-liquid phase interface is curved even at the initial melting stage (40 min). This is different from the melting of some organic PCMs where the phase interface is almost parallel to the heating wall at the initial stage [55]. The reason may be that the viscosity of liquid salt is lower than that of organic PCM [55], which results in stronger natural convection. With the elapse of time, more PCM is melted and the effect of natural convection is greater. As a result, the solid-liquid phase interface becomes more curved.

For the salt/ceramic foam CPCMs, the phase interface is also curved in the initial stage. The viscosity of liquid salt is low and ceramic foam is open-cell, so natural convection in CPCMs is not greatly suppressed. Moreover, the addition of ceramic foam remarkably enhances heat conduction. As a result, the evolution of the solid-liquid interface is overall faster than that of pure salt.

The melting fraction was calculated based on the area occupied by the liquid PCM in the digital images [55]. The ImageJ software was used to deal with the images to identify the pixel-areas of PCMs. The results are plotted in Figure 6.4. It is seen that at the initial stage, the melting of CPCMs is not significantly faster than that of pure salt. It can be explained as follows: the effective thermal conductivity of CPCM is larger and the absorbed heat is transferred to the internal PCM, which improves the overall temperature distribution; for pure salt, the absorbed heat accumulates near the wall, leads to the melting of salt.

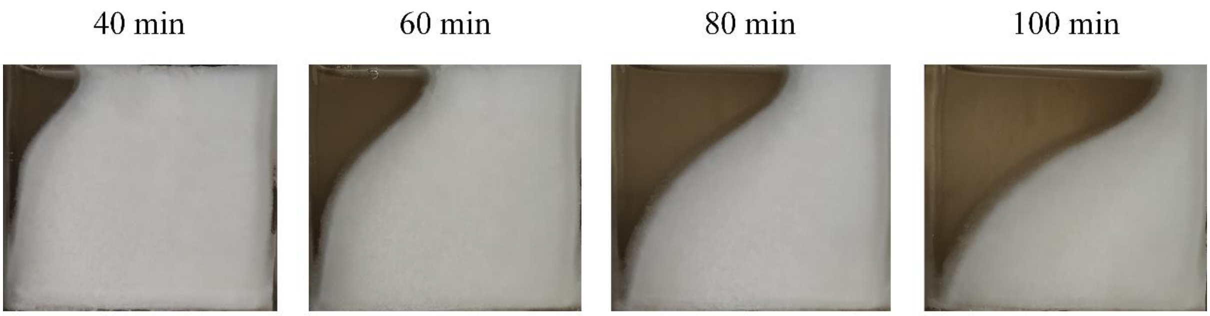

(a) Pure molten salt

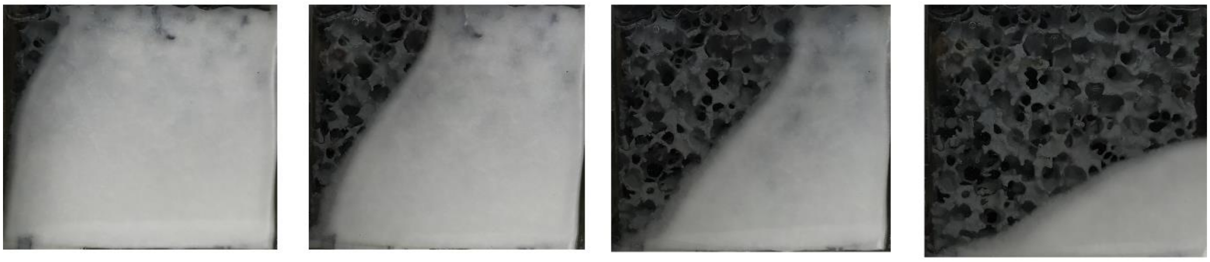

(b) Molten salt/ceramic foam, 10 PPI

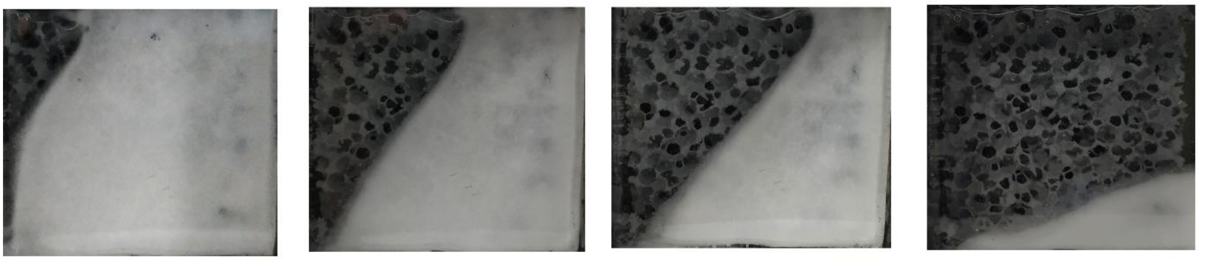

(c) Molten salt/ceramic foam, 15 PPI

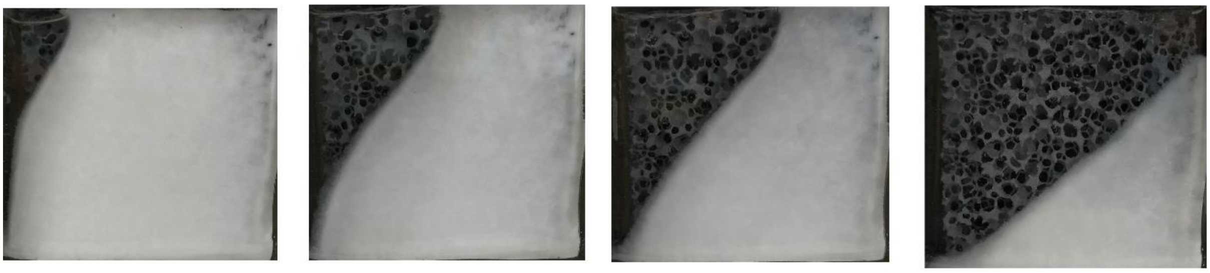

(d) Molten salt/ceramic foam, 20 PPI

Figure 6.3: Melting front of pure salt and salt/ceramic foam CPCMs.

With the time elapsed, the melting of CPCMs becomes obviously faster than that of pure salt. One of the reasons is the improved temperature field at the initial stage (more details are discussed in the following subsection). The complete melting time of pure salt is 205 min (error: ± 5 min). The melting time of salt/ceramic foam CPCMs with 10 PPI, 15 PPI and 20 PPI is 115 min, 115 min and 125 min respectively. The melting rate is calculated by:

$$v_m = \frac{V_{PCM}}{t_m} \tag{6-20}$$

where V_{PCM} is the volume of salt; t_m is the complete melting time.

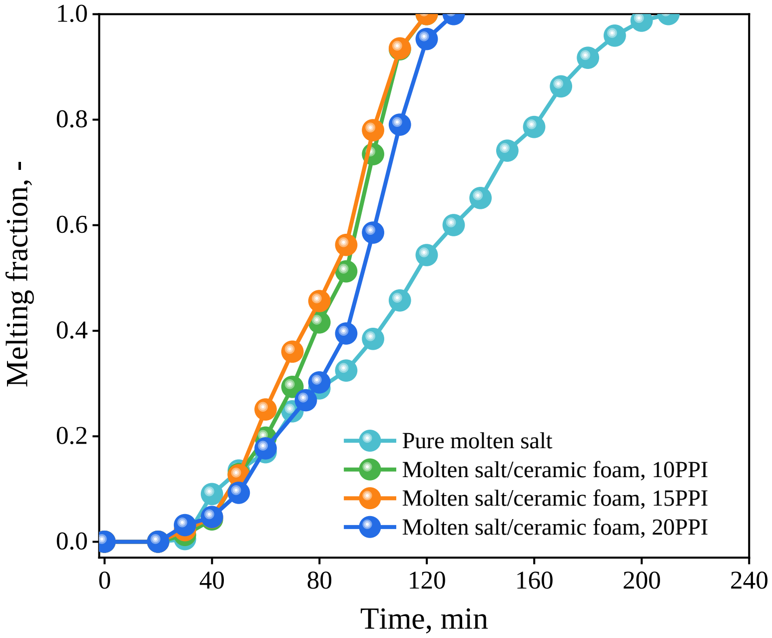

Figure 6.4: Variation of melting fraction of pure salt and salt/ceramic foam CPCMs.

Considering the porosity (0.85) and the impregnation ratio (> 95%), the melting rate of 10 PPI, 15 PPI and 20 PPI CPCMs is increased by 51.5%, 51.5% and 39.4% respectively. And the ceramic foam with a large pore size is more beneficial to enhance the melting performance. It should be pointed out that the melting fraction is calculated based on the phase images observed through the front window. In the current study, the internal solid-liquid interface is assumed to be similar to the front one as the ceramic foam is overall uniform. And when the front salt was melted completely, the thermal insulation was removed and it was observed that all the salt was melted completely.

6.4.2 Temperature response

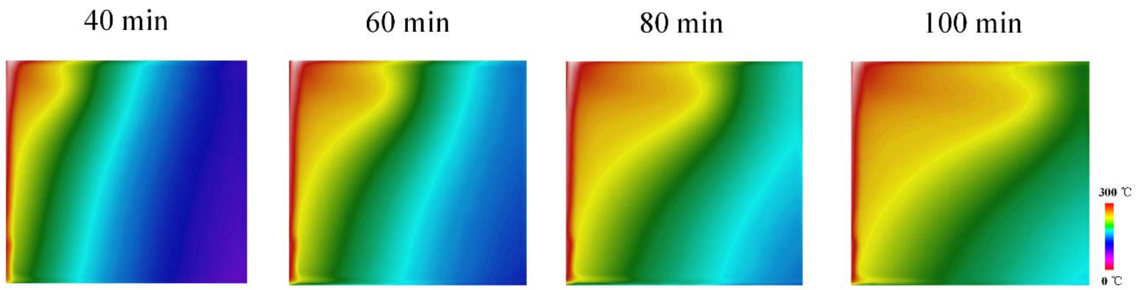

(a) Pure molten salt

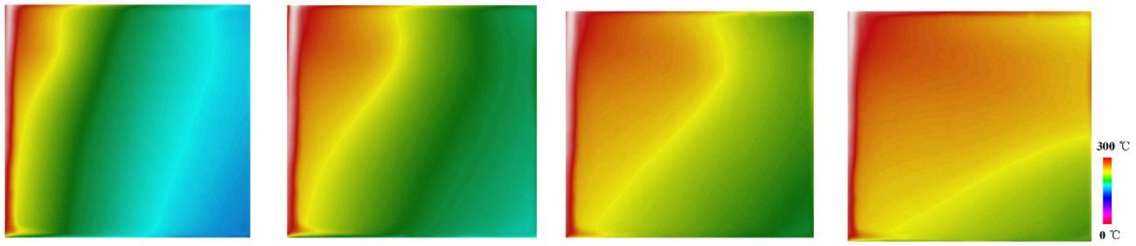

(b) Molten salt/ceramic foam, 10 PPI

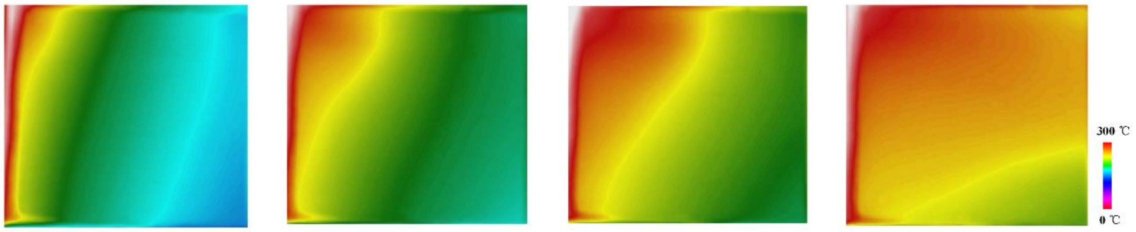

(c) Molten salt/ceramic foam, 15 PPI

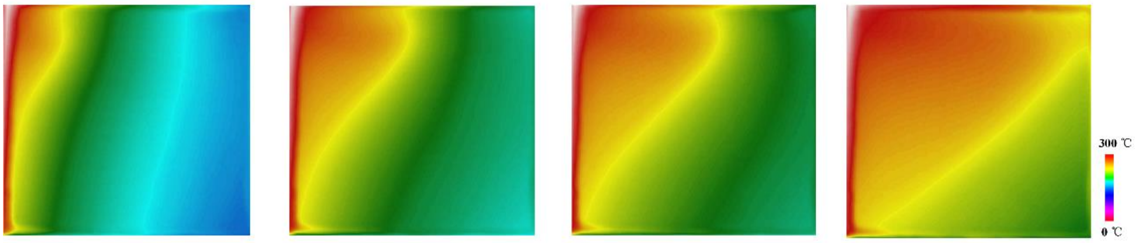

(d) Molten salt/ceramic foam, 20 PPI

Figure 6.5: Temperature fields of the front surface of the quartz cavity whith (a) pure salt, (b) 10 PPI ceramic foam/salt, (c) 15 PPI ceramic foam/salt, (d) 20 PPI ceramic foam/salt.

The temperature field of the front surface of the cavity was captured by the infrared camera and the results are shown in Figure 6.5. Although the melting front of four cases at 40 min is almost identical (as shown in Figure 6.3), the temperature fields of CPCMs are significantly improved, especially in the region far away from the heating wall. The improved temperature field at the initial stage helps accelerate the melting at the later stages.

The temperature in the top left corner is higher, which should be attributed to natural convection. With the elapse of time, more PCM is melted and the temperature fields of all cases are enhanced. It is noted that the overall temperature of CPCMs is always larger than that of pure salt. The reason lies in that the effective thermal conductivity of CPCM is larger (CPCM: 1.60 W/(m·K), pure salt: 0.59 W/(m·K)), so heat can be efficiently transferred from the boundary to the inside.

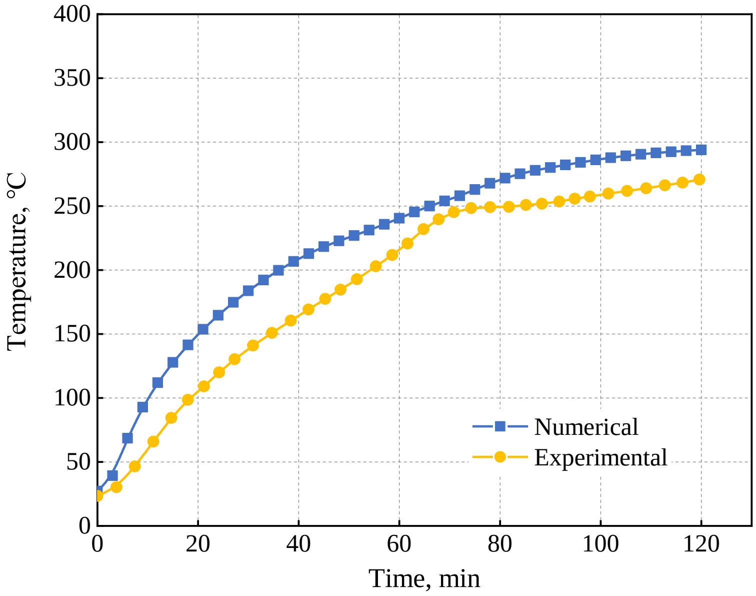

Figure 6.6: Comparison of measured and simulated temperature at P2 in 15 PPI salt/ceramic foam CPCM.

Figure 6.6 shows the comparison of the measured and simulated temperature at P2 (15 PPI salt/ceramic foam CPCM). It is seen that the numerical results are larger than the experimental data. The possible reasons are as follows: (1) the aluminium heater and the quartz cavity cannot be fit completely due to the surface roughness, which causes the contact thermal resistance and decreases the heating efficiency; while in the simulation, the left side of the quartz cavity is constantly at 300 °C; (2) the thermal insulation material with the thickness of 5.0 cm is used to wrap the quartz cavity in the experiment, however, there is still a little heat loss to the environment; (3) during the experiment, the front cover is removed every 10 min to take pictures, and the temperature difference between the cavity and the environment can exceed 200 °C, which leads to great heat loss; (4) the temperature controller is set as 300 °C, however, it takes some time for the aluminium heater to reach 300 °C, while in the simulation, the left side of the quartz cavity is at 300 °C initially. Thus, it is reasonable that the numerical results is larger than the experimental ones. At the final stage of melting, the difference between the measured and simulated temperature is less than 10%. The developed numerical model can still be used to analyse the energy storage performance.

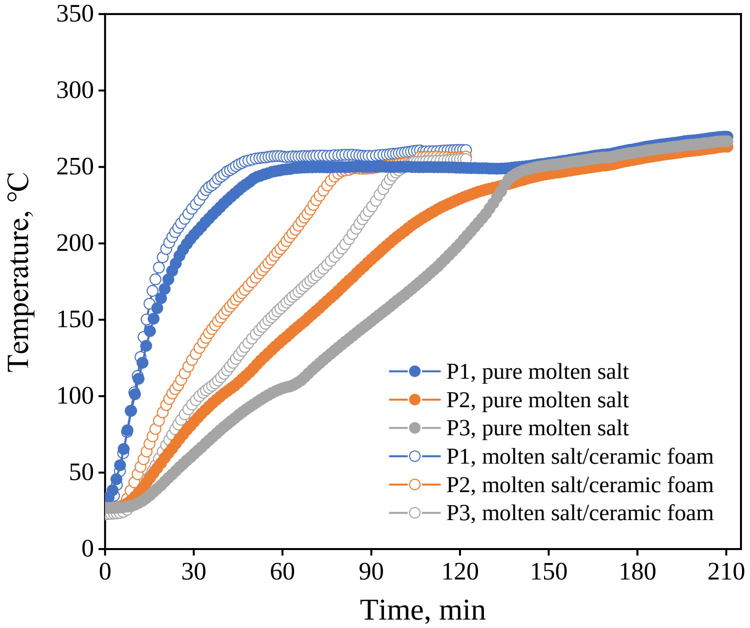

Figure 6.7: Measured temperature in pure salt and 20 PPI salt/ceramic foam CPCM.

Figure 6.7 shows the measured temperature at P1, P2 and P3. It is found that the temperature in CPCM rises faster than that in pure PCM. It should be attributed to the thermal conductivity: the thermal conductivity of pure salt is 0.59 W/(m·K); the effective thermal conductivity of salt/ceramic foam CPCM is 1.60 W/(m·K). The increased thermal conductivity helps transfer heat from the heating wall to PCM. CPCM can absorb more heat and its temperature rises faster. It is noted that the enhancement effect of ceramic foam on temperature is more significant at points that are far away from the heating wall, namely P2 and P3. This phenomenon is consistent with the observation in Figure 6.5. The reason lies in that the distance from P2 and P3 to the heating wall is long and the enhancement effect of ceramic foam can be more exerted.

The effect of foam porosity on melting performance is studied using numerical simulation. The melting fraction of pure salt and salt/ceramic foam CPCMs (porosity: 0.80, 0.85 and 0.90) is shown in Figure 6.8. It is noted that the simulated results have a little deviation from the experimental results. The reasons have been analysed above. And the four cases have the same simulation conditions, so they can be compared together. Compared to pure salt, the melting rate of CPCMs with 0.90, 0.85 and 0.80 porosities is increased by 6.9%, 31.7% and 58.3%. The increment is 51.4% (59.3% - 6.9%). As discussed above, when the pore size varies from 20 PPI to 10 PPI, the increase in the melting rate is from 39.4% to 51.5% and the increment is 12.1% (51.5% - 39.4%). Therefore, the foam porosity has a more significant effect on the melting performance than pore size.

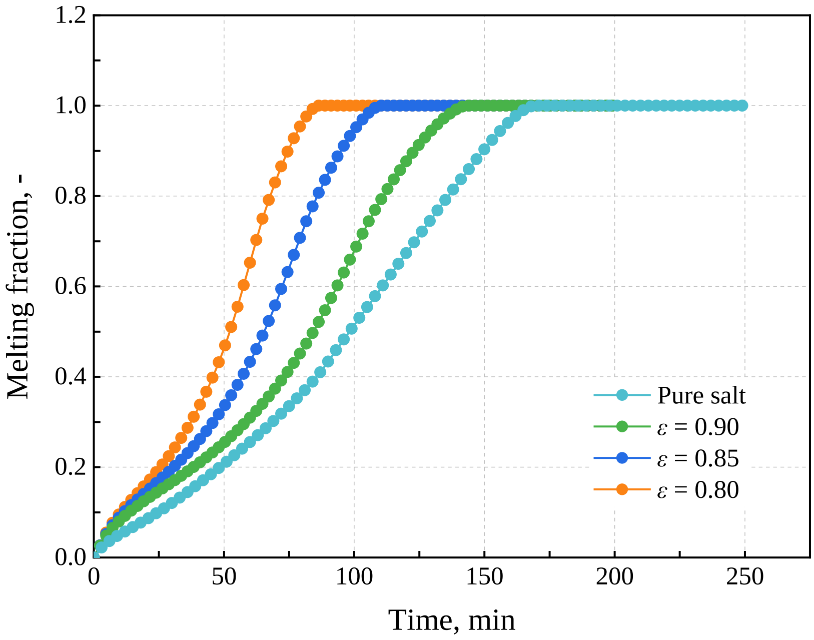

Figure 6.8: Simulated melting fraction of pure salt and salt/ceramic foam CPCMs (15 PPI) with different porosities.

6.4.3 Energy storage performance

The energy storage performance is analysed based on the above numerical simulation. Figure 6.9 shows the stored sensible heat and latent heat of pure salt and salt/ceramic foam CPCMs with different porosities. It is found that for all cases, the stored sensible heat is much larger than the latent heat. This is because the initial temperature is 27 °C and the final temperature is about 280 °C; the temperature increase is large, over 250 °C, resulting in the large sensible heat.

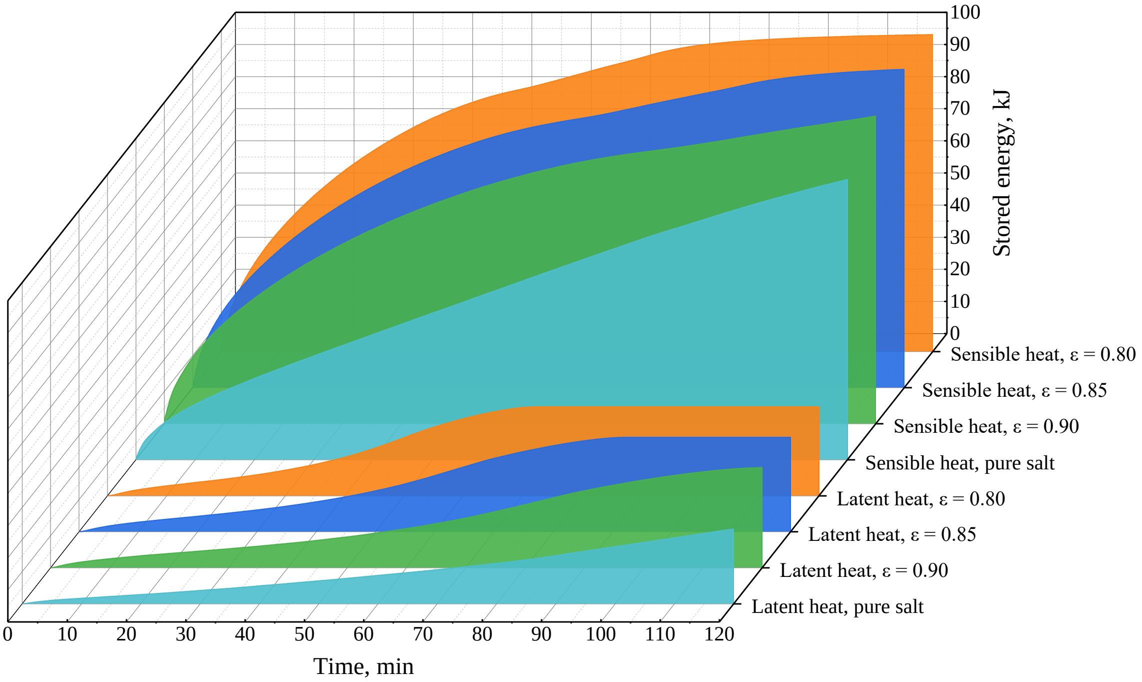

Figure 6.9: Stored sensible and latent heat of pure salt and salt/ceramic foam CPCMs.

It is noted that the stored sensible heat of CPCMs increases faster than that of pure salt. This is because that the temperature of CPCMs rises faster. And the increase of latent heat of CPCMs is also faster, which can be explained by Figure 6.8: the melting fraction of CPCMs is larger than that of pure salt at a given moment.

The total stored energy, complete melting time and energy storage rate of four cases are presented in Figure 6.10. The energy storage rate is calculated by:

$$w = \frac{E}{t_{\mathrm{m}}} \tag{6-21}$$

where E is the total stored energy.

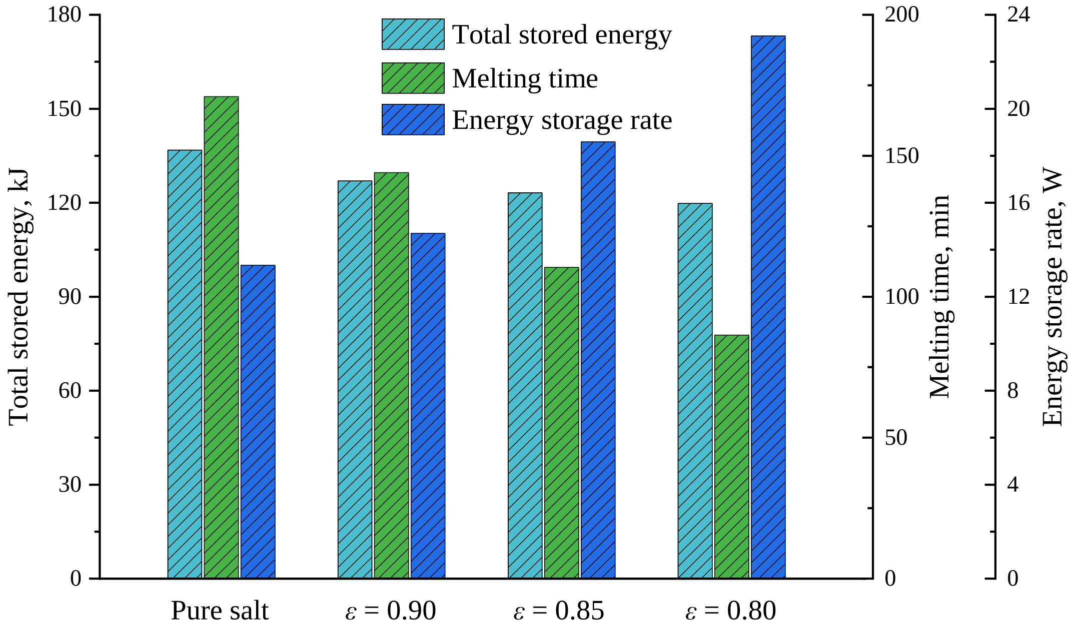

Figure 6.10: Total stored energy, complete melting time and energy storage rate of pure salt and salt/ceramic foam CPCMs.

Although the addition of ceramic foam reduces the fraction of salt, the total stored energy of CPCMs is only slightly decreased compared to pure salt. It may be explained as follows: the sensible heat dominates the total stored energy, as Figure 6.9 shows; although the fraction of salt is decreased, the sensible heat stored by ceramic foam compensates for some of the lost latent heat stored by salt. Ceramic foam shortens the melting time. As a result, the energy storage rate is increased. The energy storage rate of CPCMs with 0.90, 0.85 and 0.80 porosities is improved by 10.2%, 39.5% and 73.2% respectively.

6.4.4 Exergy analysis

Exergy characterises the amount of effective thermal energy for a specific application. The input exergy is calculated by [144]:

$$Ex_{\text{in}} = \int_0^t \left[q_{\text{in}} \left(1 - \frac{T_0}{T_{\text{wall}}} \right) \right] dt \tag{6-22}$$

The output exergy is [144]:

$$Ex_{\mathrm{out}} = \int_0^t \left[\left(1 - \frac{T_0}{T_{\mathrm{PCM}}}\right) m_{\mathrm{PCM}} c_{\mathrm{PCM}} \frac{dT_{\mathrm{PCM}}}{dt} + \left(1 - \frac{T_0}{T_{\mathrm{m}}}\right) \rho_{\mathrm{PCM}} L \frac{df_1}{dt} + \left(1 - \frac{T_0}{T_{\mathrm{quartz}}}\right) m_{\mathrm{quartz}} c_{\mathrm{quartz}} \frac{dT_{\mathrm{quartz}}}{dt}\right] dt \tag{6-23}$$

where T_0 is the reference temperature, assumed to be 27 °C in the current study; T_{wall} is the temperature of the heating wall (300 °C); q_{in} is the input heat flux; T_{m} is the PCM melting temperature. During the calculation of output exergy, T_{m} should be a specific value, rather than a range. So it is assumed that T_{m} is the average value of the solidus temperature and the liquidus temperature of solar salt (234.5 °C) only for modelling purpose.

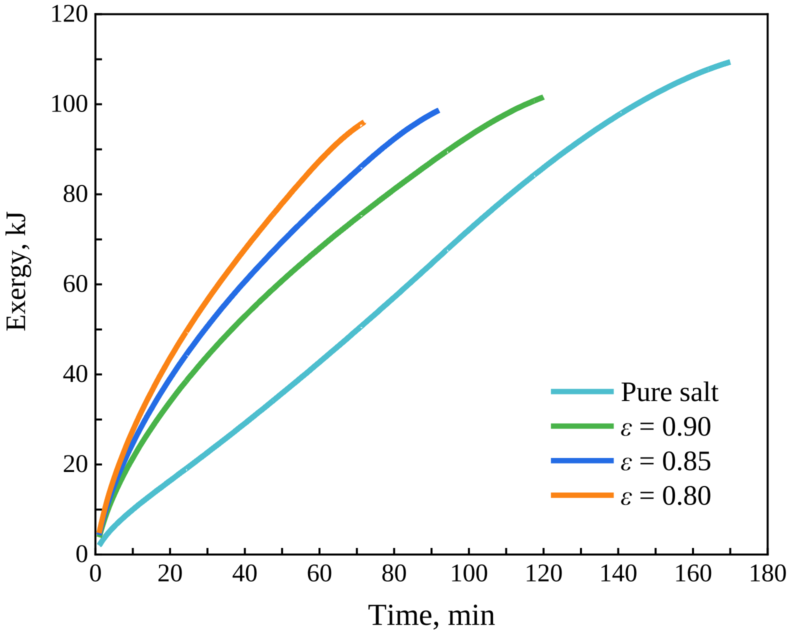

Figure 6.11: Variation of exergy of pure salt and salt/ceramic foam CPCMs with different porosities.

The variation of exergy of pure salt and salt/ceramic foam CPCMs is plotted in Figure 6.11. It is seen that the exergy of salt/ceramic foam CPCMs increases much faster than that of pure salt. And the lower the porosity, the faster the increase in exergy. The reason is that due to the enhancement of ceramic foam, the temperature of CPCMs increases faster and the melting fraction is larger, as indicated in Figure 6.7 and Figure 6.8.

The exergy efficiency is calculated by [144]:

$$\eta = \frac{Ex_{\mathrm{out}}}{Ex_{\mathrm{in}}} \tag{6-24}$$

The exergy efficiency of the four cases is shown in Figure 6.12. The exergy efficiency of pure salt is the lowest. It may be because the thermal conductivity of pure salt is lower than that of CPCMs; heat cannot be efficiently transferred from the heating wall to PCM and the overall temperature is low, as indicated in Figure 6.5. This reduces the quality of stored thermal energy and thus the exergy efficiency is low. The exergy efficiency of CPCMs is 54.5%, 55.9% and 57.2% higher than that of pure salt. It suggests that CPCMs increase the utilization efficiency of the heat source and can store more effective thermal energy.

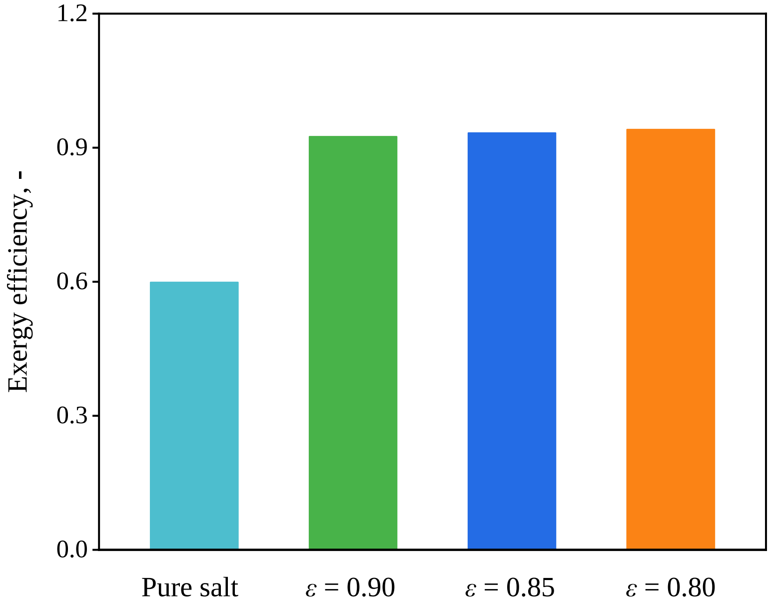

Figure 6.12: Exergy efficiency of pure salt and salt/ceramic foam CPCMs.

6.5 Summary

In this chapter, the heat transfer characteristics of salt/ceramic foam CPCMs with various pore configurations are studied experimentally and numerically. An energy and exergy analysis is carried out to evaluate CPCMs comprehensively. The following conclusions are drawn:

(1) The melting rate of CPCMs with pore density of 10 PPI, 15 PPI and 20 PPI is increased by 51.5%, 51.5% and 39.4% respectively. The porosity has a more significant effect on the melting performance than pore density. The total stored energy is slightly decreased as the sensible heat stored by ceramic foam compensates for some of the lost latent heat (conditions: initial temperature: 27 °C; heating temperature: 300 °C). The energy storage rate is improved

significantly. The average energy storage rate of CPCM with the porosity of 0.80 is increased by 73.2%.

(2) Compared to pure salt, the exergy of CPCMs rises much faster and the exergy efficiency of all CPCMs is increased by more than half.

Chapter 7 - Melting performance in a shell-and-tube unit

7.1 Introduction

The shell-and-tube heat storage unit is one of the most popular devices for industrial and commercial thermal energy storage applications [148]. In this unit, PCM occupies the circular space between the shell and tube while the heat transfer fluid (HTF) flows through the inner tube. In this chapter, the melting performance of ceramic foam/salt CPCM in a shell-and-tube unit is studied numerically. Multiple factors including filling height, porosity and outer diameter of ceramic foam are considered and compared to obtain the optimal configuration. This study evaluates the melting performance of salt/ceramic foam CPCM in the shell-and-tube heat storage unit comprehensively, providing energy storage information for practical applications.

7.2 Numerical model

7.2.1 Physical and mathematical model

The schematic of the shell-and-tube unit is shown in Figure 7.1(a). The thickness of the shell and tube is 3 mm and 2 mm respectively while the inner radius is 62 mm and 20 mm respectively. The energy storage material is filled in the annular space between the shell and tube, and HTF flows through the tube. The total length of the unit is 500 mm.

The configuration of the ceramic foam would have an influence on the thermal energy storage performance. In the current study, three factors are considered: the filling height, outer diameter and porosity of the ceramic foam. In terms of the first factor, the filling height of the ceramic foam, H, ranges from 0 d_{si} to 1 d_{si}, where d_{si} is the inner diameter of the shell (124.0 mm). The detailed filling height is listed in Table 7.1. For the second factor, the outer diameter of the ceramic foam, d_{cf}, ranges from 54.0 mm to 124.0 mm. In the first two factors, the porosity of the ceramic foam is 0.85 and the pore density is 10 PPI. In terms of the third factor, the outer diameter of the ceramic foam is fixed at 124.0 mm, i.e. fully filling in the annular space. The porosity varies from 0.70 to 0.95.

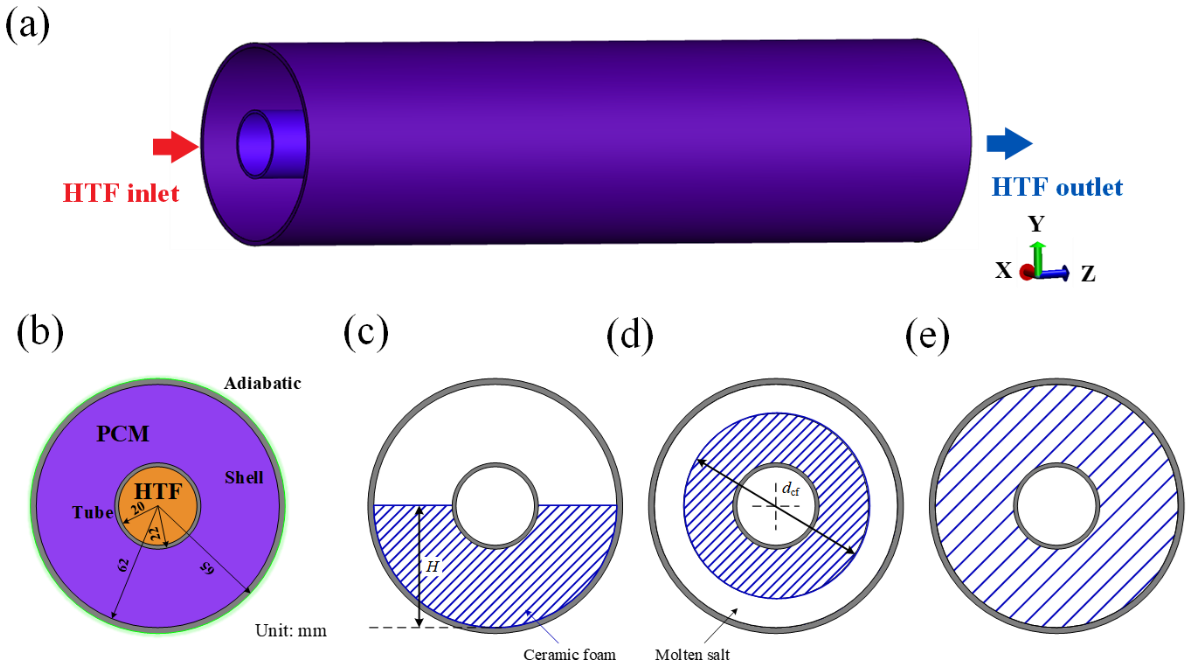

Figure 7.1: (a) Schematic of the shell-and-tube unit used in the numerical study; (b) the cross-section of the unit; (c) the unit with the varied filling height of the ceramic foam; (d) the unit with the varied outer diameter of the ceramic foam; (e) the unit with the varied porosity of the ceramic foam.

Table 7.1: Configurations of the ceramic foam in the shell-and-tube unit.

Factor 1	H, mm	Factor 2	d_{cf}, mm	Factor 3	ε, -
Filling height	0 (0 d_{si})	Outer diameter	54.0	Porosity	0.70
	12.4 (0.1 d_{si})		64.0		0.75
	24.8 (0.2 d_{si})		74.0		0.80
	37.2 (0.3 d_{si})		84.0		0.85
	49.6 (0.4 d_{si})		94.0		0.90
	62.0 (0.5 d_{si})		104.0		0.95
	74.4 (0.6 d_{si})		114.0		
	86.8 (0.7 d_{si})		124.0		
	99.2 (0.8 d_{si})				
	111.6 (0.9 d_{si})				
	124.0 (1.0 d_{si})				

For numerical modelling, the following assumptions were made: (1) the ceramic foam and PCM are homogenous and isotropic; (2) the flow of liquid PCM is laminar and incompressible; (3) the liquid PCM is subjected to the Boussinesq approximation; (4) the volume difference of PCM before/after melting is neglected and (5) thermo-physical properties except PCM density are temperature-independent.

The governing equations for PCM are summarised as follows:

Continuity equation [61]:

$$\nabla \cdot \vec{U} = 0 \tag{7-1}$$

Momentum equations [80]:

$$\frac{\rho_{\mathrm{PCM}}}{\varepsilon}\frac{\partial u}{\partial t}+\frac{\rho_{\mathrm{PCM}}}{\varepsilon^2}\left(\vec{U}\cdot\nabla u\right) = -\frac{\partial p}{\partial x}-\frac{\mu_{\mathrm{PCM}}}{K}u-\frac{\rho_{\mathrm{PCM}}F_1}{\sqrt{K}}|u|u+\frac{\mu_{\mathrm{PCM}}}{\varepsilon}\nabla^2 u - \frac{(1-f_1)^2}{(f_1^3+\omega)}A_{\mathrm{mushy}}u \tag{7-2}$$

$$\frac{\rho_{\mathrm{PCM}}}{\varepsilon}\frac{\partial v}{\partial t}+\frac{\rho_{\mathrm{PCM}}}{\varepsilon^2}\left(\vec{U}\cdot\nabla v\right) = -\frac{\partial p}{\partial y}-\frac{\mu_{\mathrm{PCM}}}{K}v-\frac{\rho_{\mathrm{PCM}}F_1}{\sqrt{K}}|v|v+\frac{\mu_{\mathrm{PCM}}}{\varepsilon}\nabla^2 v+\rho_{\mathrm{PCM}}\,g\,\beta(T-T_{\mathrm{ml}})$$
$$-\frac{(1-f_1)^2}{(f_1^3+\omega)}A_{\mathrm{mushy}}v \tag{7-3}$$

$$\frac{\rho_{\mathrm{PCM}}}{\varepsilon}\frac{\partial u}{\partial t}+\frac{\rho_{\mathrm{PCM}}}{\varepsilon^2}\left(\vec{U}\cdot\nabla u\right) = -\frac{\partial p}{\partial z}-\frac{\mu_{\mathrm{PCM}}}{K}u-\frac{\rho_{\mathrm{PCM}}F_1}{\sqrt{K}}|u|u+\frac{\mu_{\mathrm{PCM}}}{\varepsilon}\nabla^2 u - \frac{(1-f_1)^2}{(f_1^3+\omega)}A_{\mathrm{mushy}}u \tag{7-4}$$

where ρ_{PCM} is the PCM density; u and v are the velocities in r and z directions, respectively; p is the pressure; μ_{PCM} is the PCM viscosity; g is the gravitational acceleration; β is PCM thermal expansion coefficient; T is the temperature; T_{ml} is the lower limit of melting point; f_1 is the melting fraction in each cell; ω is a small number (0.001) to prevent division by zero; A_{mushy} is the mushy zone constant (10^5) [21]. ε is the porosity; K is the permeability; F_{l} is the inertia coefficient. The second term on the right side of momentum equations accounts for the Darcy effect; the third term explains the Forchheimer-extended Darcy effect [11]. $\rho_{\mathrm{PCM}}\,g\,\beta(T-T_{\mathrm{ml}})$ represents the Boussinesq approximation to include the buoyancy effect. The last term in momentum equations is the damping term[21]. The melting fraction f_{l} quantifies the percentage of liquid PCM in the mushy zone and is evaluated as [51]:

$$f_{\mathrm{l}} = \frac{T - T_{\mathrm{m1}}}{T_{\mathrm{mu}} - T_{\mathrm{ml}}} = \begin{cases} 0 & \text{for } T < T_{\mathrm{m1}} \\ 0-1 & \text{for } T_{\mathrm{m1}} \leq T \leq T_{\mathrm{mu}} \\ 1 & \text{for } T > T_{\mathrm{mu}} \end{cases} \tag{7-5}$$

where T_{mu} is the upper limit of melting point.

Local thermal equilibrium is adopted because the temperature difference between the ceramic skeleton and salt is very small (< 0.52 °C) [142].

Energy equation is given by [90]:

$$\left[(1-\varepsilon)\rho_{\mathrm{ps}} c_{\mathrm{p,\,ps}} + \varepsilon\, \rho_{\mathrm{PCM}}\, c_{\mathrm{p,\,PCM}}\right] \frac{\partial T}{\partial t} + \rho_{\mathrm{PCM}}\, c_{\mathrm{p,\,PCM}} \left(\vec{U} \cdot \nabla T\right) = k_{\mathrm{ef}} \nabla^2 T - \varepsilon \rho_{\mathrm{PCM}} L \frac{df_{\mathrm{l}}}{dt} \tag{7-6}$$

where $c_{\mathrm{p,\,PCM}}$ and $c_{\mathrm{p,\,ps}}$ are the specific heat of PCM and porous skeleton respectively; k_{PCM} is the thermal conductivity of PCM; L is the latent heat; ρ_{ps} is the density of porous skeleton; k_{ef} is the effective thermal conductivity.

For the HTF, forced convection occurs and the governing equations are [149]:

Continuity equation:

$$\nabla \cdot \vec{u} = 0 \tag{7-7}$$

Momentum equation:

$$\rho_{\mathrm{HTF}} \frac{\partial \vec{u}}{\partial t} + \rho_{\mathrm{HTF}} (\vec{u} \cdot \nabla) \vec{u} = -\nabla p + \mu_{\mathrm{HTF}} \nabla^2 \vec{u} \tag{7-8}$$

Energy equation:

$$\rho_{\mathrm{HTF}}\, c_{\mathrm{p,\,HTF}} \frac{\partial T}{\partial t} + \rho_{\mathrm{HTF}}\, c_{\mathrm{p,\,HTF}}\, \vec{u} \cdot \nabla T = \nabla \cdot (k_{\mathrm{HTF}} \nabla T) \tag{7-9}$$

where ρ_{HTF}, $c_{\mathrm{p,\,HTF}}$ and k_{HTF} are density, specific heat and thermal conductivity of heat transfer fluid.

7.2.2 Thermo-physical properties

Solar salt (60 wt% $NaNO_3$ + 40 wt% KNO_3) was used as PCM while the ceramic foam act as thermal promotor. The thermo-physical properties are the same as those in Chapter 6 and are listed in Table 7.2.

Table 7.2: Thermo-physical properties of solar salt and ceramic.

Material	Parameter	Value
Solar salt	Density, kg/m^3	1980
	Latent heat, J/kg	140,000
	Melting point, °C	222.9 – 246.0
	Specific heat, J/(kg·K)	1575
	Thermal conductivity (solid/liquid), W/(m·K)	0.59/0.48
	Viscosity, mPa·s	4.61
	Thermal expansion coefficient, K^{-1}	5.47×10^{-5}
Ceramic	Thermal conductivity, W/(m·K)	20.7
	Specific heat, J/(kg·K)	800
	Density, kg/m^3	2327

The effective thermal conductivity is calculated using the extended Lemlich model [143]:

$$k_{\mathrm{ef,\,ps}} = \frac{1-\varepsilon}{3} k_{\mathrm{ps}} \tag{7-10}$$

$$k_{\mathrm{ef,\,PCM}} = \frac{2+\varepsilon}{3} k_{\mathrm{PCM}} \tag{7-11}$$

$$k_{\mathrm{ef}} = k_{\mathrm{ef,\,PCM}} + k_{\mathrm{ef,\,ps}} \tag{7-12}$$

where k_{ps} and k_{PCM} are the thermal conductivity of ceramic and salt, respectively.

The above correlations were developed based on the direct simulation of thermal conduction over a wide range of thermal conductivity ratios (0.001-1000) between the porous skeleton and filling medium. They have been compared with experimental data and show high accuracy [143]. Moreover, the correlations have a simple and elegant form of expression and can be used very easily. Therefore, they were adopted in the current simulation to predict effective thermal conductivity.

The permeability K and inertia coefficient F_l are calculated by [21]:

$$K = \frac{\varepsilon^2 \left(d_\text{fp}\sqrt{\kappa_\text{tor}/3\varepsilon}\right)^2}{36(\kappa_\text{tor} - 1)\kappa_\text{tor}} \tag{7-13}$$

$$F_\text{l} = 0.00212(1\text{-}\ \varepsilon)^{\text{-}0.132}\left(d_\text{fs}/d_\text{fp}\right)^{\text{-}1.63} \tag{7-14}$$

$$d_\text{fp} = \frac{25.4 \times 10^{\text{-}3}}{\text{PPI}} \tag{7-15}$$

$$d_\text{fs} = 1.18\sqrt{\frac{1 - \varepsilon}{3\pi}}\left[\frac{1}{1 - e^{(\varepsilon\text{-}1)/0.04}}\right] d_\text{fp} \tag{7-16}$$

$$\frac{1}{\kappa_\text{tor}} = \frac{3}{4\varepsilon} + \frac{\sqrt{9 - 8\varepsilon}}{2\varepsilon}\cos\left\{\frac{4\pi}{3} + \frac{1}{3}\cos^{\text{-}1}\left[\frac{8\varepsilon^2\text{-}36\varepsilon + 27}{(9 - 8\varepsilon)^{1.5}}\right]\right\} \tag{7-17}$$

These correlations are suitable for the solid-liquid phase change of PCM in porous foam [21].

The material of the shell and the tube is AISI316 stainless steel [150] and HTF is the mineral oil [151, 152]. Their properties are listed in Table 7.3.

Table 7.3: Properties of shell/tube material and HTF.

Material	Parameter	Value
AISI316 stainless steel	Thermal conductivity, W/(m·K)	16.2
	Specific heat, J/(kg·K)	502
	Density, kg/m^3	8000
Mineral oil	Thermal conductivity, W/(m·K)	0.1
	Specific heat, J/(kg·K)	2436
	Viscosity, mPa·s	1.085
	Density, kg/m^3	800

7.2.3 Initial and boundary conditions

For the whole computational domain, the initial conditions are:

$$u = v = w = 0,\;\; T = T_{\mathrm{ini}} \tag{7-18}$$

where T_{ini} is the initial temperature (200 °C).

HTF is injected with the temperature of 300 °C and the velocity of 0.05 m/s from the inlet. The outlet boundary is set as Outflow to ensure the mass conservation. The outer wall of the shell, the front and back surface of the whole computational domain except the HTF domain are set as adiabatic.

At the interface between the tube and HTF:

$$T_{\mathrm{HTF}} = T_{\mathrm{tube}},\;\; (-k_{\mathrm{HTF}}\,\nabla T_{\mathrm{HTF}})\cdot\boldsymbol{n} = (-k_{\mathrm{tube}}\,\nabla T_{\mathrm{tube}})\cdot\boldsymbol{n},\;\; u = v = w = 0 \tag{7-19}$$

At the interface between the tube and PCM:

$$T_{\mathrm{PCM}} = T_{\mathrm{tube}},\; (-k_{\mathrm{PCM}}\,\nabla T_{\mathrm{PCM}})\cdot\boldsymbol{n} = (-k_{\mathrm{tube}}\,\nabla T_{\mathrm{tube}})\cdot\boldsymbol{n},\;\; u = v = w = 0 \tag{7-20}$$

At the interface between the shell and PCM:

$$T_{\mathrm{PCM}} = T_{\mathrm{shell}},\; (-k_{\mathrm{PCM}}\,\nabla T_{\mathrm{PCM}})\cdot\boldsymbol{n} = (-k_{\mathrm{shell}}\,\nabla T_{\mathrm{shell}})\cdot\boldsymbol{n},\;\; u = v = w = 0 \tag{7-21}$$

7.2.4 Numerical procedure

ANSYS Fluent 18.0 package was utilised to solve the thermal transport problem. The governing equations were discretized using the finite volume method (FVM). The SIMPLE scheme was employed to couple pressure and velocity. The second-order upwind method was implemented to discretise pressure, momentum and energy terms. The under-relaxation factors were set as 0.3, 1, 1, 0.7, 0.9 and 1 for pressure, density, body forces, momentum, liquid fraction update and energy respectively. The convergence criteria for conservation equations of mass, momentum and energy were 10^{-4}, 10^{-4} and 10^{-6} respectively.

Three mesh sets (1,093,935 cells, 1,218,366 cells and 1,847,104 cells) and time steps (0.5 s, 1 s and 2 s) were tested to balance the computational accuracy and time. First, under the fixed time step of 1 s, three mesh sets were tested (H = 124.0 mm). The result of the mesh independence is shown in Figure 7.2(a). The maximum deviation in melting fraction is about 0.04, occurring at 4500 s. To save the computing resources, the medium mesh set (1,218,366 cells) was chosen. Then, under the fixed mesh of 1,218,366 cells, time step independence was checked. It is seen from Figure 7.2(b) that the time step almost has no effect on the melting fraction, therefore the time step of 2 s was used for the final setting.

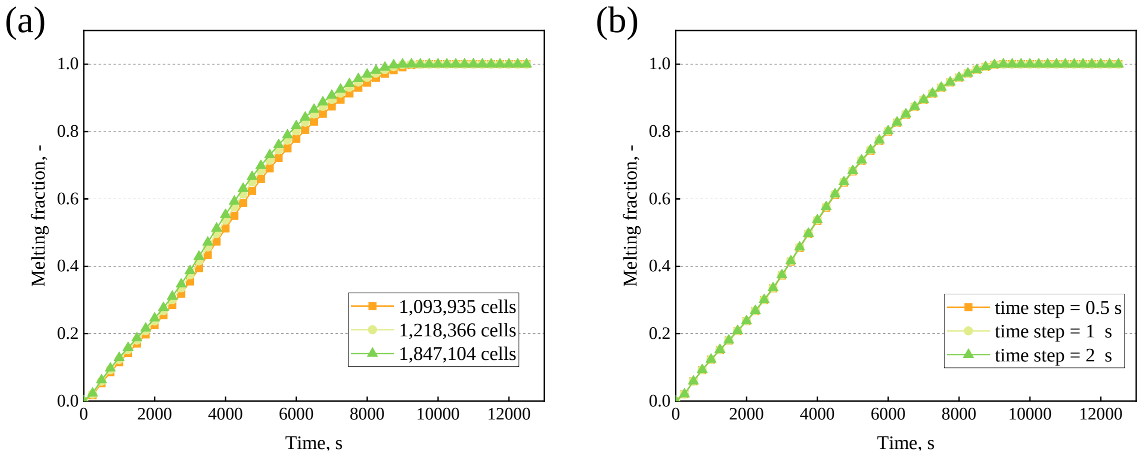

Figure 7.2: (a) Mesh independence analysis. (b) Time step independence analysis.

7.3 Model validation

Tian et al. [79] carried out experimental and numerical studies on the melting performance of paraffin/copper foam composite phase change material. In their experiment, the composite phase change material was placed in a rectangular cavity and heated by the bottom heater with constant heat flux. A thermocouple was inserted 8 mm from the bottom heat source to record the local temperature. The authors also performed a 2D numerical simulation to investigate the melting process. Their experimental and numerical results are used to verify the current model. The physical model is shown in Figure 7.3(a). Model parameters and thermo-physical properties are listed in Table 7.5. The same computational domain, boundary/initial conditions and thermo-physical properties are used in the validation. The simulated temperature at the monitored point, Tian et al.'s experimental and numerical results [79] and Liu et al.'s numerical results [91] are presented in Figure 7.3(b).

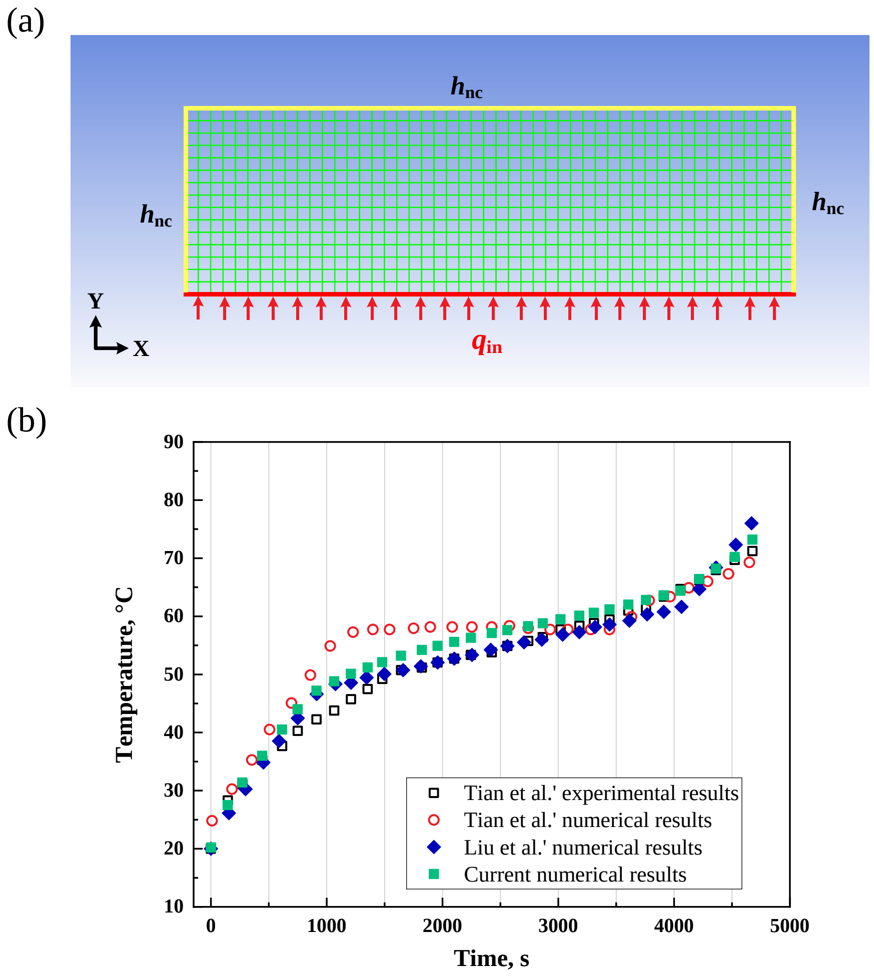

Figure 7.3: Physical model of experiment in Tian et al. [79]'s research. (b) Comparison of Tian et al. [79]'s experimental and numerical results, Liu et al. [91]'s numerical results and the current numerical results.

Table 7.4: Model parameters and thermo-physical properties [79, 91].

Parameter/property	Model	Paraffin	Copper foam
Size, mm	200 × 25	-	-
Heat flux, kW/m^2	1.6	-	-
Melting point, °C	-	48 – 62	-
Latent heat, J/kg	-	181,000	-
Specific heat, J/(kg·K)	-	2100	381
Thermal conductivity, W/(m·K)	-	0.2	350
Porosity, -	-	-	0.95

It is seen from Figure 7.3(b) that the temperature increases rapidly from 0 s to 1000 s. Then it rises slowly. After about 4000 s, the temperature rises rapidly again. This is because before the melting and after the complete melting, the absorbed heat is mainly used to increase the sensible heat, so the temperature increases rapidly. By contrast, during the melting process, the absorbed heat is mostly used to increase the latent heat, thus the temperature rises slowly. In Tian et al.'s numerical simulation [79], the composite phase change material was treated with a fixed melting point, so the temperature was almost unchanged during the melting process. The current numerical results are slightly larger than the experimental results. The reason may be the difficulty in establishing the complete adiabatic boundary in the experiment. The deviation between numerical and experimental results is within 10%. The overall trend of the simulated results is consistent with the experiment. And at the late stage, the simulated results are almost the same as the experimental ones, which verifies the reliability of the current model.

7.4 Results and discussions

7.4.1 Effect of filling height

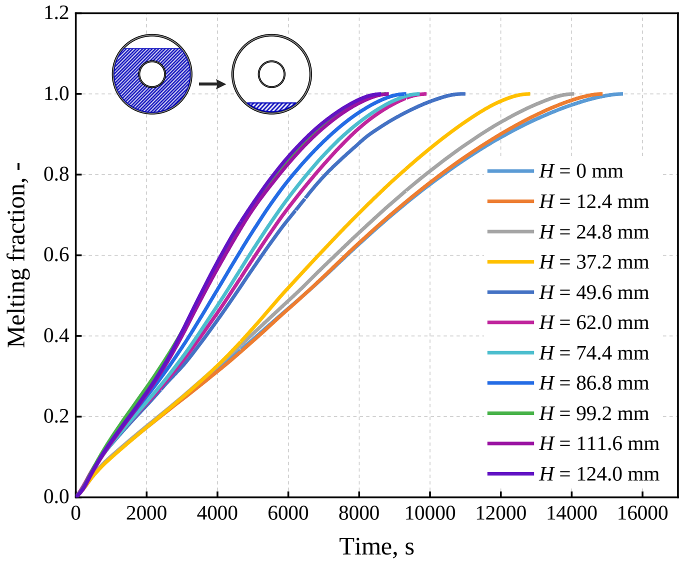

Figure 7.4: Effect of the filling height of the ceramic foam on melting fraction.

Figure 7.4 shows the variation of the melting fraction. The melting fraction rises faster as the filling height of the ceramic foam increases. It is noticeable that when the filling height is

49.6 mm (0.4 d_{si}) or more, the melting is accelerated remarkably; in comparison, when the filling height is lower than 49.6 mm, the melting is accelerated less significantly. The higher filling height means less PCM; meanwhile, the overall thermal conductivity is improved. Moreover, the ceramic foam with a height of 49.6 mm reaches the tube and helps conduct the heat of the tube, which also contributes to faster melting.

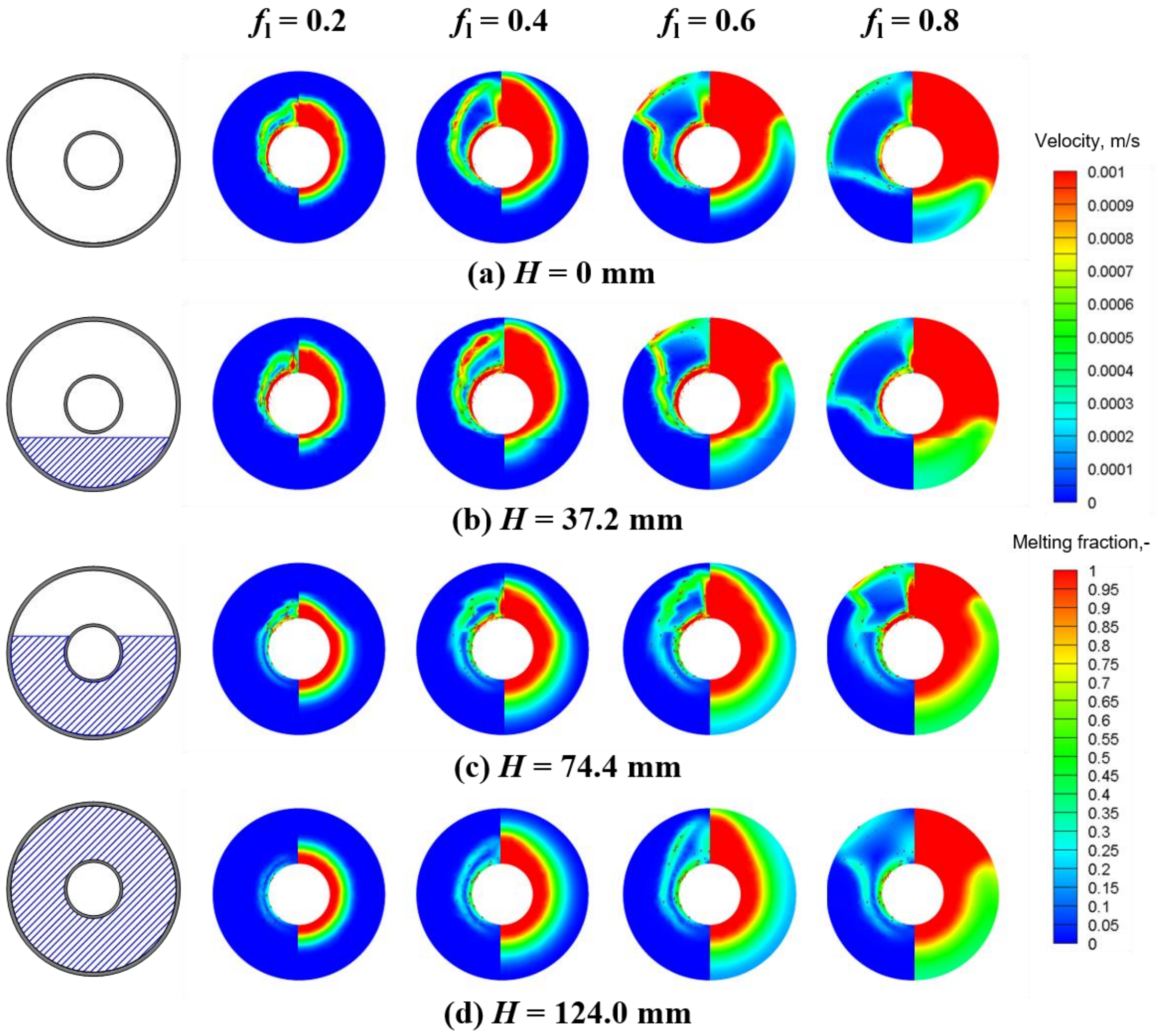

(a) $H = 0$ mm

(b) $H = 37.2$ mm

(c) $H = 74.4$ mm

(d) $H = 124.0$ mm

Figure 7.5: Velocity field (left semicircle) and melting front (right semicircle) at the melting fraction = 0.2, 0.4, 0.6 and 0.8 ($z = 250$ mm).

Figure 7.5 shows the velocity field and melting front at the plane of $z = 250$ mm. For the non-filled case ($H = 0$ mm), PCM which surrounds the tube first melts. Then, liquid PCM flows upwards under the buoyancy force (Figure 7.5(a)). After that, much PCM in the upper half portion is melted; in comparison, PCM under the tube is rarely melted. At $f_l = 0.8$, PCM in the upper half portion has been melted completely. The overall temperature is highest (Figure 7.6(a)), however, the fluid flow is weak, indicating that the impact of natural convection is small.

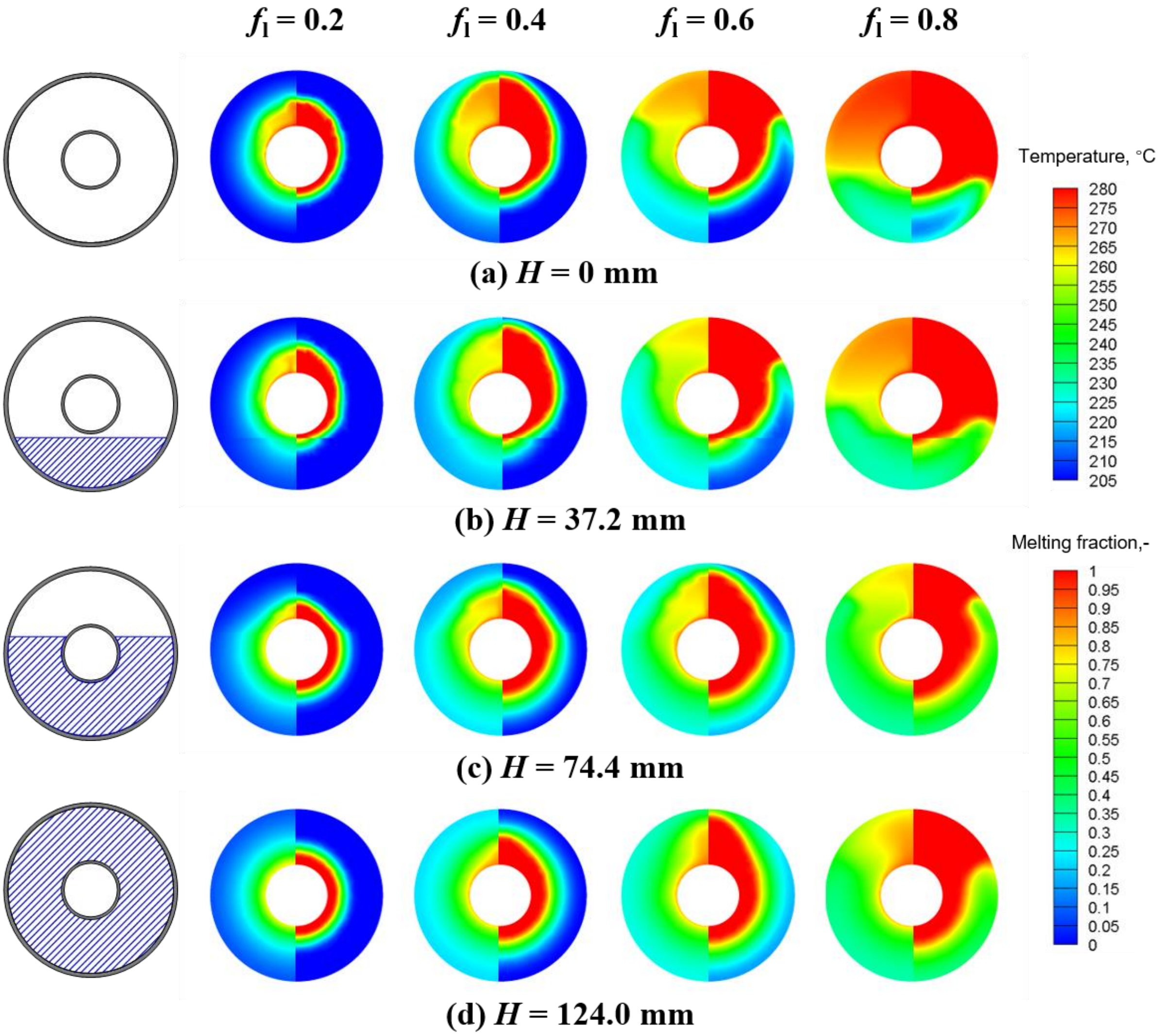

(a) $H = 0$ mm

(b) $H = 37.2$ mm

(c) $H = 74.4$ mm

(d) $H = 124.0$ mm

Figure 7.6: Temperature field (left semicircle) and melting front (right semicircle) at the melting fraction = 0.2, 0.4, 0.6 and 0.8 ($z = 250$ mm).

For the fully filled unit ($H = 124.0$ mm), the melting front is annular-shaped at the early stage. The velocity of liquid PCM is small, as shown in Figure 7.5(d), indicating the weak natural convection. With the elapse of time, the amount of liquid PCM increases and the influence of natural convection becomes significant. The phase interface is converted from annular-shaped to egg-shaped. Nevertheless, the distortion of the phase interface is still less obvious compared to the non-filled unit. It is noted that from f_l = 0.2 to 0.4, PCM under the tube is melted significantly; by contrast, for the non-filled case, PCM in this portion is rarely melted.

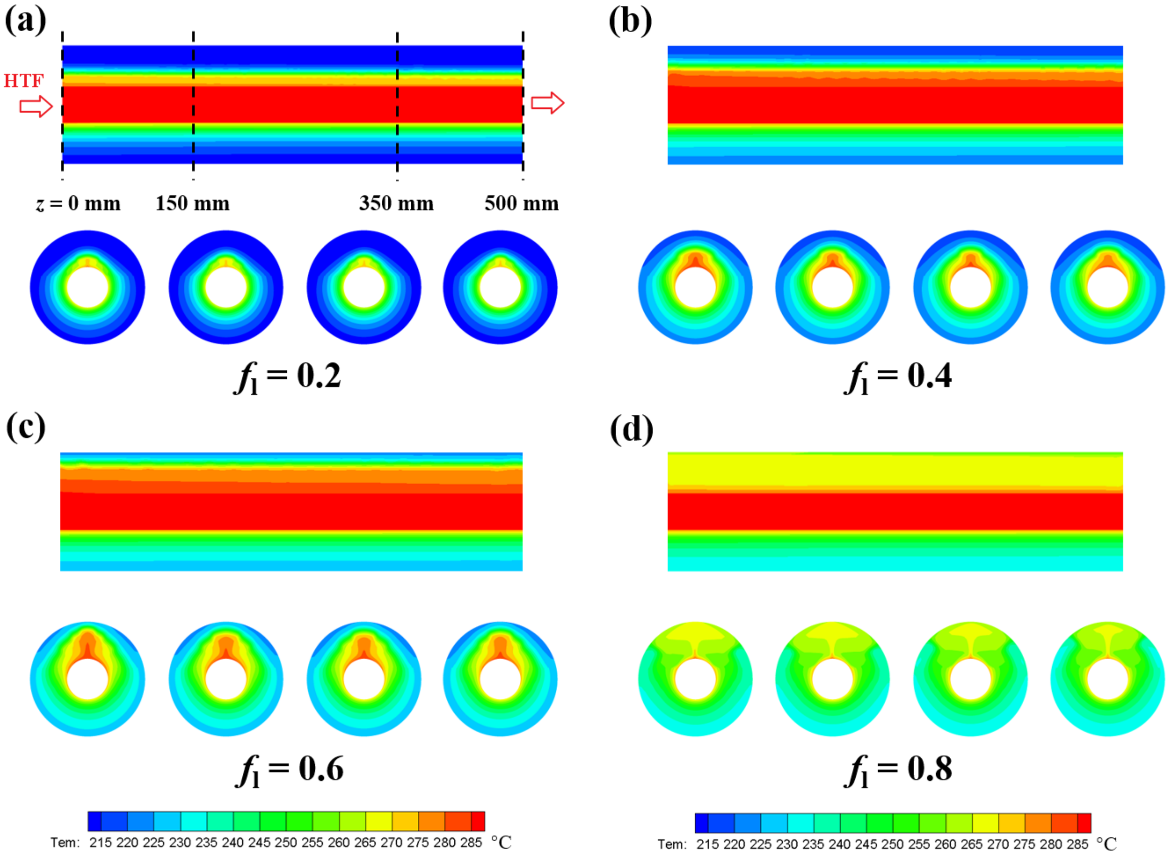

Figure 7.7: Variation of temperature fields along the axial direction at different melting fractions (H = 74.4 mm).

For the partially filled units, the melting is distinguished by the boundary between the pure PCM and the PCM/ceramic foam composite. Above the boundary, the fluid flow is strong and the mushy region is narrow; under the boundary, the flow is weak and the mushy region is wide. With the aid of the ceramic foam, the temperature of PCM in the lower region is slightly increased (Figures 7.6(a), (b) and (c)). The phase interface of the H = 37.2 mm case is similar to that of the non-filled case while the phase interface of the H = 74.4 mm case is similar to that of the fully filled case.

Figure 7.7 shows the temperature fields along the axial direction (H = 74.4 mm). It is found that the temperature fields are almost unchanged along the axial direction at f_l = 0.2.

After that, the influence of axial position becomes a bit significant. At f_l = 0.4, 0.6 and 0.8, the temperature decreases slightly with the HTF flow direction. Moreover, the influence of axial position is mainly exerted on the upper half.

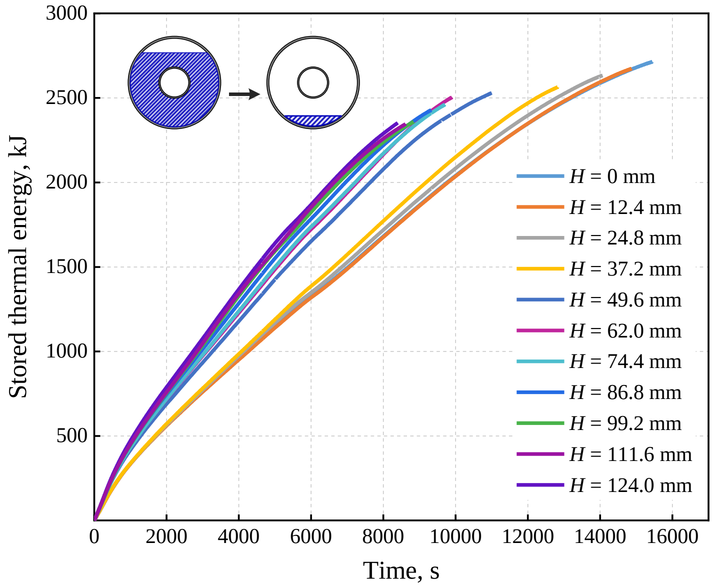

Figure 7.8: Effect of the filling height of the ceramic foam on the stored thermal energy.

Figure 7.8 shows the variation of the stored thermal energy. As the filling height increases, the thermal energy is stored faster. However, the effect of the filling height is different. When the filling height is 49.6 mm (0.4 d_{si}) or more, the improvement on the stored thermal energy is remarkable; by contrast, when the filling height is lower than 49.6 mm, the effect is insignificant. In other words, 49.6 mm is a critical point. This is not only because there is more ceramic foam inserted into the unit, but also because the ceramic foam reaches the tube and helps conduct the heat of the tube.

The total stored energy is calculated by:

$$E = (T_{\mathrm{fin}} - T_{\mathrm{ini}})m_{\mathrm{PCM}}c_{\mathrm{p,PCM}} + (T_{\mathrm{fin}} - T_{\mathrm{ini}})m_{\mathrm{ps}}c_{\mathrm{p,ps}} + m_{\mathrm{PCM}}L \tag{7-22}$$

The energy stored rate is calculated by:

$$w = \frac{E}{t_{\mathrm{m}}} \tag{7-23}$$

where T_{fin} is the final average temperature; T_{ini} is the initial temperature; m_{PCM} and $c_{\mathrm{p,PCM}}$ are the mass and the specific heat of PCM respectively; m_{ps} and $c_{\mathrm{p,ps}}$ are the mass and the specific heat of the porous skeleton respectively; t_{m} is the complete melting time.

The complete melting time, total stored energy and energy storage rate are plotted in Figure 7.9. The melting time always decreases with the filling height of the ceramic foam. Compared to the H = 0 mm case, the melting time of the H = 124.0 mm case is shortened by 43.9%. The total stored energy also decreases with the increase of the filling height. This is because the higher filling height means less PCM. The total stored energy of the H = 124.0 mm case is 13.6% lower than that of the H = 0 mm case. The energy storage rate always increases with the filling height. The energy storage rate of the H = 124.0 mm case is 54.9% larger than that of the H = 0 mm case, indicating the energy storage is accelerated significantly.

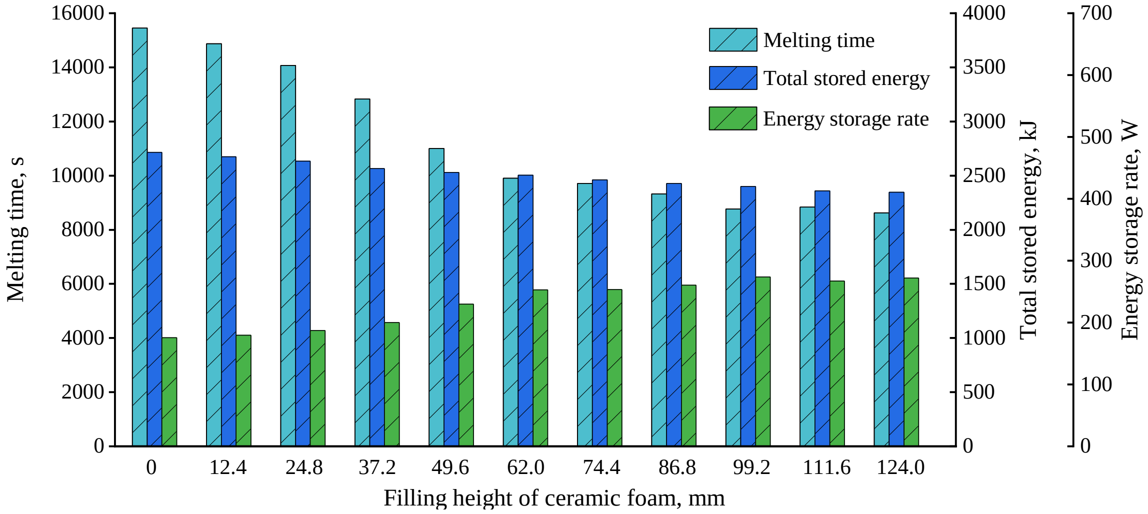

Figure 7.9: Variation of the complete melting time, total stored energy and energy storage rate with the filling height of the ceramic foam.

7.4.2 Effect of outer diameter

The velocity field and melting front under different outer diameters of the ceramic foam are presented in Figure 7.10. At f_{l} = 0.2, the velocity field of the d_{cf} = 54 mm case is obviously stronger compared to other cases. As the melting proceeds (f_{l} = 0.4), the velocity field of the

d_{cf} = 54 mm case keeps the strongest, while that of the d_{cf} = 74 mm case develops significantly. At f_l = 0.8, the velocity field of the four cases becomes similar.

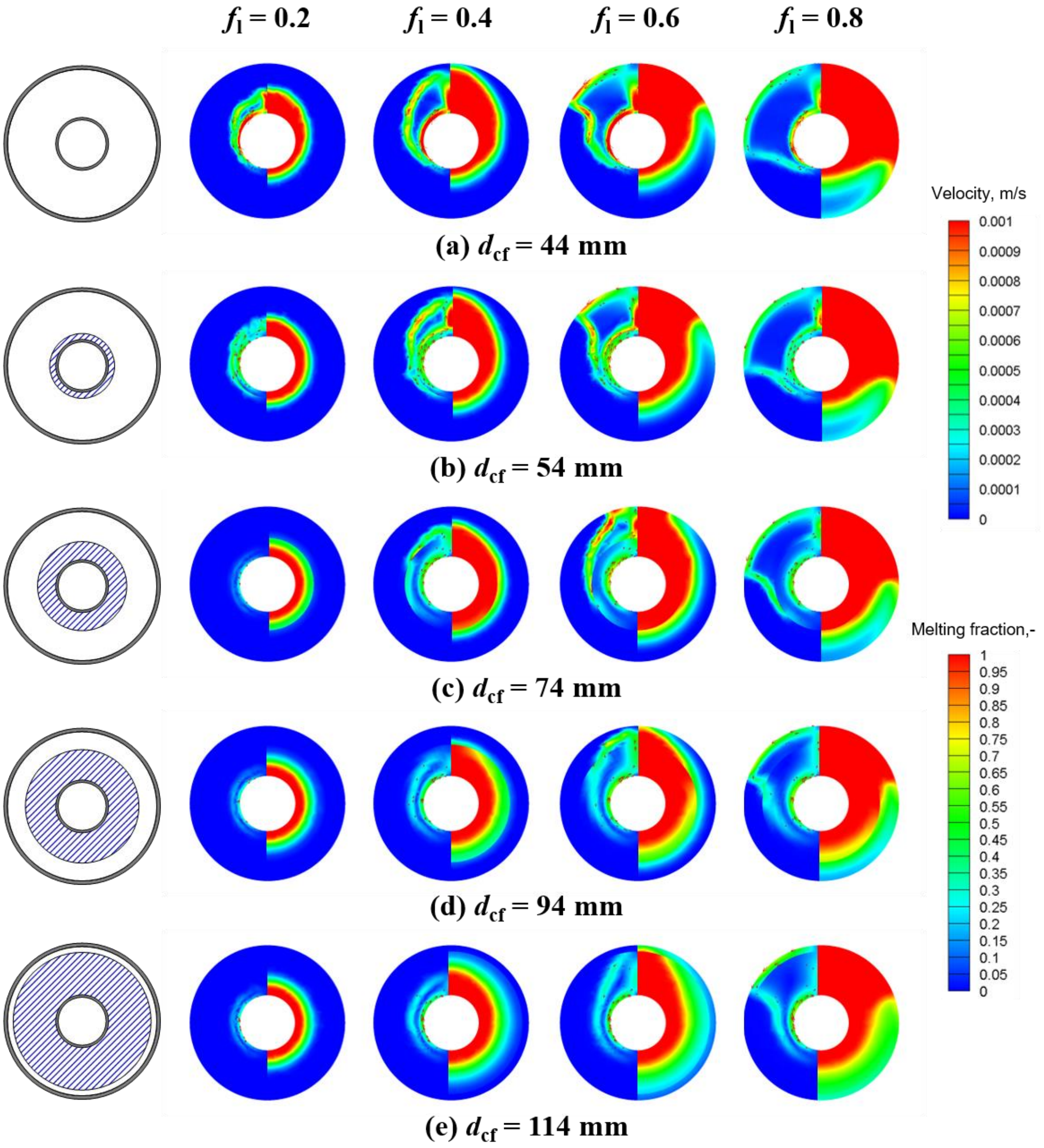

(a) d_{cf} = 44 mm

(b) d_{cf} = 54 mm

(c) d_{cf} = 74 mm

(d) d_{cf} = 94 mm

(e) d_{cf} = 114 mm

Figure 7.10: Velocity field (left semicircle) and melting front (right semicircle) under different outer diameters of the ceramic foam (z = 250 mm).

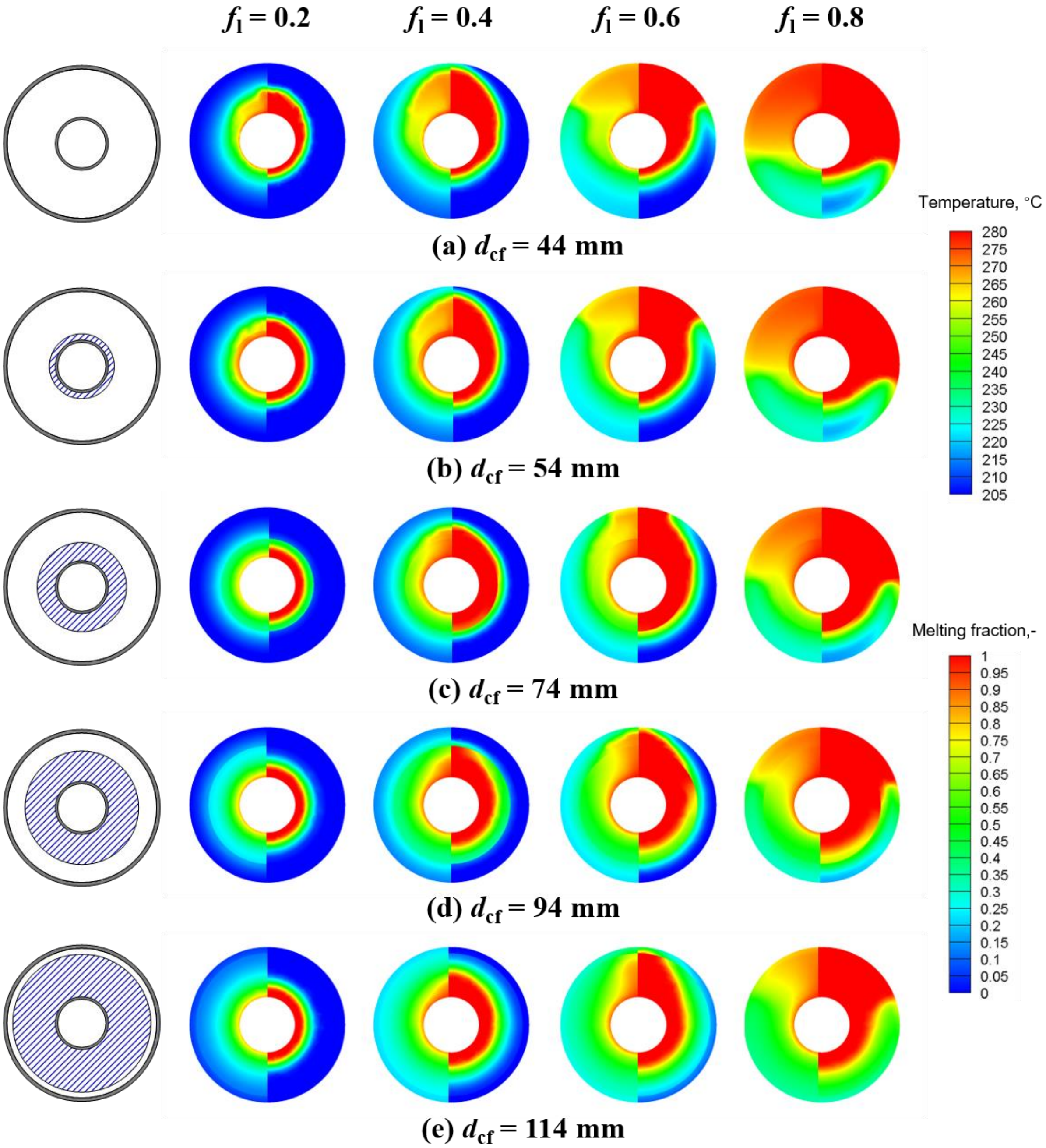

(a) d_{cf} = 44 mm

(b) d_{cf} = 54 mm

(c) d_{cf} = 74 mm

(d) d_{cf} = 94 mm

(e) d_{cf} = 114 mm

Figure 7.11: Temperature field (left semicircle) and melting front (right semicircle) under different outer diameters of the ceramic foam (z = 250 mm).

Figure 7.11 shows the temperature field. For the d_{cf} = 54 mm case, at f_l = 0.2, the high-temperature area is mainly around the tube. This is because the outer diameter of the ceramic foam is small and heat cannot be effectively transferred to the pure PCM area. When the melting fraction reaches 0.4, the temperature difference of the d_{cf} = 114 mm case is minimum.

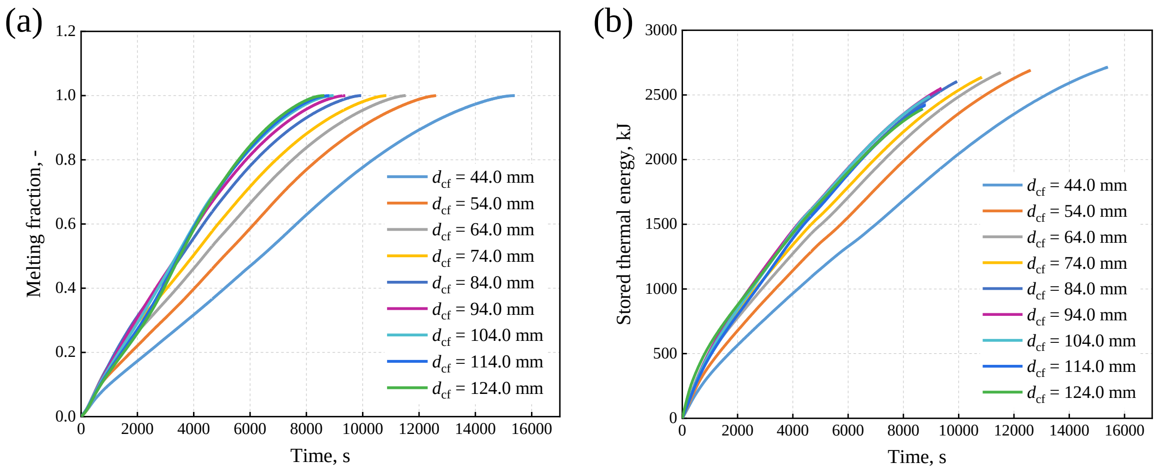

Figure 7.12: Variation of (a) melting fraction and (b) stored thermal energy under different outer diameters of the ceramic foam.

Figure 7.12(a) shows the variation of melting fraction with time under different outer diameters. As the outer diameter increases, the melting is accelerated. However, the effect of the outer diameter is different. When the ceramic foam is initially inserted into the unit, i.e. d_{cf} = 54 mm (d_{cf} = 44 is the non-inserted case), the melting is accelerated remarkably; as the outer diameter increases, the difference in the enhancement performance becomes less remarkable. This phenomenon can also be found in the stored thermal energy (Figure 7.12(a)). It may be explained as follows: when the ceramic foam is initially inserted into the unit, it completely surrounds the tube and helps directly conduct the heat of the tube; as the outer diameter increases, the contact area between the ceramic foam and the tube does not increase though and the newly-added ceramic foam would not conduct the heat of the tube directly.

It is seen from Figure 7.13 that the melting time and the total stored energy decrease with the increase of the outer diameter. The energy storage rate generally increases with the outer diameter except for the d_{cf} = 114.0 mm case. The energy rate of the d_{cf} = 104 mm case is the highest.

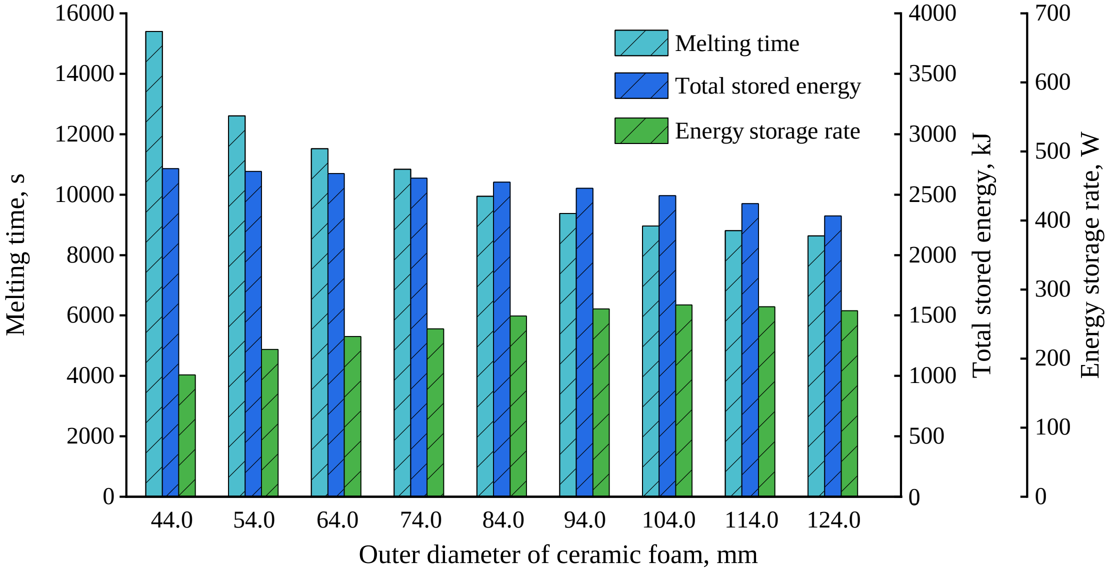

Figure 7.13: Variation of the complete melting time, total stored energy and energy storage rate with the outer diameter of the ceramic foam.

7.4.3 Effect of porosity

It is seen from Figure 7.14(a) that the lower the porosity, the faster the melting. At ε = 0.95, the complete melting time is 12492s, while at ε = 0.70, the melting time is 5506s. Compared to the non-filled case (15400s), the melting time is shorted by 18.9% and 64.2% respectively. It should be noted that the accelerated melting is partly because of the more ceramic foam which enhances heat conduction. Another reason is that the proportion of PCM is decreased. It is found from Figure 15(d) that as the porosity decreases, thermal energy is stored faster. However, the effect of porosity is different. When the porosity decreases from 0.95 to 0.90, thermal energy is stored faster significantly. By contrast, when the porosity decreases from 0.75 to 0.70, the difference is insignificant. This should be attributed to the effective thermal conductivity. Taking the solid state as the example, the effective thermal conductivity of cases with 0.95, 0.90, 0.75 and 0.70 porosities is 0.93 W/(m·K), 1.26 W/(m·K), 2.27 W/(m·K), 2.60 W/(m·K) respectively. The increase in the effective thermal conductivity is more significant (35%) when the porosity decreases from 0.95 to 0.90, which results in a remarkable difference in the stored thermal energy.

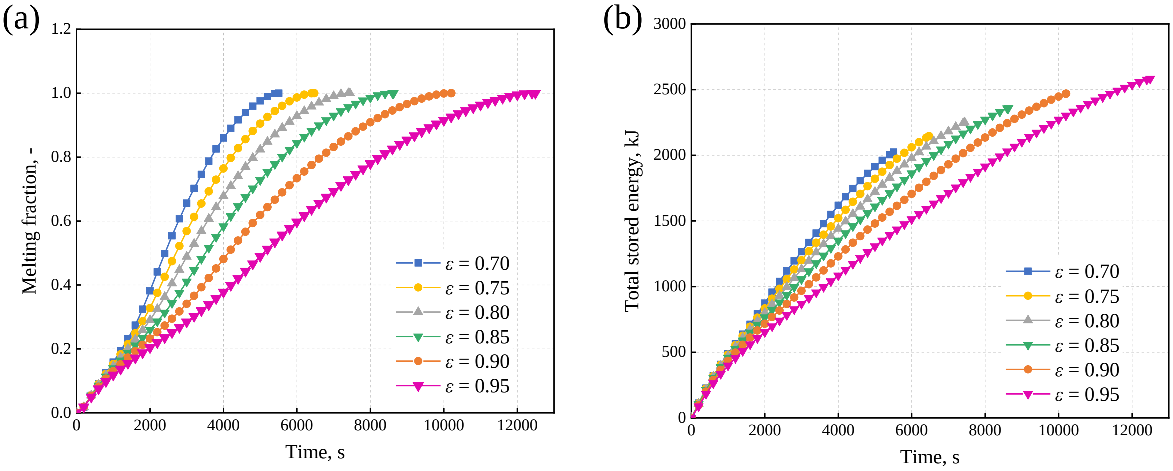

Figure 7.14: Variation of (a) melting fraction and (b) stored thermal energy under different porosities.

Figure 7.14(b) shows the variation of the stored thermal energy under different porosities. Figure 7.15 presents the melting time, total stored energy and energy storage rate. The effect of the porosity on the three parameters is similar to that of the filling height. As the porosity decreases, the melting time and total stored energy decrease while the energy storage rate increases.

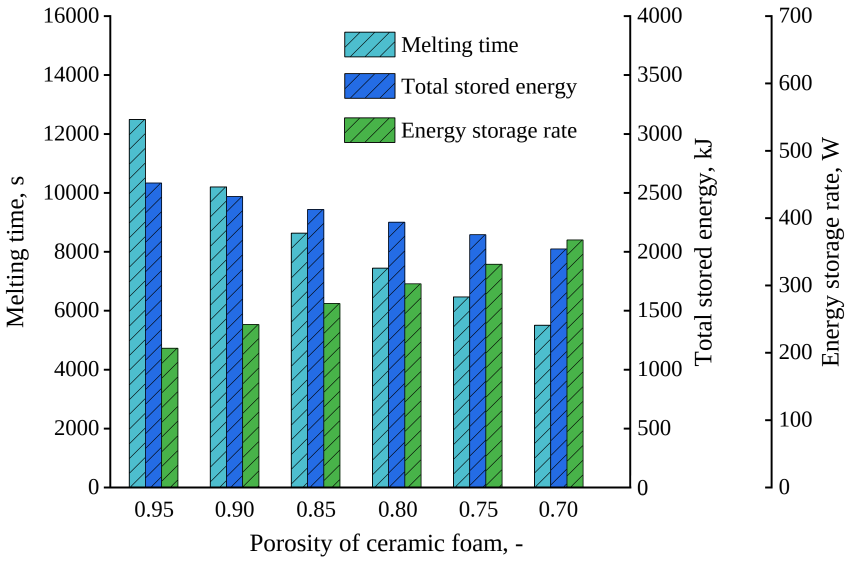

Figure 7.15: Variation of the complete melting time, total stored energy and energy storage rate with the porosity of the ceramic foam.

7.4.4 Comparison between different factors

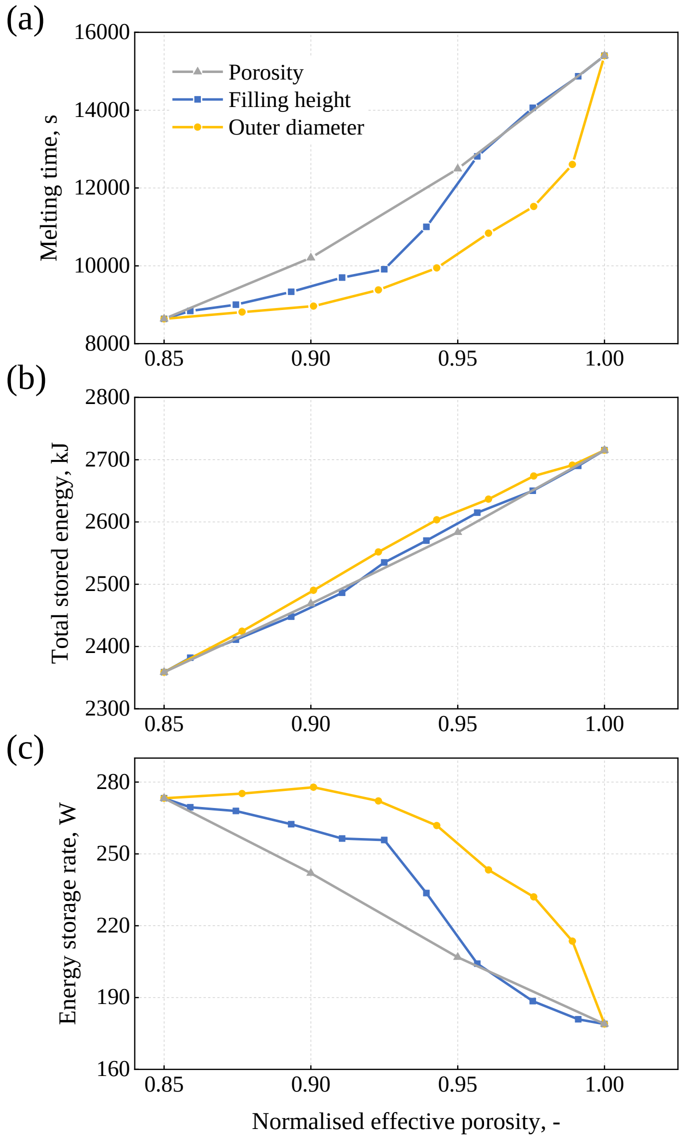

Figure 7.16: (a) Melting time, (b) total stored energy and (c) energy storage rate under different normalised effective porosities induced by the porosity, filling height and outer diameter.

The effect of the filling height, outer diameter and porosity are compared in terms of melting time, total stored energy and energy storage rate. Since they are different variables and cannot be compared directly, the normalised effective porosity, $\varepsilon_{\mathrm{ef}}$, is defined:

$$\varepsilon_{\mathrm{ef}} = 1 - \frac{V_{\mathrm{cf}}}{V_{\mathrm{an}}} \tag{7-24}$$

where V_{cf} is the volume of ceramic foam; V_{an} is the volume of the annulus of the shell-and-tube unit. By defining this parameter, the filling height and outer diameter are converted to the normalised effective porosity and the three factors can be compared.

Figure 7.16(a) shows the variation of the melting time under different $\varepsilon_{\mathrm{ef}}$. The $\varepsilon_{\mathrm{ef}}$ induced by the outer diameter has the shortest melting time. This is because the ceramic foam completely surrounds the tube and concentrates around the tube; therefore, the performance of conducting the heat of the tube is the best. Figure 7.16(b) presents the variation of the total stored energy under different $\varepsilon_{\mathrm{ef}}$. The $\varepsilon_{\mathrm{ef}}$ induced by the outer diameter corresponds to the largest total stored energy. Moreover, it has the highest energy storage rate (Figure 7.16(c)). Therefore, it can be concluded that the ceramic foam with varying outer diameters is optimal.

7.4.5 Comparison with other studies

In order to demonstrate the effect of ceramic foam on energy storage performance more clearly, the current work is compared with studies using metal foam. The basic configuration of the selected studies is the horizontal shell-and-tube unit, the same as the current study. The key parameters and results are listed in Table 7.5.

It is seen that metal foam and ceramic foam can accelerate the melting of PCM to different extents. The effect of copper foam is very significant. In Xu et al. [90]'s research, the porosity of copper foam is 0.95 and the melting time of the full-foam inserted case can be shortened by over 86% compared to no foam inserted case. This should be attributed to the high thermal conductivity of copper (350 W/(m·K)). The effect of aluminium foam is also remarkable. In Ge et al. [153]'s study, the porosity of aluminium foam is 0.90. The melting time of the aluminium foam inserted case is saved by 88%. The thermal conductivity of aluminium is 160 W/(m·K), much lower than that of copper foam. However, the thermal conductivity of paraffin is quite small, which is 0.2 W/(m·K) [153], so the enhancement effect of aluminium foam is still remarkable compared to the case of pure paraffin. The enhancement effect of ceramic foam on the melting of solar salt is less significant compared to metal foam: the melting time of the full-foam inserted case is shortened by 44%. This is because the thermal conductivity of ceramic is relatively low (20.7 W/(m·K)); another reason is that the thermal conductivity of solar salt is relatively high (0.59 W/(m·K)), in comparison with paraffin. Nevertheless, ceramic has the advantage of corrosion resistance while corrosion is a big problem for Cu and Al. And the cost of ceramic is lower than Cu and Al. So, ceramic is a promising candidate as the thermal enhancer of salt.

Table 7.5: Comparison of the performance between ceramic foam and metal foam.

Source	PCM	Foam	Outcomes
[153]	Paraffin	Aluminium alloy foam, $\varepsilon = 0.90$	(1) The melting time of the full foam-filled case is 3800 s, shortened by 88% compared to the no foam-filled case (33000 s). (2) The dimensionless energy storage rate is increased by 2.3 times.
[154]	Paraffin	Aluminium foam, $\varepsilon = 0.95$	(1) The solidification time of the full foam-filled case is 558 s, shorten by 92% compared to the no foam-filled case (6900 s). (2) The energy discharge capacity is decreased by less than 1%. (3) The energy discharge rate is increased by 11 times.
[90]	Li_2CO_3-K_2CO_3	Copper foam, $\varepsilon = 0.95$	(1) The melting time of the full foam-filled case is 2809 s, shorten by 86% compared to the no foam-filled case (20423 s). (2) The dimensionless energy storage rate is increased by 6.7 times.
This work	$NaNO_3$-KNO_3	Ceramic foam, $\varepsilon = 0.85$	(1) The melting time of the full foam-filled case is 8634 s, shortened by 44% compared to the no foam-filled case (15400 s). (2) The total stored energy is decreased by 14%. (3) The energy storage rate is increased by 55%.

7.5 Summary

In this chapter, the melting performance of ceramic foam/salt CPCM in a shell-and-tube unit is evaluated. Various characteristics including melting front, temperature response, flow field, energy storage rate and total stored energy are analysed. Multiple factors, namely the filling height, porosity and outer diameter of the ceramic foam are considered and compared to obtain an optimal configuration. This study provides comprehensive heat transfer and energy storage information for practical applications. The conclusions are drawn as follows:

(1) Thermal energy is stored faster as the filling height of the ceramic foam increases. However, the effect of the filling height is different. 49.6 mm (0.4 inner diameter of the shell) is a critical point. When the ceramic foam reaches the inner tube, the enhancement performance is remarkable, while it is insignificant in the case of below the inner tube.

(2) The porosity of the ceramic foam has a similar effect to the filling height on melting time, total stored energy and energy storage rate. In terms of the outer diameter, the enhancement performance of ceramic foam with a small outer diameter is significant; as the outer diameter increases, the difference in the enhancement gets less remarkable.

(3) The effects of the filling height, outer diameter and porosity are compared through a normalised effective porosity and the ceramic foam with varying outer diameters is found to be optimal.

(4) The enhancement performance of ceramic foam is less significant than that of metal foam. However, the corrosion resistance and low cost make it a promising thermal enhancer for salt.

Chapter 8 - Thermal performance under solar fluctuation

8.1 Introduction

Organic Rankine Cycle (ORC) is a widely recognised technology to convert solar heat to power with high reliability and low cost [7, 155]. It is based on the principle of the Rankine cycle and employs organics with low boiling points as working fluids [156]. Although the conventional steam Rankine cycle has higher efficiency when using heat sources over 400 °C, the temperature is out of reach for many solar collectors [157]. ORC is the most efficient power cycle below 400 °C [158], which makes it friendly to many current solar collector technologies. Solar ORC is a promising approach to converting low-to-medium-temperature solar heat into electricity. However, solar radiation has unsteady and intermittent nature, resulting in ORC systems operating under off-design conditions [159]. Latent heat thermal energy storage (LHTES) is a promising solution to buffer solar fluctuation [160, 161]. It stores unsteady solar heat in phase change materials (PCMs) and releases steady heat to ORC so that ORC can operate under design conditions [162, 163]. In sensible heat thermal energy storage (SHTES), the flow rate of the heat transfer fluid (HTF) has to be controlled accurately according to the solar fluctuation so as to keep the temperature of the storage tank constant. In comparison, LHTES does not need accurate control of the HTF flow rate. A constant flow rate is fine because the temperature of the storage tank does not have to be kept constant. This reduces the equipment requirement and avoids control lag. Moreover, as the thermal condition of the LHTES storage tank is known, it is easy to optimise the system. From these points of view, LHTES is more reliable and attractive.

Solar radiation is unsteady and has specific fluctuating characteristics. It is essential to study the thermal performance under solar fluctuation to understand the practical energy storage process. This chapter aims to investigate the thermal performance of a typical storage system under solar fluctuation. The study improves the understanding of the practical energy storage process and gives essential energy storage information for the design/optimisation of integrated LHTES-ORC systems.

8.2 Numerical modelling

To achieve the continuous operation of ORC, the TES subsystem is configured with two storage tanks (Figure 8.1**)**. The working process of the integrated system is as follows. HTF flows through the solar field and its temperature is increased. The hot HTF flows to storage tank A(B), and the charging of storage tank A(B) starts. When storage tank A(B) is fully charged, hot HTF switches to storage tank B(A) and the charging of storage tank B(A) starts. At the same time, storage tank A(B) starts to discharge to supply heat to ORC until the temperature of storage tank A(B) decreases to the minimum driving temperature of ORC. Tanks A and B charge/discharge alternately so that the solar energy is made the most use of and power is produced continuously.

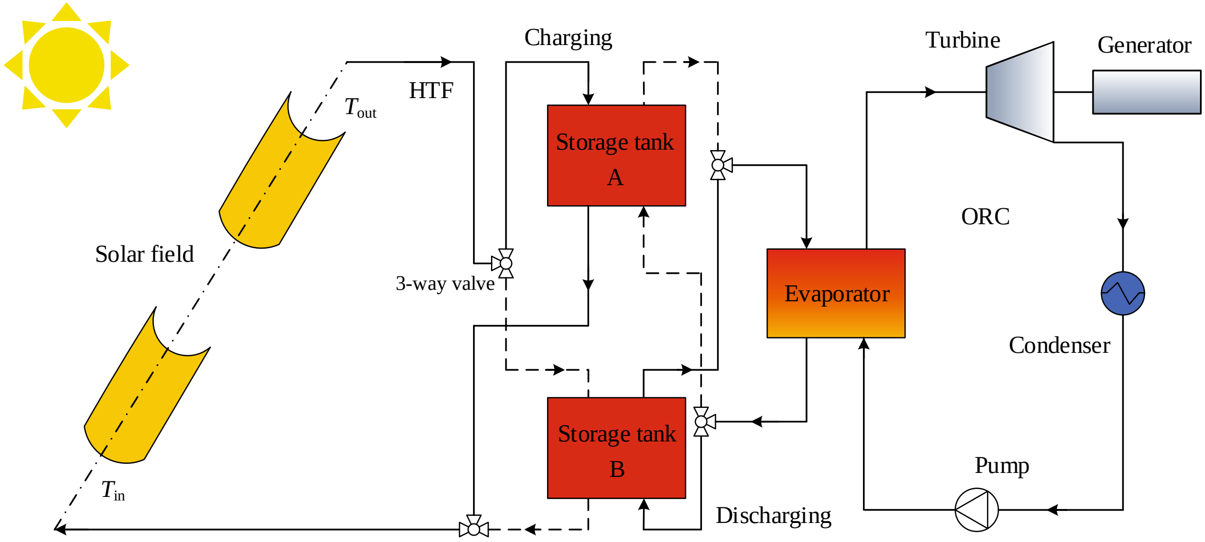

Figure 8.1: Schematic of TES-ORC integrated system with two storage tanks.

8.2.1 Solar radiation

The global solar radiation on the Earth’s surface consists of direct and diffuse radiation. Direct radiation is also called direct normal irradiance (DNI). Only DNI can be used by parabolic trough collectors [156]. The most direct method to obtain DNI is using a pyranometer to measure solar radiation. However, it is very difficult to obtain the pyranometer-measured data at a specific place because it is very likely that this place has no pyranometer installed. SOLCAST API Toolkit provides DNI data which is based on cloud images taken by weather satellites along with a series of modelling [164]. This toolkit has been validated by an actual pyranometer measurement (Global Horizontal Irradiance) at a solar farm [165]. And it has been widely used by people in the solar industry. So this toolkit was employed in the current study to get DNI data. Nottingham, the UK was chosen, although the UK is not rich in solar radiation due to a great number of rainy days. The location is only used to illustrate the effect of solar fluctuation while the practical situation needs to consider multiple factors such as policy, market, capital, etc. The DNI on a sunny and cloudy day [164] is presented in Figure 8.2. The total daily DNI on the sunny and cloudy day are 9.13 kWh/m^2 and 4.60 kWh/m^2 respectively.

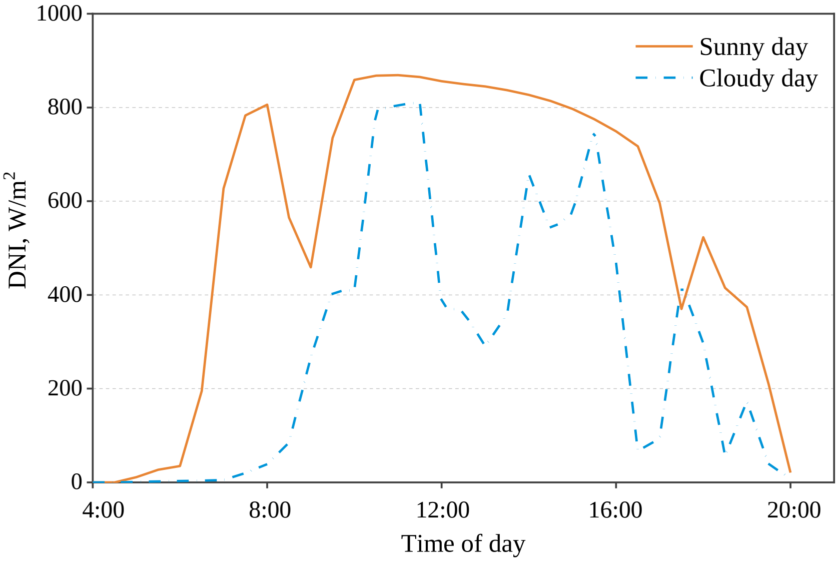

Figure 8.2: Direct normal irradiance (DNI) in Nottingham, the UK on a sunny (15th, June) and cloudy day (8th, June) [164].

The total solar energy absorbed by the solar collector depends on DNI (G), collector aperture (A_c) and collector efficiency (η_c) [156]:

$$Q_{solar} = G \cdot A_c \cdot \eta_c \tag{8-1}$$

In the current study, A_c is set as 1.6 m^2. Commercial EuroTrough ET-150 is chosen as the parabolic trough collector (PTC) and the collector efficiency is [156]:

$$\eta_c = 0.75 - 0.000045\cdot\left(T_{\mathrm{solar,\ inlet}} - T_{\mathrm{am}}\right) - 0.039\cdot\left(\frac{T_{\mathrm{solar,\ inlet}} - T_{\mathrm{am}}}{G}\right) - 0.0003\cdot G\cdot\left(\frac{T_{\mathrm{solar,\ inlet}} - T_{\mathrm{am}}}{G}\right)^2 \tag{8-2}$$

where T_{am} is the ambient temperature; $T_{\mathrm{solar,\ inlet}}$ is the temperature of HTF at the inlet of solar collector. T_{am} is got from SOLCAST API Toolkit [164] and plotted in Figure 8.3.

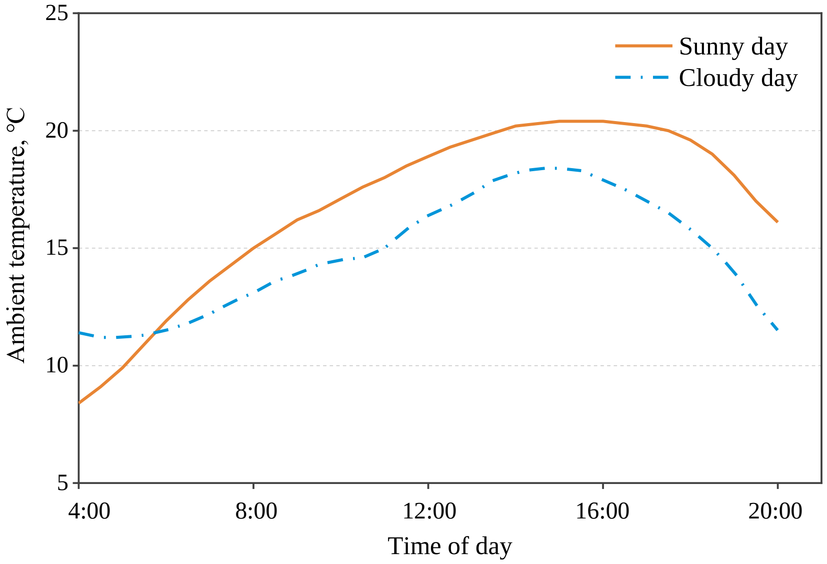

Figure 8.3: Ambient temperature on a sunny and cloudy day [164].

HTF flows through the solar collector and its temperature is increased. The hot HTF is the heat source of TES. The energy conservation equation in the solar collector is given by [156]:

$$\int c_{\mathrm{p,\ HTF}}\left(T_{\mathrm{solar,\ outlet}} - T_{\mathrm{solar,\ inlet}}\right) m_c\, dt = \int G\cdot A_c\cdot\eta_c\, dt \tag{8-3}$$

where $c_{\mathrm{p,\ HTF}}$ is the specific heat of HTF; $T_{\mathrm{solar,\ outlet}}$ is the temperature of HTF at the outlet of solar collector; m_c is the mass flow rate of HTF. To highlight the effect of solar fluctuation, $T_{\mathrm{solar,\ inlet}}$ is assumed constant, equal to the minimum driving temperature of ORC (125 °C [166]), so $T_{\mathrm{solar,\ outlet}}$ only depends on meteorological conditions.

8.2.2 Shell-and-tube TES system

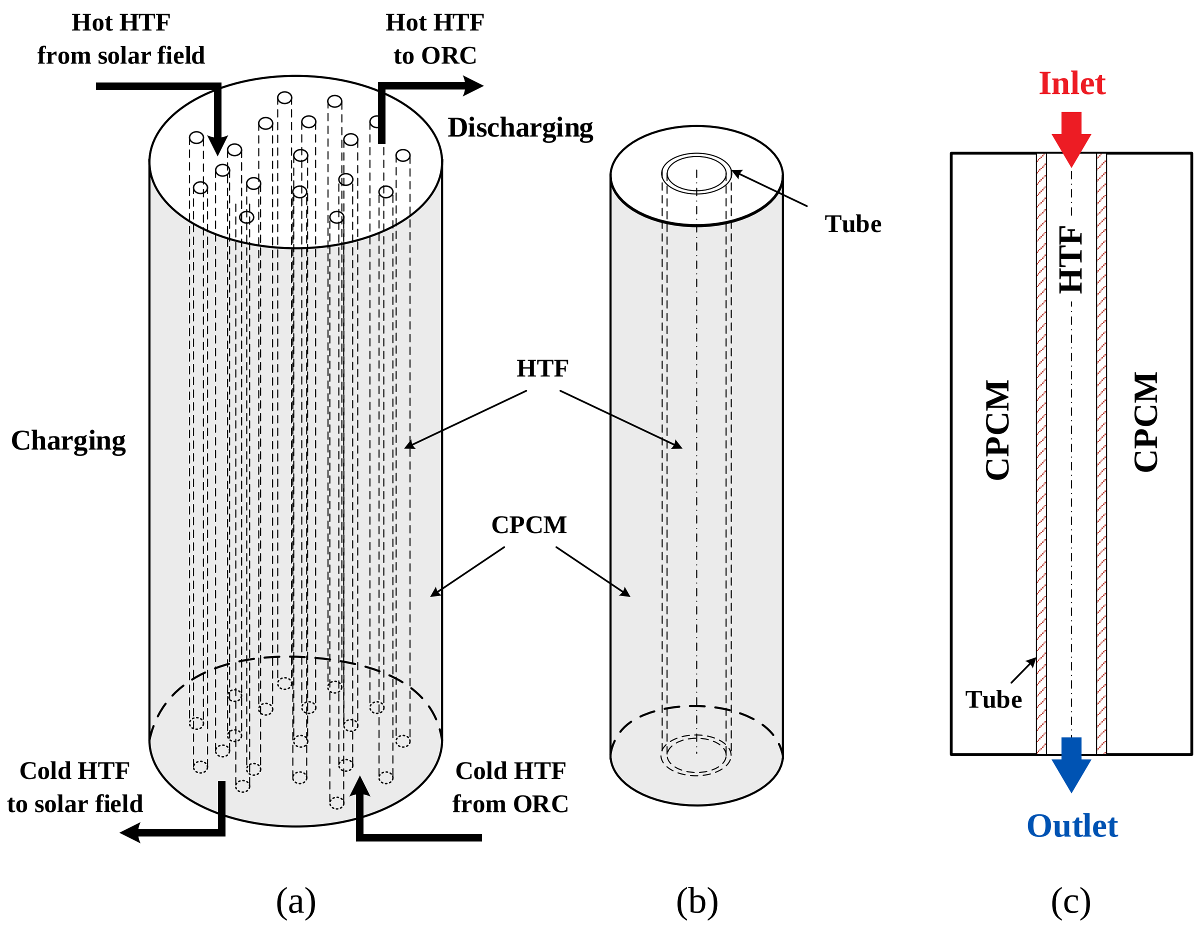

Figure 8.4: Schematic of (a) the shell-and-tube system; (b) the represented unit and (c) physical model used in the current simulation.

The shell-and-tube system is a widely used configuration for thermal energy storage in solar power plants [167]. The schematic of a typical shell-and-tube system is shown in Figure 8.4(a). There are many tubes in the cylindrical tank. The HTF flows through tubes and exchanges heat with PCM in the surrounding region. During the charging process, the hot HTF from the solar field flows to the shell-and-tube system and supplies heat to PCM. It enters the storage tank from the top inlet and exits from the bottom outlet. In the current configuration, storage tanks A and B charge alternately. It is assumed that when one storage tank is fully charged (melting fraction of PCM = 1), the other tank starts to charge immediately. And each charging process starts with a fully discharged state where the initial temperature is the minimum driving temperature of ORC ($T_{\text{min, ORC}}$, 125 °C [166]). The charging process stops when PCM is melted completely (melting fraction = 1).

Assuming the flow in each tube is identical, the energy storage process in the system can be represented by a single unit [167-169]. As Figure 8.4(b) shows, HTF flows through the tube while PCM fills in the annulus space of the unit with the adiabatic conditions at the outer PCM surface. The alternate charging in tanks A and B is represented by the continuous charging in one unit. Due to symmetry, the shell-and-tube unit can be further simplified into a two-dimensional physical model [167], as indicated in Figure 8.4(c).The dimension of the physical model used in the current study is listed in Table 8.1.

Table 8.1: Dimension of the physical model.

Parameter	Outer radius of unit (mm)	Length of unit (mm)	Outer radius of tube (mm)	Inner radius of tube (mm)
Value	30	300	8.75	6.25

8.2.3 Materials and properties

In the current study, solar salt (60wt% $NaNO_3$ + 40wt% KNO_3) is used as PCM. First, the thermal performance of TES unit containing pure salt is investigated. Subsequently, the use of ceramic foam to enhance the heat transfer of salt is assessed. Thermo-physical properties of solar salt and ceramic foam are the same as those in Chapter 6 and are listed in Table 8.2.

AISI316 stainless steel is used as the tube material [150] and the mineral oil as HTF [151, 152]. Their properties are listed in Table 8.3.

Table 8.2: Properties of solar salt and ceramic foam.

Material	Parameter	Value
Solar salt	Density, kg/m^3	1980
	Latent heat, J/kg	140,000
	Melting point, ℃	222.9 – 246.0
	Specific heat, J/(kg·K)	1575
	Thermal conductivity (solid/liquid), W/(m·K)	0.59/0.48
	Viscosity, mPa·s	4.61
	Thermal expansion coefficient, K^{-1}	5.47 ×10^{-5}
Ceramic foam	Thermal conductivity, W/(m·K)	20.7
	Specific heat, J/(kg·K)	800
	Density, kg/m^3	2327
	Porosity, -	0.85
	Pore density, PPI	10

Table 8.3: Properties of the tube material and HTF [150-152].

Material	Parameter	Value
AISI316 stainless steel	Thermal conductivity, W/(m·K)	16.2
	Specific heat, J/(kg·K)	502
	Density, kg/m^3	8000
Mineral oil	Thermal conductivity, W/(m·K)	0.1
	Specific heat, J/(kg·K)	2436
	Viscosity, mPa·s	1.085
	Density, kg/m^3	800

8.2.4 Governing equations

A two-dimensional transient heat transfer model based on the enthalpy method is developed to simulate the energy storage process. During the numerical modelling, the following assumptions were made: (1) the porous skeleton and PCM are homogeneous and isotropic; (2) the flow of liquid PCM is laminar and incompressible; (3) the liquid PCM is subjected to the Boussinesq approximation; (4) the local thermal equilibrium exists between PCM and the porous skeleton; (5) the volume difference of PCM before/after melting is neglected; (6) thermo-physical properties are temperature-independent; (7) the HTF outlet temperature from the solar field equals the HTF inlet temperature to the shell-and-tube unit.

The governing equations are summarised as follows:

Continuity equation [61]:

$$\nabla \cdot \vec{U} = 0 \tag{8-4}$$

Momentum equations for the case without ceramic foam [11, 51]:

$$\rho_{\text{PCM}} \frac{\partial u}{\partial t} + \rho_{\text{PCM}} \left(\vec{U} \cdot \nabla u \right) = -\frac{\partial p}{\partial r} + \mu_{\text{PCM}} \nabla^2 u - \frac{\left(1 - f_1\right)^2}{\left(f_1^3 + f_1\right)} A_{\text{mushy}} u \tag{8-5}$$

$$\rho_{\text{PCM}} \frac{\partial v}{\partial t} + \rho_{\text{PCM}} \left(\vec{U} \cdot \nabla v \right) = -\frac{\partial p}{\partial z} + \mu_{\text{PCM}} \nabla^2 v + \rho_{\text{PCM}}\, g\, \beta (T - T_{\text{m1}}) - \frac{\left(1 - f_1\right)^2}{\left(f_1^3 + f_1\right)} A_{\text{mushy}} v \tag{8-6}$$

where ρ_{PCM} is the PCM density; u and v are the velocities in r and z directions, respectively; p is the pressure; μ_{PCM} is the PCM viscosity; g is the gravitational acceleration; β is PCM thermal expansion coefficient; T is the temperature; T_{ml} is the lower limit of PCM melting point; f_{l} is the melting fraction in each cell; ω is a small number (0.001) to prevent division by zero; A_{mushy} is the mushy zone constant (10^5) [21]. $\rho_{\text{PCM}}\, g\, \beta (T - T_{\text{m1}})$ represents the Boussinesq approximation for including the buoyancy effect. The last term in momentum equations is the damping term [21]. The melting fraction f_{l} quantifies the percentage of liquid PCM in the mushy zone and is evaluated as [51]:

$$f_1 = \frac{T - T_{\text{m1}}}{T_{\text{mu}} - T_{\text{ml}}} = \begin{cases} 0 & \text{for } T < T_{\text{m1}} \\ 0 - 1 & \text{for } T_{\text{m1}} \le T \le T_{\text{mu}} \\ 1 & \text{for } T > T_{\text{mu}} \end{cases} \tag{8-7}$$

where T_{mu} is the upper limit of PCM melting point.

Momentum equations for the case with ceramic foam are given by [80]:

$$\frac{\rho_{\mathrm{PCM}}}{\varepsilon}\frac{\partial u}{\partial t}+\frac{\rho_{\mathrm{PCM}}}{\varepsilon^2}\left(\vec{U}\cdot\nabla u\right)=-\frac{\partial p}{\partial r}-\frac{\mu_{\mathrm{PCM}}}{K}u-\frac{\rho_{\mathrm{PCM}}F_l}{\sqrt{K}}|u|u+\frac{\mu_{\mathrm{PCM}}}{\varepsilon}\nabla^2 u-\frac{\left(1-f_l\right)^2}{\left(f_l^3+f_l\right)}A_{\mathrm{mushy}}u \quad (8\text{-}8)$$

$$\frac{\rho_{\mathrm{PCM}}}{\varepsilon}\frac{\partial v}{\partial t}+\frac{\rho_{\mathrm{PCM}}}{\varepsilon^2}\left(\vec{U}\cdot\nabla v\right)=-\frac{\partial p}{\partial z}-\frac{\mu_{\mathrm{PCM}}}{K}v-\frac{\rho_{\mathrm{PCM}}F_l}{\sqrt{K}}|v|v+\frac{\mu_{\mathrm{PCM}}}{\varepsilon}\nabla^2 v+\rho_{\mathrm{PCM}}\,g\,\beta(T-T_{\mathrm{ml}})$$

$$-\frac{\left(1-f_l\right)^2}{\left(f_l^3+f_l\right)}A_{\mathrm{mushy}}v \quad (8\text{-}9)$$

where ε is the porosity; K is the permeability; F_l is the inertia coefficient. The second term on the right side of momentum equations accounts for the Darcy effect; the third term explains the Forchheimer-extended Darcy effect [11]. The correlations for calculating permeability K and inertial coefficient F_l are the same as those in Chapter 6 and are listed in Table 8.4.

Table 8.4: Correlations used in the numerical model.

Inertia coefficient (F_l) [21]	$F_l = 0.00212(1-\varepsilon)^{-0.132}\left(d_{\mathrm{fs}}/d_{\mathrm{fp}}\right)^{-1.63}$ $d_{\mathrm{fp}} = \frac{25.4\times 10^{-3}}{\mathrm{PPI}}$ $d_{\mathrm{fs}} = 1.18\sqrt{\frac{1-\varepsilon}{3\pi}}\left[\frac{1}{1-e^{(\varepsilon-1)/0.04}}\right]d_{\mathrm{fp}}$
Permeability (K) [21]	$K=\frac{\varepsilon^2\left(d_{\mathrm{fp}}\sqrt{\kappa_{\mathrm{tor}}/3\varepsilon}\right)^2}{36(\kappa_{\mathrm{tor}}-1)\kappa_{\mathrm{tor}}}$ $\frac{1}{\kappa_{\mathrm{tor}}}=\frac{3}{4\varepsilon}+\frac{\sqrt{9-8\varepsilon}}{2\varepsilon}\cos\left\{\frac{4\pi}{3}+\frac{1}{3}\cos^{-1}\left[\frac{8\varepsilon^2-36\varepsilon+27}{(9-8\varepsilon)^{1.5}}\right]\right\}$
Effective thermal conductivity (k_{ef}) [143]	$k_{\mathrm{ef}} = k_{\mathrm{ef,\,ps}} + k_{\mathrm{ef,\,PCM}}$ $k_{\mathrm{ef,\,ps}} = \frac{1-\varepsilon}{3}k_{\mathrm{ps}}$ $k_{\mathrm{ef,\,PCM}} = \frac{2+\varepsilon}{3}k_{\mathrm{PCM}}$

The energy equation for the case without ceramic foam is given by [51]:

$$\rho_{\mathrm{PCM}}\, c_{\mathrm{p,\,PCM}} \left(\frac{\partial T}{\partial t} + \vec{U}\cdot\nabla T\right) = k_{\mathrm{PCM}}\nabla^2 T - \rho_{\mathrm{PCM}} L \frac{d\varphi}{dt} \tag{8-10}$$

The energy equation for the case with ceramic foam is [90]:

$$\left[(1-\varepsilon)\rho_{\mathrm{ps}} c_{\mathrm{p,\,ps}} + \varepsilon\, \rho_{\mathrm{PCM}}\, c_{\mathrm{p,\,PCM}}\right] \frac{\partial T}{\partial t} + \rho_{\mathrm{PCM}}\, c_{\mathrm{p,\,PCM}} \left(\vec{U}\cdot\nabla T\right) = k_{\mathrm{ef}}\nabla^2 T - \varepsilon \rho_{\mathrm{PCM}} L \frac{d\varphi}{dt} \tag{8-11}$$

where $c_{\mathrm{p,\,PCM}}$ and $c_{\mathrm{p,\,ps}}$ are the specific heat of PCM and porous skeleton respectively; k_{PCM} is the thermal conductivity of PCM; L is the latent heat; ρ_{ps} is the density of porous skeleton; k_{ef} is the effective thermal conductivity, which is computed using correlations in Table 8.4.

For the HTF, forced convection occurs and the governing equations are:

Continuity equation [149]:

$$\nabla \cdot \vec{u} = 0 \tag{8-12}$$

Momentum equation [149]:

$$\rho_{\mathrm{HTF}} \frac{\partial \vec{u}}{\partial t} + \rho_{\mathrm{HTF}} (\vec{u} \cdot \nabla)\vec{u} = -\nabla p + \mu_{\mathrm{HTF}} \nabla^2 \vec{u} \tag{8-13}$$

Energy equation [149]:

$$\rho_{\mathrm{HTF}}\, c_{\mathrm{p,\,HTF}} \frac{\partial T}{\partial t} + \rho_{\mathrm{HTF}}\, c_{\mathrm{p,\,HTF}}\, \vec{u} \cdot \nabla T = \nabla \cdot (k_{\mathrm{HTF}} \nabla T) \tag{8-14}$$

where ρ_{HTF}, μ_{HTF}, $c_{\mathrm{p,\,HTF}}$ and k_{HTF} are density, viscosity, thermal conductivity and specific heat of HTF respectively.

8.2.5 Initial and boundary conditions

The working hour of the TES subsystem is 6:00 – 20:00. The initial temperature of the entire unit is set as the minimum driving temperature of ORC ($T_{\mathrm{min,\,ORC}}$, 125 °C [166]):

$$T = T_{\mathrm{min,\,ORC}} \tag{8-15}$$

Other initial conditions are:

$$u = v = 0 \tag{8-16}$$

The HTF inlet temperature to the unit equals the outlet temperature from the solar field:

$$T_{\text{in, HTF}} = T_{\text{solar, outlet}} \tag{8-17}$$

HTF flows into the unit with the mass flow rate of 1.4×10^{-3} kg/s. The outlet boundary is set as Outflow to ensure the mass conservation. The outer wall of the entire unit except the HTF domain are set as adiabatic.

At the interface between the tube and HTF:

$$T_{\text{HTF}} = T_{\text{tube}},\ (-k_{\text{HTF}}\ \nabla T_{\text{HTF}})\cdot\boldsymbol{n} = (-k_{\text{tube}}\ \nabla T_{\text{tube}})\cdot\boldsymbol{n},\ \ u = v = 0 \tag{8-18}$$

At the interface between the tube and PCM:

$$T_{\text{PCM}} = T_{\text{tube}}, (-k_{\text{PCM}}\ \nabla T_{\text{PCM}})\cdot\boldsymbol{n} = (-k_{\text{tube}}\ \nabla T_{\text{tube}})\cdot\boldsymbol{n},\ \ u = v = 0 \tag{8-19}$$

8.2.6 Numerical procedure

ANSYS Fluent 18.0 package was employed to solve the above thermal transport problem. The governing equations were discretized using the finite volume method (FVM). The SIMPLE scheme was utilised to couple pressure and velocity. The second-order upwind method was implemented to discretise pressure, momentum and energy terms. The under-relaxation factors were set as 0.3, 1, 1, 0.7, 0.9 and 1 for pressure, density, body forces, momentum, liquid fraction update and energy respectively. The convergence criteria for conservation equations of mass, momentum and energy were 10^{-4}, 10^{-4} and 10^{-6} respectively.

Several mesh sets (18, 118 cells, 28, 491 cells and 36, 898 cells) and time steps (0.5 s, 1 s and 2 s) were tested to balance the computational accuracy and time. $T_{\text{in, HTF}}$ is set as constant 400 °C. First, under the fixed time step of 1 s, three mesh sets were tested. The variation of melting fraction with time is presented in Figure 8.5. It is seen from Figure 8.5(a) that the grid size has an insignificant effect on the melting fraction. The medium mesh set with 28, 491 cells is chosen. Then, under the fixed mesh of 28, 491 cells, three time step sets were tested. It is found from Figure 8.5(b) that although there is some deviation in the melting fraction, the difference in the total melting time is within 2 s. The time step of 1 s is adopted.

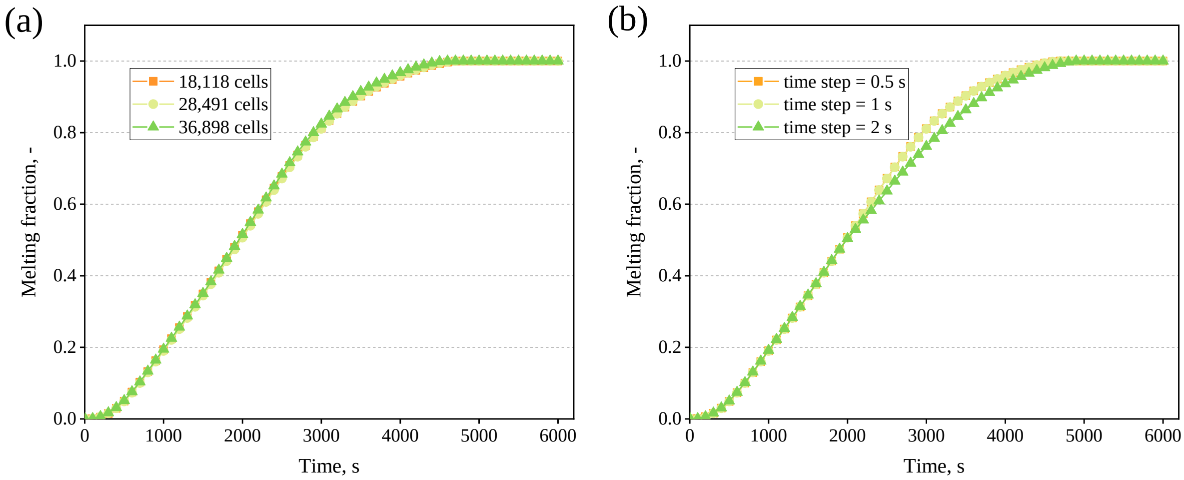

Figure 8.5: (a) Grid independence test; (b) time step independence test.

8.3 Model validation

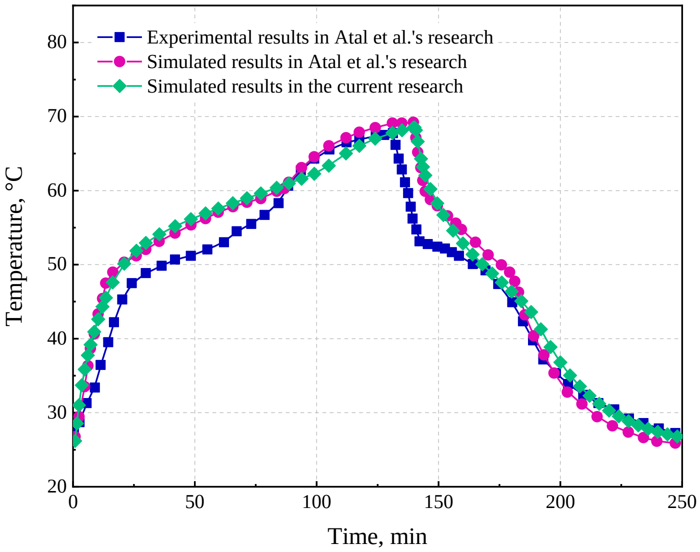

Figure 8.6: Comparison between Atal et al. [47]'s experimental/numerical results with the predicted results.

Atal et al. [47] carried out experimental and numerical studies on the charging/discharging process of paraffin/aluminium foam in a shell-and-tube unit. Material properties are listed in **Table 5**. In their experiment, the shell-and-tube unit was placed horizontally. The unit is made of aluminium and insulated by commercial fibreglass. The outer tube is 12 inches long with an outer diameter of 2 inches. The inner tube is 30 inches long with an outer diameter of 0.5 inch. The inner tube is longer than the outer tube so that a uniform flow can be developed. Heat storage material was placed in the annular space between the outer tube and the inner tube. During the charging process, 70 °C air passed through the inner tube. Heat storage material was melting until a steady state was reached. Then, 25 °C air was pumped into the inner tube, starting the discharging process.

Table 8.5: Thermo-physical properties of PCM and porous skeleton [47].

Property	Paraffin	Aluminum foam
Density, kg/m^3	730 - 790	140.4
Melting point, °C	50 - 60	-
Latent heat, J/kg	117, 000	-
Specific heat, J/(kg·K)	2510	896
Thermal conductivity, W/(m·K)	0.25	167
Porosity, -	-	0.95

The temperature variation at a point was recorded and shown in **Figure 6**. Atal et al. also performed a 2D simulation and the numerical results are presented in Figure 6. The temperature evolution is predicted by the current model and the results are compared with Atal et al.'s experimental and numerical results. It is seen from Figure 6 that the variation trend of predicted results agrees well with that of experimental results. At about 0 – 25 min, the temperature rises rapidly and the storage material is in a solid state. At about 25 – 70 min, the experimental temperature rises slowly, for the reason that the absorbed heat is mostly used for solid-liquid phase change. At these two stages, the predicted results as well as Atal et al.'s numerical results are larger than the experimental values, and the deviation becomes greater as the melting proceeds. The deviation should be attributed to the difficulty in establishing the absolutely adiabatic boundary for the experiment. After 70 min, the temperature difference between HTF and storage material is small, however, the experimental temperature rises rapidly. This may be caused by the specific heat of the storage material: the specific heat of the liquid storage material is lower than that of the solid counterpart [21], so even though the storage material absorbs less heat, its temperature still rises rapidly. However, in the current simulation as well as Atal et al.'s simulation, the specific heat of the storage material is set as constant. After the complete melting, since the temperature difference between HTF and the storage material becomes small, the simulated temperature rises slowly. As a result, the deviation between the numerical results and the experimental results gets smaller and even the latter is larger than the former. At about 125 min, the predicted result is almost the same as the experimental counterpart, which might be attributed to the balance between the heat loss and the specific heat. The maximum deviation between the experimental and predicted results occurs at 141 min when the discharging begins in the simulation. After that, the deviation becomes smaller remarkably and at the end of discharging, the predicted results are almost the same as the experimental values. And the maximum deviation between the predicted results and Atal et al. [47]'s numerical results is about 4%. Thus, the current model is reliable.

8.4 Results and discussions

8.4.1 Melting and energy storage

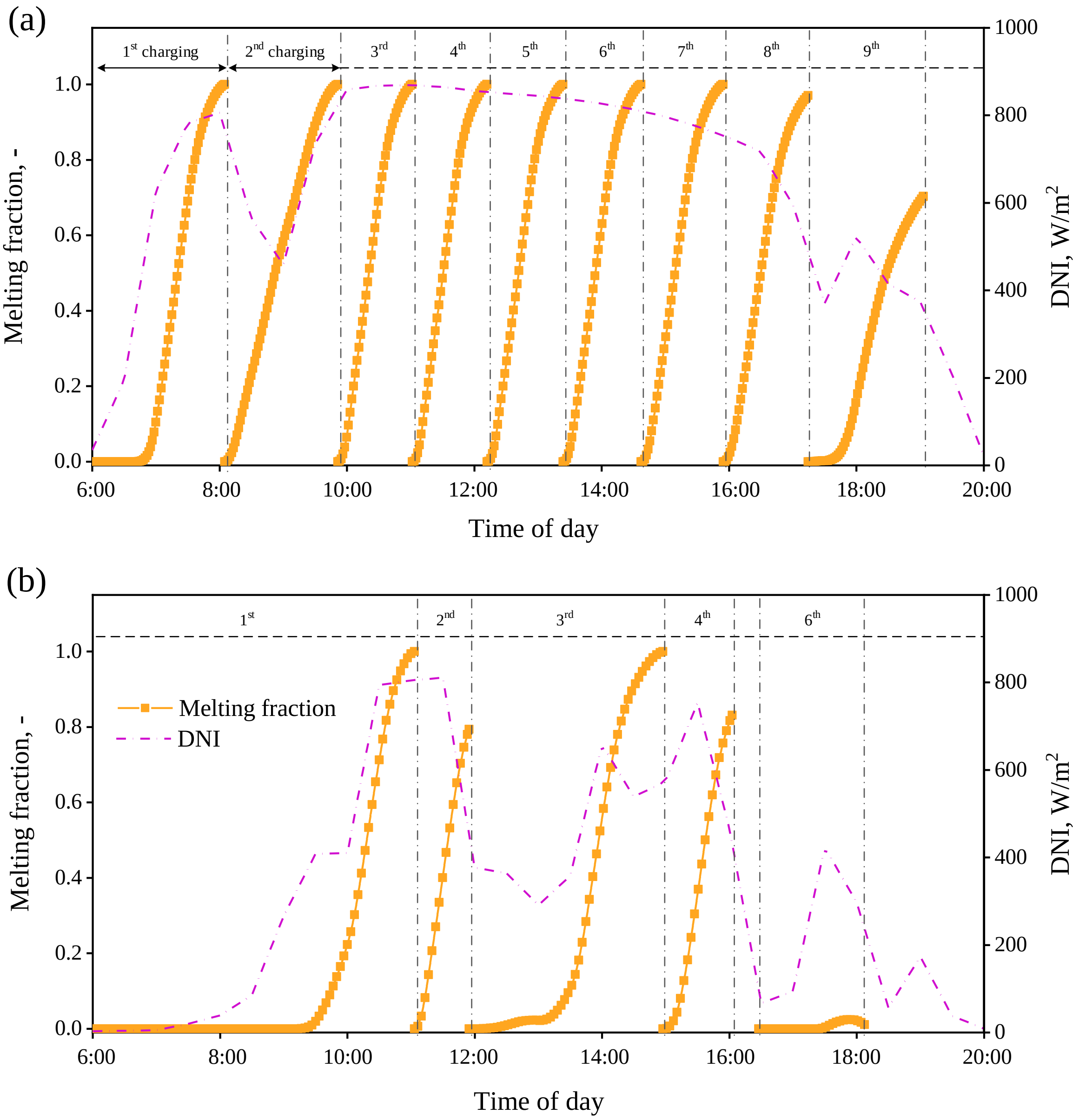

Figure 8.7: Variation of melting fraction in each charging on (a) sunny day and (b) cloudy day.

Figure 8.7 shows the variation of melting fraction in each charging over the whole working day (6:00 – 20:00). On a sunny day, the first 7 charging is complete (melting fraction $f_l = 1$) while the 8th and 9th charging is incomplete ($f_l = 0.97$ and 0.70). After the 9th charging, no PCM melts because the solar radiation is very weak. During the 1st charging, DNI starts from a low level and gradually increases to a high level. During the 2nd charging, DNI falls to a low value and then increases. This explains the slow melting rate of PCM in the 1st and 2nd charging, as shown in Figure 8.8(a). In contrast, during the 3rd, 4th, 5th, 6th and 7th charging, DNI remains at a high level and the melting rate of PCM is fast. However, their melting rates are a bit different and the variation is the same as the change in DNI: from the 3rd charging to the 7th charging, DNI gradually decreases, and the melting rate decreases. After the 7th charging, DNI decreases greatly. As a result, HTF cannot be heated fully and PCM cannot be melted completely in the 8th and 9th charging.

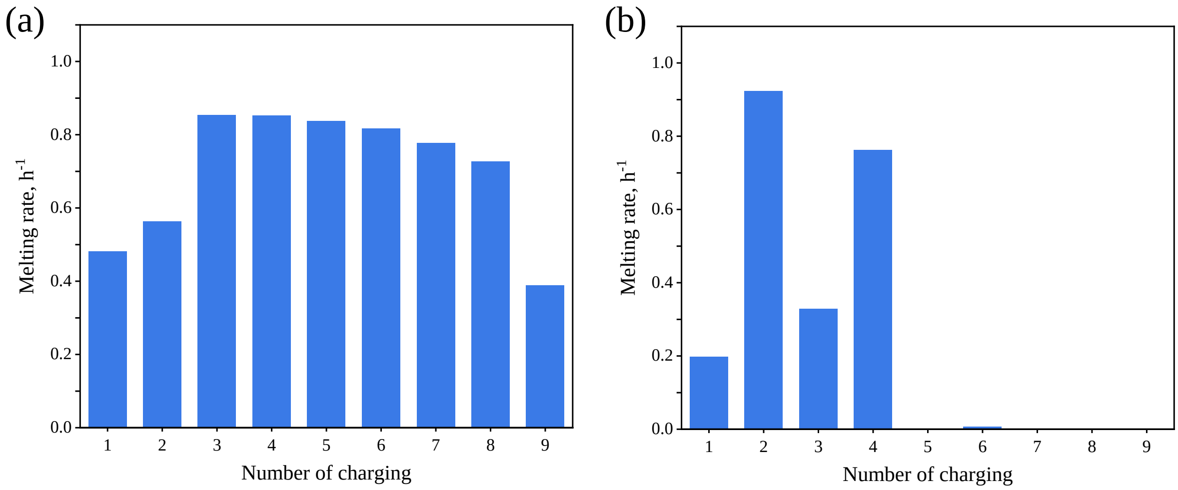

Figure 8.8: Melting rate of PCM in each charging on (a) sunny day and (b) cloudy day.

It is seen from Figure 8.7 that the number of charging on a cloudy day decreases and only two charging are full (the 1st and 3rd charging). Moreover, the melting rate of the full charging cases is slower than that on a sunny day (Figure 8.8). These should be attributed to the weaker solar radiation on a cloudy day. Moreover, DNI on a cloudy day is more fluctuating than that on a sunny day. As a consequence, the difference between the melting fraction curves on a cloudy day is more remarkable (Figure 8.7).

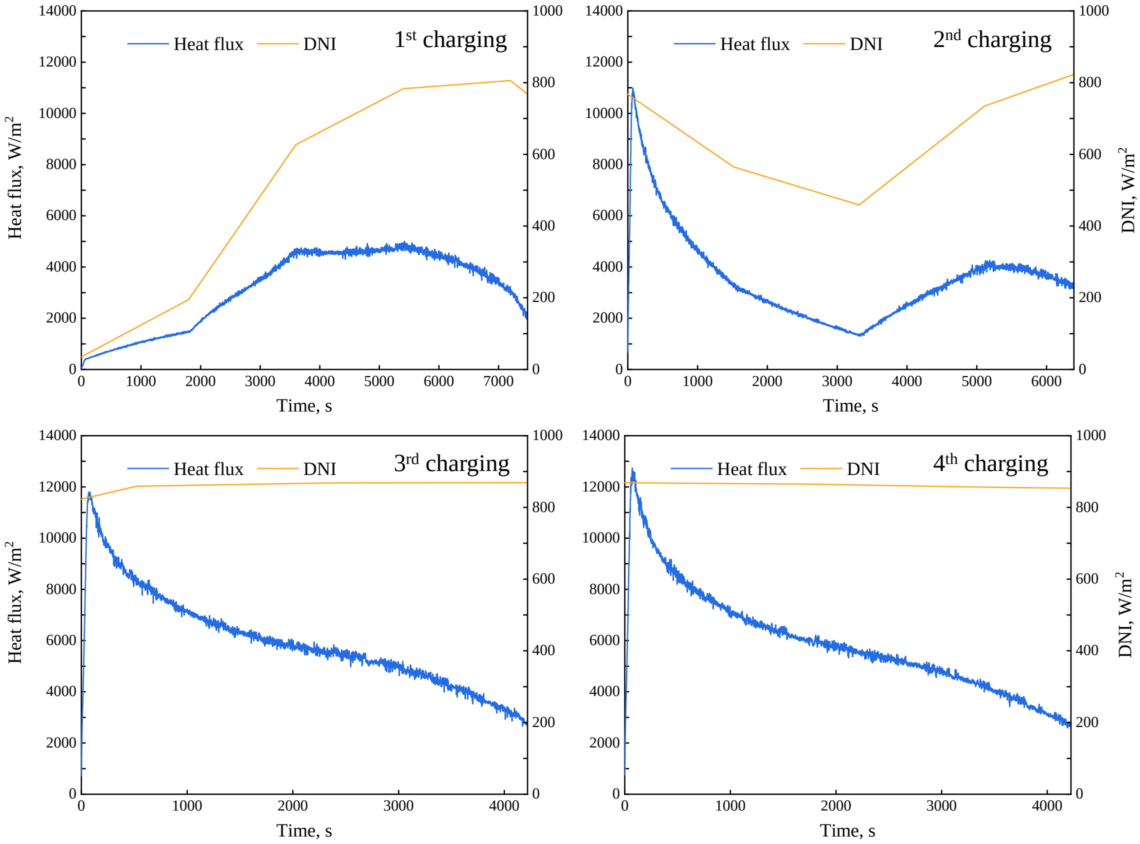

Figure 8.9: Variation of heat flux in different charging on a sunny day.

The evolution of the melting fraction is related to the heat flux transferred from HTF to PCM. The heat flux in the 1st, 2nd, 3rd and 4th charging on a sunny day is shown in Figure 8.9. The general trend of the four heat flux curves is that: heat flux first increases (because of the large temperature difference between HTF and PCM) and then decreases (owing to the rise of the average PCM temperature). The heat flux in the 2nd charging has additional specific characteristics (a valley at about 3300 s) corresponding to the variation of DNI. For the 2nd, 3rd and 4th charging, the heat flux rises to the peak sharply, so the melting fraction gets greater than zero very quickly, as Figure 8.7(a) shows. By contrast, the heat flux in the 1st charging rises very slowly at the initial stage, as a result, the melting fraction remains at zero for a quite long time.

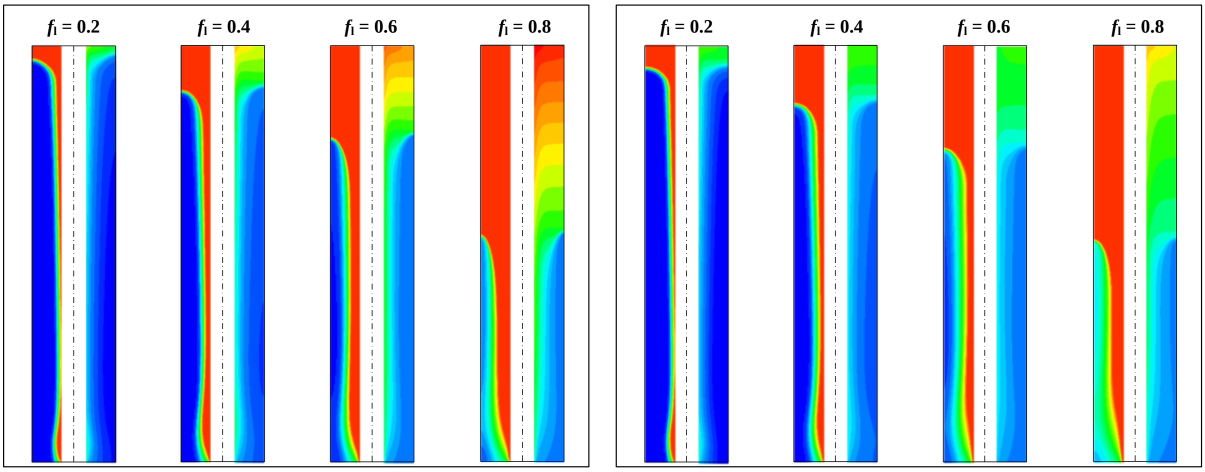

(a) 1st charging (b) 2nd charging

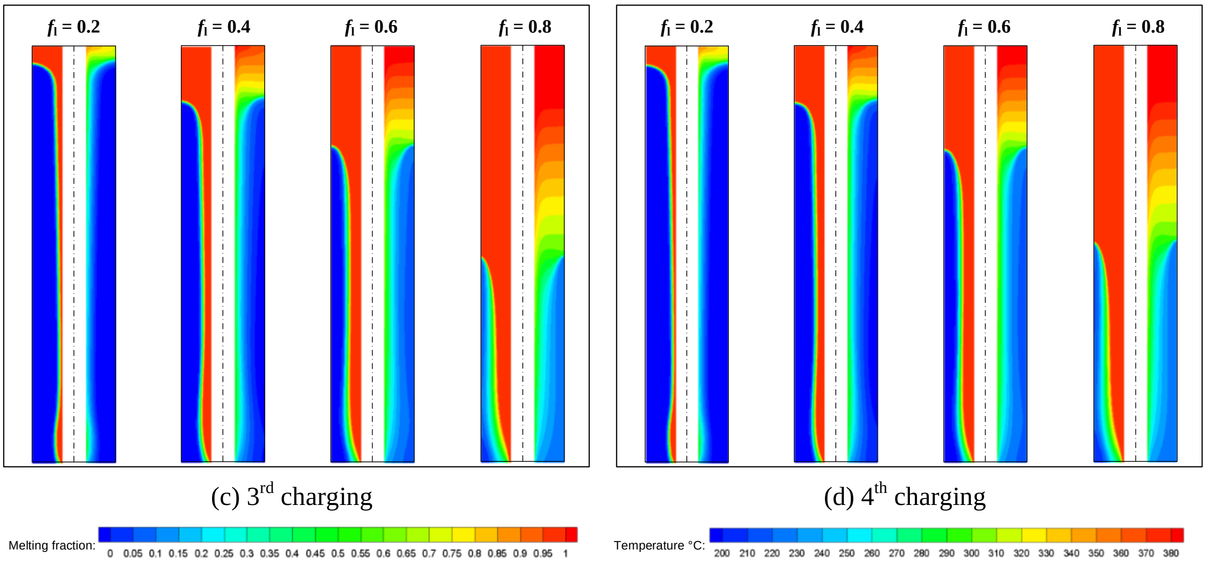

(c) 3rd charging (d) 4th charging

Figure 8.10: Solid-liquid phase interface (left half) and temperature field (right half) of PCM in different charging on a sunny day.

To further illustrate the effect of solar fluctuation, the solid-liquid phase interphase and temperature contour of PCM at different melting fraction (f_l) in the 1st, 2nd, 3rd and 4th charging are presented in Figure 8.10. In each small figure, the left half is the solid-liquid interface while the right half is the temperature contour. It can be found that the solid-liquid interface has little difference among different charging at $f_l = 0.2$. The case is the same for $f_l = 0.4$. However, at $f_l = 0.6$ and 0.8, the mushy region in the 2nd charging is obviously larger than that in the other three charging. Taking $f_l = 0.8$ as an example, the DNI in the 2nd charging is 649 W/m^2, lower than 788 W/m^2 in the 1st charging, 868 W/m^2 in the 3rd charging and 860 W/m^2 in the 4th charging. This weak solar radiation results in low-temperature HTF and heat is transferred from liquid PCM to solid PCM gradually and slowly, forming a large mushy region. Overall, solar fluctuation has a very limited effect on the solid-liquid interface. But it has a remarkable influence on the temperature distribution. As Figure 8.10 shows, at $f_l = 0.2$, from the 1st charging to the 4th charging, the temperature field in the upper portion is increased. At $f_l = 0.4$, the temperature field in the upper portion in the 3rd/4th charging is the highest while that in the 1st charging develops greatly. At the same time, the minimum temperature of PCM in the 3rd/4th charging is lower than that in the 1st and 2nd charging. At $f_l = 0.6$ and $f_l = 0.8$, the temperature field in the upper portion in the 3rd/4th charging remains the highest, while that in the 2nd charging is the lowest.

To demonstrate the difference in temperature distribution clearly, the average PCM temperature, maximum temperature, minimum temperature and temperature non-uniformity index in the four charging are plotted in Figure 8.11. The temperature non-uniformity index is defined as:

$$\delta\,(f_l) = \sqrt{\frac{\sum_{i=0}^{n}\left[T_i(r,z,f_l) - \overline{T\,(f_l)}\,\right]^2}{n}} \tag{8-20}$$

where $T_i(r,z,f_l)$ and $\overline{T(f_l)}$ are the transient temperature at (r, z) and the average temperature of PCM at the melting fraction f_l.

At the initial melting stage ($f_l = 0.2$), DNI in the 3rd/4th charging is largest and HTF can be heated to a high temperature, so the maximum temperature of PCM is highest (Figure 8.11(b)). However, the heating time in the 3rd/4th charging is limited and some PCM cannot be heated fully, leading to the lower minimum temperature (Figure 8.11(c)). The condition is similar at $f_l = 0.4$, 0.6 and 0.8.

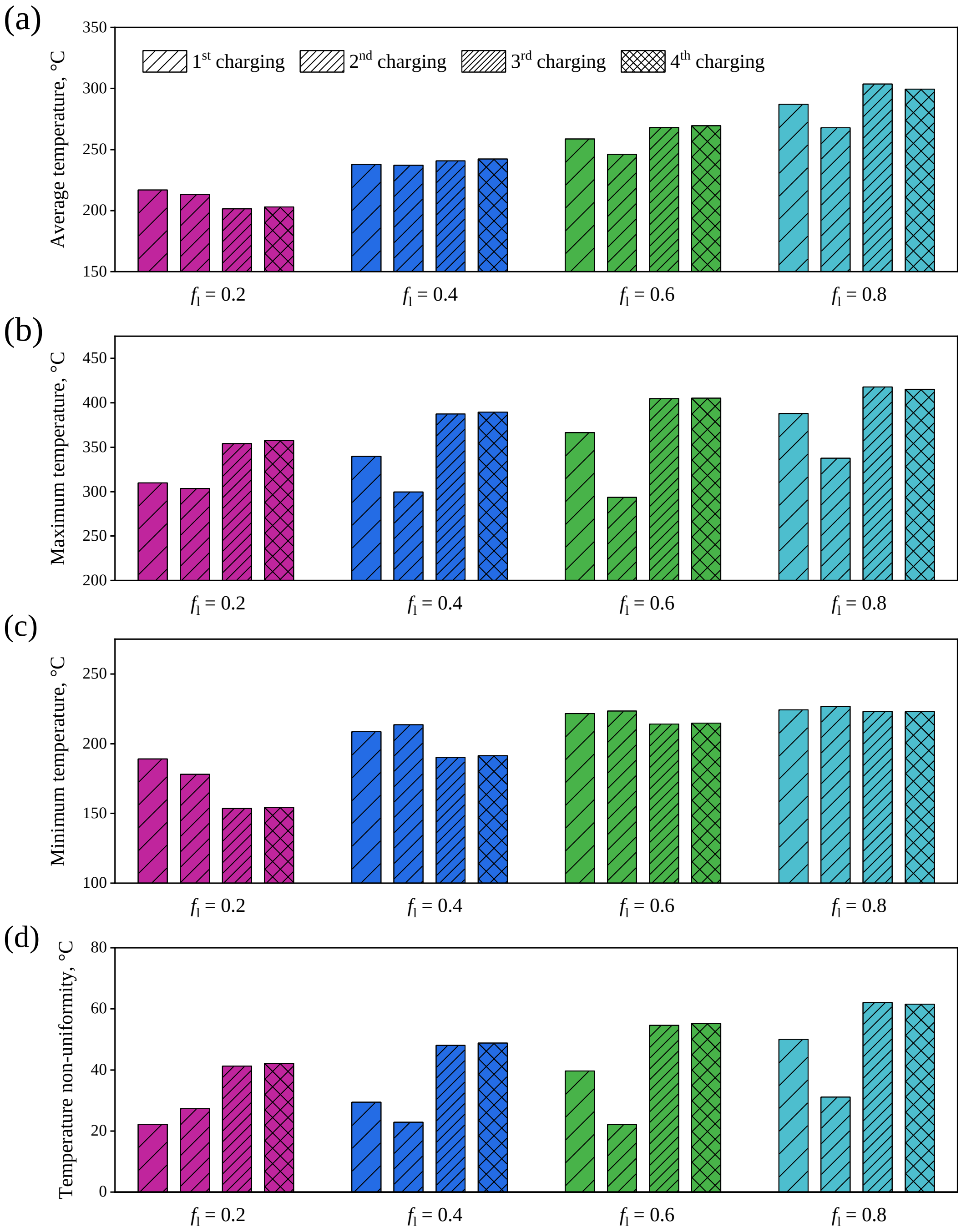

Figure 8.11: Comparison of (a) average temperature, (b) maximum temperature, (c) minimum temperature and (d) temperature non-uniformity index of PCM in different charging on a sunny day.

The maximum temperature in the 2nd charging is always the lowest among the four charging because its DNI is the smallest. In turn, the minimum temperature is the highest except for $f_l = 0.2$. The initial DNI in the 1st charging is low and the heating time is long, which should explain the highest minimum temperature at $f_l = 0.2$. The variation of the temperature difference between the maximum temperature and the minimum temperature is generally consistent with the variation of the temperature non-uniformity index.

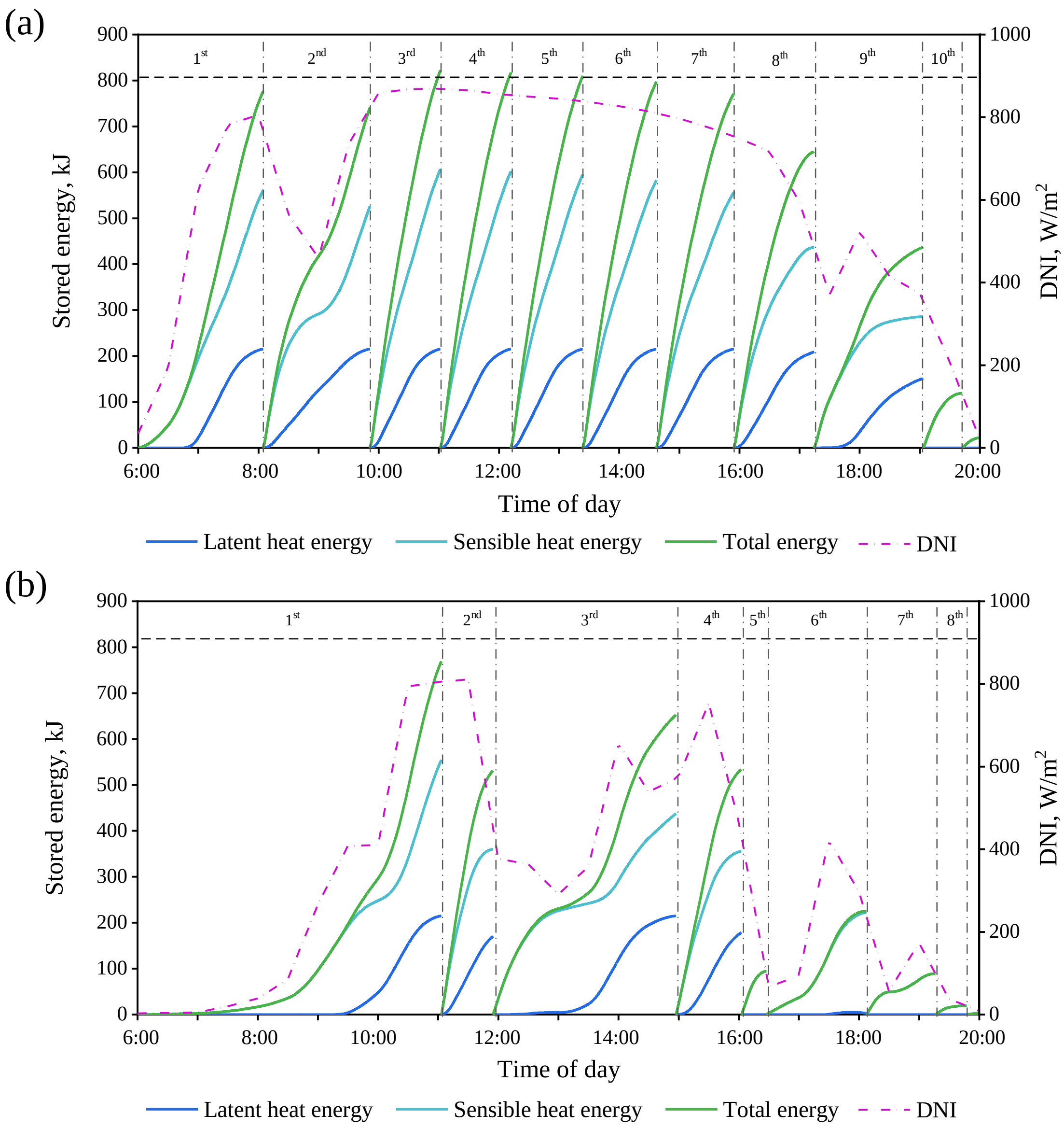

Figure 8.12: Stored latent heat energy, sensible heat energy and total energy in each charging on (a) sunny day and (b) cloudy day.

Although the melting fraction of the four charging is the same, the average temperature of PCM is different. As Figure 8.11(a) shows, at $f_\mathrm{l} = 0.2$, the 3rd/4th charging has the lowest average temperature, however, as the melting develops, their average temperature becomes the highest. The melting fraction is related to latent heat energy while the temperature is related to sensible heat energy. The different temperature distribution among the four charging will lead to different sensible heat energy storage, which will be discussed following.

Figure 8.12 presents the stored latent heat energy, sensible heat energy and total energy in each charging during the whole working hours. On a sunny day, the first 7 charging is full (melting fraction $f_l = 1$), however, the total stored energy is different. The 3rd charging stores the most energy (822.7 kJ) while the 2nd charging stores the least energy (741.6 kJ). The former is 10.9% higher than the latter. Since PCM is fully melted in the first 7 charging, the difference in the total stored energy should be attributed to the sensible heat energy. Sensible heat energy is related to the temperature distribution. As shown in Figure 8.11(a), the average temperature in the 3rd charging at $f_l = 0.8$ is highest, leading to largest sensible energy storage. On a cloudy day, the difference in total stored energy is more remarkable. The total stored energy in the 1st charging is 769.7 kJ while that in the 3rd charging is 652.9 kJ, the former is 17.9% higher than the latter.

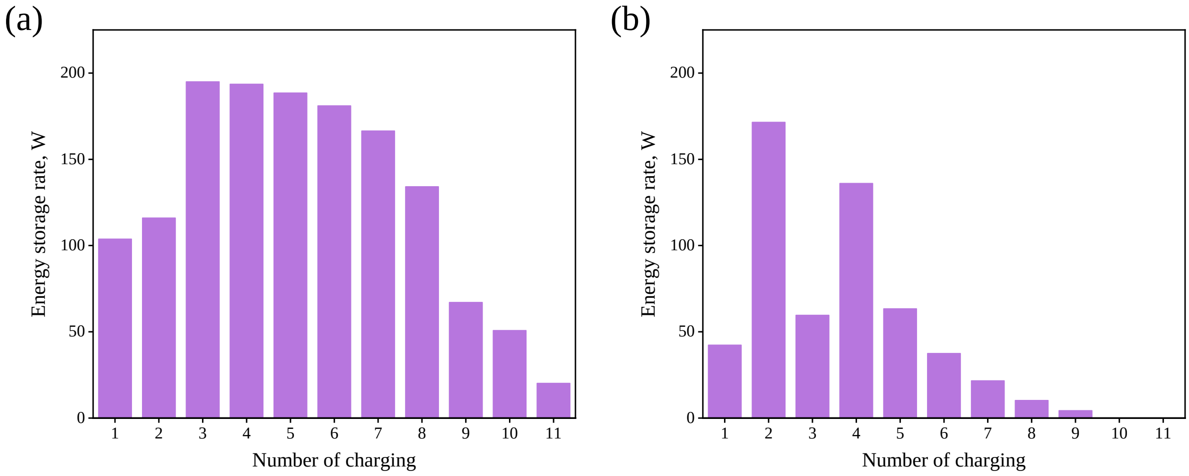

Figure 8.13: Energy storage rate of each charging on (a) sunny day and (b) cloudy day.

It is found from Figure 8.12(a) that when DNI is high, the total stored energy is high. This is because HTF can be heated to a high temperature so the temperature of PCM at the inlet of the shell-and-tube unit is higher, as observed in Figure 8.10 (c) and (d) at $f_l = 0.8$; when the melting is completed, the overall average temperature is higher, resulting in the larger sensible heat storage. The high DNI not only improves the total stored energy but accelerates the energy storage rate. As Figure 8.13(a) shows, the energy storage rate in the 3rd/4th charging is also the highest.

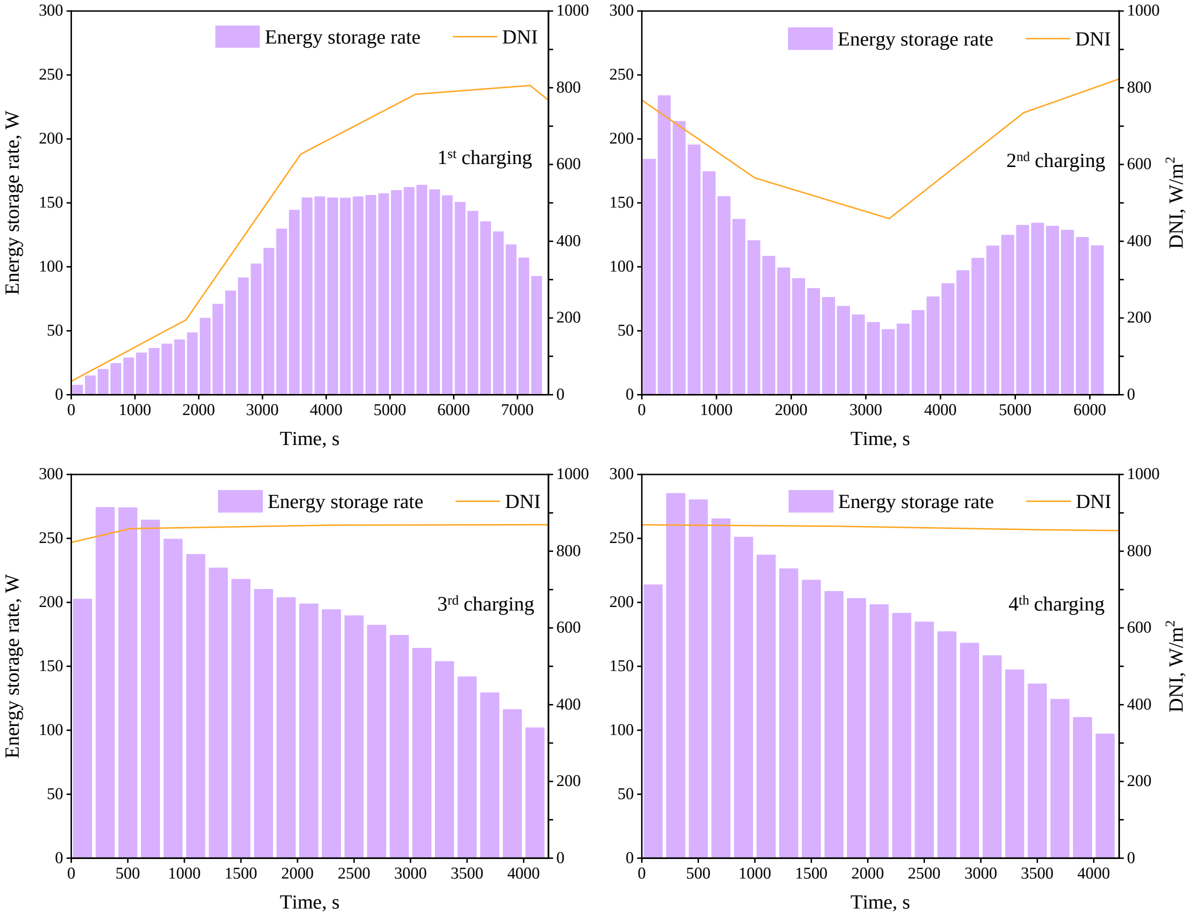

Figure 8.14: Variation of energy storage rate in different charging on a sunny day.

The rising DNI can also cause large total stored energy, i.e. the 1st charging on a sunny day. This can be explained as follows: the initial DNI is low, but it mainly affects the early energy storage process; the total stored energy is mostly influenced by the late (or final) DNI. However, the energy storage rate under this condition is low, as seen in Figure 8.13(a).

The oscillating DNI (the 2nd charging) leads to the least total stored energy but the energy storage rate is higher than that under the rising DNI. The effect of the rising DNI and the oscillating DNI on total stored energy and energy storage rate is further confirmed by results of the 1st and 3rd charging ($f_1 = 1$) on a cloudy day (Figure 8.12(b) and Figure 8.13(b)).

The falling DNI such as in the 8th and 10th charging on a sunny day and the 5th charging on a cloudy day causes small total stored energy, not only because of the weak solar radiation in the late energy storage process but the overall weak solar radiation.

The detailed (200s-averaged) energy storage rate is presented in Figure 8.14. The general trend is first rising and then falling, which is similar to the variation of heat flux. It is noted that the time when the maximum energy storage rate occurs is not consistent with the time when the maximum DNI occurs. For the 2nd, 3rd and 4th charging, the maximum energy storage rate occurs at the initial stage, which should be attributed to the large temperature difference between HTF and PCM.

8.4.2 Assessment of ceramic foam

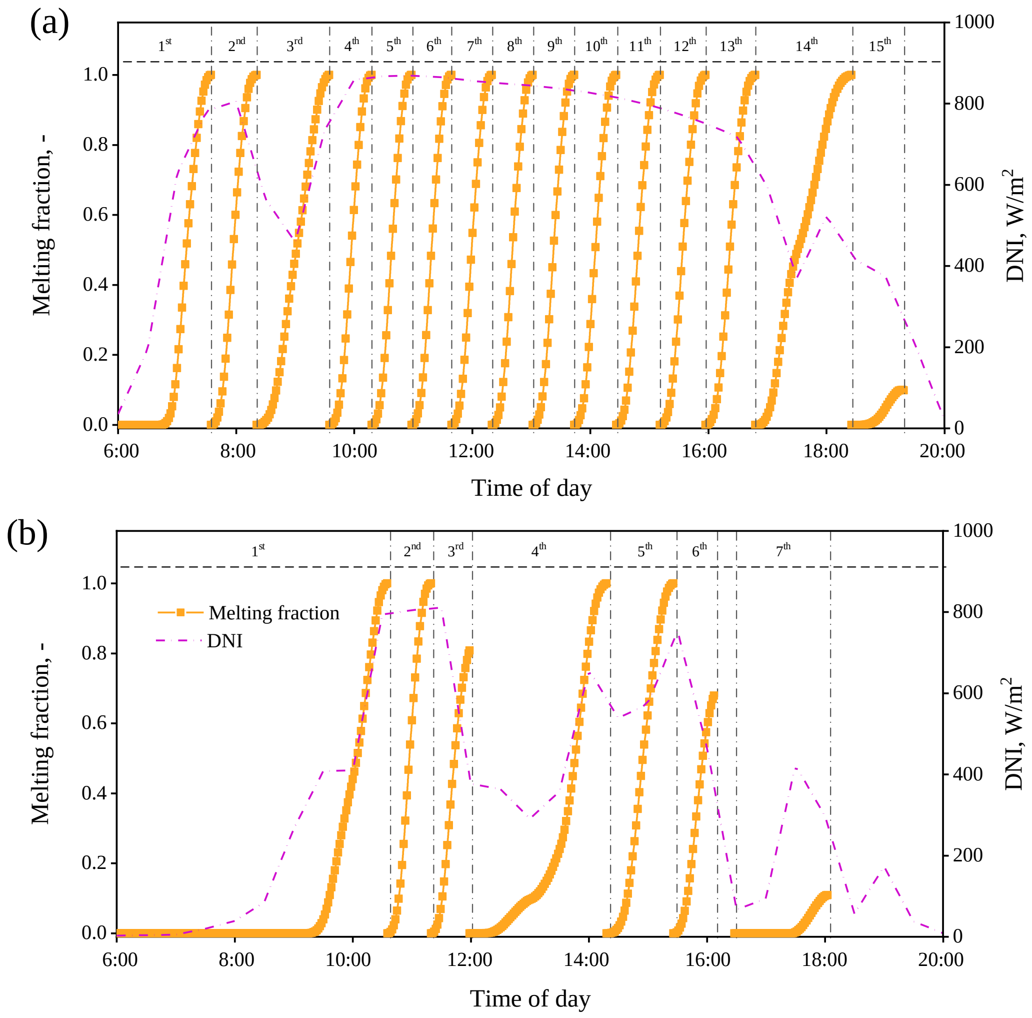

Figure 8.15: Melting fraction of PCM with ceramic foam enhancement on (a) sunny day and (b) cloudy day.

The energy storage characteristics of pure salt were analysed in the above subsection. However, the thermal conductivity of pure salt is low. In this subsection, the use of ceramic foam to enhance the heat transfer was discussed. The melting fraction of salt with ceramic foam enhancement under solar fluctuation is plotted in Figure 8.15. The number of full charging (f_l = 1) on a sunny day and on a cloudy day is 14 and 4 respectively, both doubles that of using pure salt.

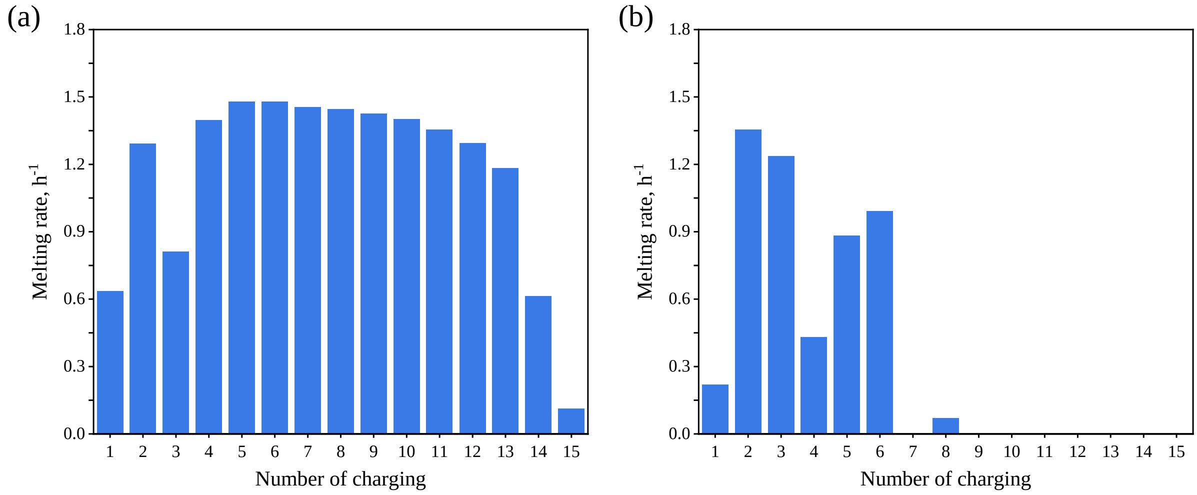

Figure 8.16: Melting rate of PCM with ceramic foam enhancement on (a) sunny day and (b) cloudy day.

The melting rate is also improved. As seen in Figure 8.16, on a sunny day, the maximum melting rate is 1.26 h^{-1}, while that of using pure salt is 0.85 h^{-1}; on a cloudy day, the maximum melting rate is 1.15 h^{-1}, while that of using pure salt is 0.76 h^{-1}. This is related to the increased thermal conductivity. The effective thermal conductivity of ceramic foam-enhanced salt is 1.60 W/(m·K), much larger than that of pure salt (0.59 W/(m·K)). The standard deviation in the melting rate (>0) is listed in Table 8.6. It is found that the standard deviation of cases with enhancement is higher, both on a sunny day and on a cloudy day, suggesting ceramic foam-enhanced PCM is more sensitive to solar fluctuation. This is because after adding ceramic foam to the salt, the melting time is shortened and thus the fluctuating feature of solar radiation is exhibited more fully in each charging.

Table 8.6: Comparison of energy storage characteristics between PCM with/without ceramic foam enhancement.

		Total number of charging, -	Number of full charging, -	Total energy storage, kJ	*σ* of melting rate, h^{-1}	*σ* of energy storage rate, W
Without enhancement	Sunny day	11	7	6761	0.18	62.3
	Cloudy day	9	2	2918	0.39	57.1
With enhancement	Sunny day	17	14	9003	0.35	84.4
	Cloudy day	12	4	3767	0.43	75.8

*: *σ* is the standard deviation

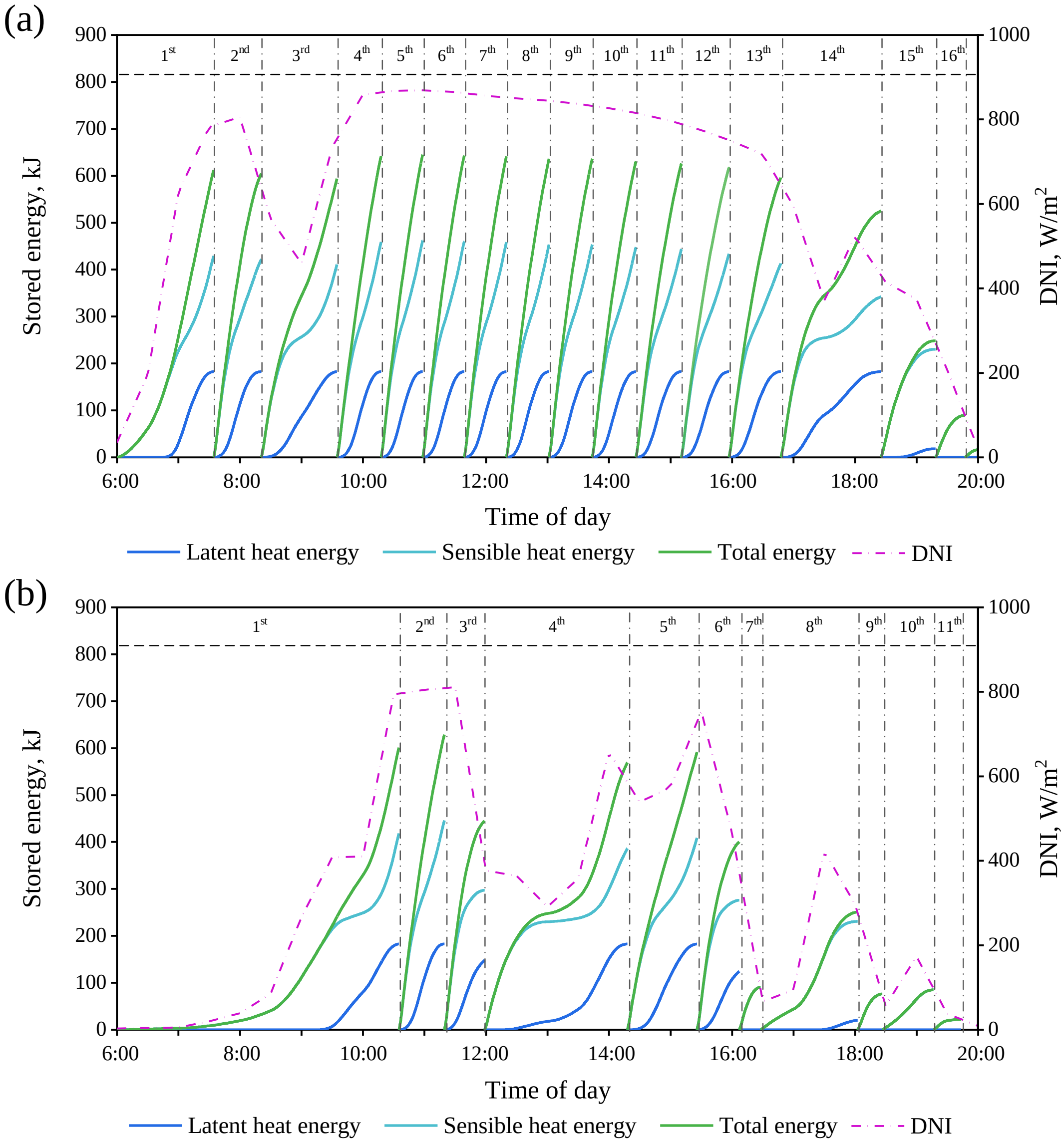

Figure 8.17: Latent heat energy storage, sensible heat energy storage and total energy storage of PCM with ceramic foam enhancement on (a) sunny day and (b) cloudy day.

Various energy storage parameters are plotted in Figure 8.17. The total number of charging is increased by 6 on a sunny day and 3 on a cloudy day respectively. However, the total stored energy in each full charging is reduced. Taking the 5th charging (the maximum total stored energy) as an example, the total stored energy is 645 kJ. For cases without enhancement, the total stored energy of the 3rd charging is the maximum, 823 kJ. This is mainly because after adding ceramic foam (porosity = 0.85) to the salt, the volume of salt is decreased and the latent heat energy is reduced. Nevertheless, the total energy storage over the whole working day is improved by 33.2% on a sunny day and 29.1% on a cloudy day respectively.

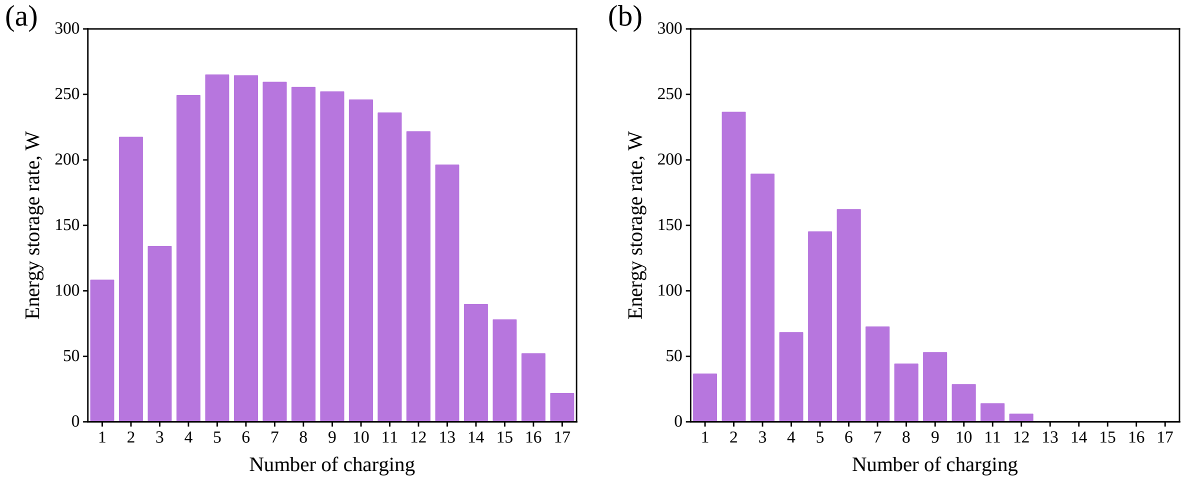

Figure 8.18: Energy storage rate of PCM with ceramic foam enhancement on (a) sunny day and (b) cloudy day.

The energy storage rate of ceramic foam-enhanced PCM is shown in Figure 8.18. Compared to cases without enhancement, the energy storage rate is improved. However, the improvement is different according to the time of day. At 6:00 on a sunny day, i.e. the 1st charging, the energy storage rate is only increased from 103.8 W to 108.1 W. At about 10:30 (the 5th charging of case with enhancement or the 3rd charging of case without enhancement), the DNI is highest and the energy storage rate is greatly increased from 195.0 W to 264.9 W. And the difference in energy storage rate under enhancement is more significant. As Table 8.6 shows, the standard deviation in the energy storage rate of ceramic foam-enhanced PCM is larger than that without enhancement, both on a sunny day and on a cloudy day. This also suggests that ceramic foam-enhanced PCM is more sensitive to solar fluctuation, consistent with the analysis of melting rate.

8.5 Summary

In this chapter, the thermal performance of phase change material under solar fluctuation was investigated. A sunny day and cloudy day in Nottingham, the UK were selected and the charging over the whole working hours (6:00-20:00) was analysed to understand the practical energy storage process. The following conclusions are drawn:

(1) Solar fluctuation has a very limited effect on the solid-liquid interface but has a remarkable influence on the temperature distribution. The variation of the maximum temperature, the minimum temperature and the temperature uniformity of PCM is generally consistent with the change in solar radiation.

(2) For the same full charging cases, the total stored energy is different according to solar fluctuation, with a maximum difference of 17.9%. Strong solar radiation not only improves the energy storage rate but also increases the total stored energy. Rising solar radiation can also cause large total stored energy while the energy storage rate is low. Oscillating solar radiation results in the least total stored energy among full charging cases, whilst the energy storage rate is higher than that under rising solar radiation. Falling solar radiation leads to small total stored energy.

(3) Ceramic foam-enhanced PCM is more sensitive to solar fluctuation. And the number of full charging doubles and the total stored energy over the whole working day is improved by 33.2% on a sunny day and 29.1% on a cloudy day respectively.

Chapter 9 - Conclusions and outlook

9.1 Conclusions

Inorganic salts are suitable medium- and high-temperature phase change materials but they have issues of low thermal conductivity and corrosivity, which makes conventional heat transfer enhancement methods fail. In the current research, the open-cell ceramic foam was used to enhance the heat transfer of salts. The following conclusions are drawn:

(1) Thermo-physical properties of binary nitrate salts ($NaNO_3$-KNO_3) with different component fractions were measured. Mixing pure salts decreases the melting point while would not impair the latent heat. The melting point of all eutectic salts is lower than that of pure salt, with a maximum decrease of over 100 °C, which is attributed to the low coulombic bonding energy from the molecular dynamics (MD) simulation.

(2) Open-cell ceramic foams with large pore sizes (~mm) were fabricated using the dipping method, and ceramic foam/salt porous CPCMs were prepared using the atmospheric impregnation method. The compatibility between prepared ceramic and salt was tested by conducting 50, 100, and 200 melting/solidification cycles. Various characterising technologies including scanning electron microscope (SEM), energy-dispersive spectroscopy (EDS), X-ray diffraction (XRD), and Raman were used to analyse the corrosion behaviours. The corrosion experiments of Cu and Al were also conducted to make a comparison. Experimental results indicate that the prepared ceramic has excellent corrosion-resistant performance. In addition, the reactive molecular dynamics simulation provides microscopic insights into corrosion behaviours from the possible physical dissolution, chemical reaction and thermal stress failure.

(3) The thermal transport in ceramic foam/salt CPCMs was investigated experimentally and numerically. The solid-liquid phase interface is curved greatly, indicating strong natural convection. The melting rate of CPCMs with pore density of 10 PPI (Pores Per Inch)is increased by 51.5%. The porosity has a more significant effect than pore density on the melting

performance. The total stored energy is slightly decreased in the current condition because the sensible heat stored by ceramic foam compensates for some of the lost latent heat. But the energy storage rate is improved remarkably. The average energy storage rate of CPCM with the porosity of 0.80 is increased by 73.2%. Compared to pure salt, the exergy of CPCMs rises faster, and the exergy efficiency of all CPCMs is improved by more than half.

(4) A three-dimensional numerical simulation was performed to study the melting performance of ceramic foam/salt CPCMs in a shell-and-tube heat storage unit. The effects of filling height, porosity, and outer diameter of ceramic foam were analysed and compared. As the filling height increases, thermal energy is stored faster. However, the effect of the filling height is different: when the ceramic foam reaches the inner tube, the enhancement performance is remarkable; otherwise, it is insignificant. A new criterion, which is called the normalised effective porosity, was used to compare the influence of filling height, outer diameter, and porosity. The ceramic foam with varying outer diameters is optimal in the melting rate, total stored energy, and energy storage rate.

(5) The thermal performance under solar fluctuation was studied to understand the practical energy storage process. A sunny day and cloudy day in Nottingham, the UK were selected, and the charging over the whole working hours (6:00-20:00) was analysed. For the full charging cases, the total stored energy is different according to solar fluctuation, with a maximum difference of 17.9%. Strong solar radiation not only improves the energy storage rate but also increases the total stored energy. Rising solar radiation can also cause large total stored energy while the energy storage rate is low. Oscillating solar radiation results in the smallest total stored energy, whilst the energy storage rate is higher than that under rising solar radiation. Compared to pure salt, the CPCM is more sensitive to solar fluctuation. The total stored energy over the whole working hours is improved by 33.2% on a sunny day and 29.1% on a cloudy day respectively.

9.2 Outlook

This thesis shows a comprehensive study on the thermal transport in a novel ceramic foam/salt composite phase change material. Some work needs to be done in the future to better understand the thermal transport and pave the way for potential large-scale applications.

- More application scenarios should be included, such as industrial waste heat recovery. The thermal conditions in different scenarios are different. The thermal transport performance of the porous CPCM needs to be analysed in more scenarios and detailed energy storage information be provided.
- The performance at higher temperature needs to be evaluated. The current test temperature is ~300 °C. Some applications work at high temperature, like 500 °C or higher. The ceramic foam should be tested at high temperature to make sure its feasibility in high-temperature applications.
- The role of CPCM in the whole system should be assessed. Actually, the thermal energy storage system does not work alone many times. Instead, it is integrated as a component in the whole application system. For example, in the solar power generation system, the effect of the CPCM on the output power and the system efficiency could be evaluated and the system could be optimised.
- The performance in low-temperature applications such as household heating systems can be discussed and some practical factors (day/night, season, etc) needs to be taken into account.

The above recommendations focus more on the application aspect. They should be able to provide reasonable guidelines for future studies on the thermal transport in the porous CPCM. They would contribute to further recognising the potential of the porous CPCM in applications.

References

[1] H. Zhang, J. Baeyens, G. Cáceres, J. Degreve, Y. Lv, Thermal energy storage: Recent developments and practical aspects, Progress in Energy and Combustion Science, 53 (2016) 1-40.

[2] bp Statistical Review of World Energy 2021, https://www.bp.com/content/dam/bp/business-sites/en/global/corporate/pdfs/energy-economics/statistical-review/bp-stats-review-2021-full-report.pdf.

[3] L.F. Cabeza, Advances in thermal energy storage systems: methods and applications, Woodhead Publishing, 2021.

[4] G. Alva, Y. Lin, G. Fang, An overview of thermal energy storage systems, Energy, 144 (2018) 341-378.

[5] Y. Zhang, G. Zhou, K. Lin, Q. Zhang, H. Di, Application of latent heat thermal energy storage in buildings: State-of-the-art and outlook, Building and Environment, 42 (2007) 2197-2209.

[6] L. Miró, J. Gasia, L.F. Cabeza, Thermal energy storage (TES) for industrial waste heat (IWH) recovery: A review, Applied Energy, 179 (2016) 284-301.

[7] Q. Zhang, Z. Wang, X. Du, G. Yu, H. Wu, Dynamic simulation of steam generation system in solar tower power plant, Renewable Energy, 135 (2019) 866-876.

[8] S. Ručevskis, P. Akishin, A. Korjakins, Parametric analysis and design optimisation of PCM thermal energy storage system for space cooling of buildings, Energy and Buildings, 224 (2020) 110288.

[9] U.S. Department of Energy: Concentrating Solar Power (CSP) Technologies, 2022, https://solareis.anl.gov/guide/solar/csp/.

[10] A. Castell, I. Martorell, M. Medrano, G. Pérez, L.F. Cabeza, Experimental study of using PCM in brick constructive solutions for passive cooling, Energy and Buildings, 42 (2010) 534-540.

[11] S. Zhang, D. Feng, L. Shi, L. Wang, Y. Jin, L. Tian, Z. Li, G. Wang, L. Zhao, Y. Yan, A review of phase change heat transfer in shape-stabilized phase change materials (ss-PCMs) based on porous supports for thermal energy storage, Renewable and Sustainable Energy Reviews, 135 (2021) 110127.

[12] W. Wang, X. He, Y. Shuai, J. Qiu, Y. Hou, Q. Pan, Experimental study on thermal performance of a novel medium-high temperature packed-bed latent heat storage system containing binary nitrate, Applied Energy, 309 (2022) 118433.

[13] A. Sharma, V.V. Tyagi, C.R. Chen, D. Buddhi, Review on thermal energy storage with phase change materials and applications, Renewable and sustainable energy reviews, 13 (2009) 318-345.

[14] M. Liu, W. Saman, F. Bruno, Review on storage materials and thermal performance enhancement techniques for high temperature phase change thermal storage systems, Renewable and Sustainable Energy Reviews, 16 (2012) 2118-2132.

[15] L.F. Cabeza, Advances in thermal energy storage systems: Methods and applications, Woodhead Publishing, Cambridge, 2015.

[16] D. Aydin, S.P. Casey, S. Riffat, The latest advancements on thermochemical heat storage systems, Renewable and Sustainable Energy Reviews, 41 (2015) 356-367.

[17] L. Shao, A. Raghavan, G.-H. Kim, L. Emurian, J. Rosen, M.C. Papaefthymiou, T.F. Wenisch, M.M.K. Martin, K.P. Pipe, Figure-of-merit for phase-change materials used in thermal management, International Journal of Heat and Mass Transfer, 101 (2016) 764-771.

[18] S.A. Mohamed, F.A. Al-Sulaiman, N.I. Ibrahim, M.H. Zahir, A. Al-Ahmed, R. Saidur, B.S. Yılbaş, A.Z. Sahin, A review on current status and challenges of inorganic phase change materials for thermal energy storage systems, Renewable and Sustainable Energy Reviews, 70 (2017) 1072-1089.

[19] P. Zhang, X. Xiao, Z.W. Ma, A review of the composite phase change materials: Fabrication, characterization, mathematical modeling and application to performance enhancement, Applied Energy, 165 (2016) 472-510.

[20] Y. Lin, Y. Jia, G. Alva, G. Fang, Review on thermal conductivity enhancement, thermal properties and applications of phase change materials in thermal energy storage, Renewable and Sustainable Energy Reviews, 82 (2018) 2730-2742.

[21] Y. Yao, H. Wu, Macroscale Modeling of Solid–Liquid Phase Change in Metal Foam/Paraffin Composite: Effects of Paraffin Density Treatment, Thermal Dispersion, and Interstitial Heat Transfer, Journal of Thermal Science and Engineering Applications, 13 (2021).

[22] N.I. Ibrahim, F.A. Al-Sulaiman, S. Rahman, B.S. Yilbas, A.Z. Sahin, Heat transfer enhancement of phase change materials for thermal energy storage applications: A critical review, Renewable and Sustainable Energy Reviews, 74 (2017) 26-50.

[23] A. Gautam, R.P. Saini, A review on sensible heat based packed bed solar thermal energy storage system for low temperature applications, Solar Energy, 207 (2020) 937-956.

[24] G. Alva, L. Liu, X. Huang, G. Fang, Thermal energy storage materials and systems for solar energy applications, Renewable and Sustainable Energy Reviews, 68 (2017) 693-706.

[25] Y. Jemmal, N. Zari, M. Maaroufi, Thermophysical and chemical analysis of gneiss rock as low cost candidate material for thermal energy storage in concentrated solar power plants, Solar Energy Materials and Solar Cells, 157 (2016) 377-382.

[26] A. Anagnostopoulos, A. Alexiadis, Y. Ding, Molecular dynamics simulation of solar salt (NaNO3-KNO3) mixtures, Solar Energy Materials and Solar Cells, 200 (2019) 109897.

[27] J.C. Choi, S.D. Kim, Heat-transfer characteristics of a latent heat storage system using MgCl2 · 6H2O, Energy, 17 (1992) 1153-1164.

[28] S. Tiari, S. Qiu, Three-dimensional simulation of high temperature latent heat thermal energy storage system assisted by finned heat pipes, Energy Conversion and Management, 105 (2015) 260-271.

[29] C. Zhang, J. Li, Y. Chen, Improving the energy discharging performance of a latent heat storage (LHS) unit using fractal-tree-shaped fins, Applied Energy, 259 (2020) 114102.

[30] Z. Liu, Z. Liu, J. Guo, F. Wang, X. Yang, J. Yan, Innovative ladder-shaped fin design on a latent heat storage device for waste heat recovery, Applied Energy, 321 (2022) 119300.

[31] M. Fang, G. Chen, Effects of different multiple PCMs on the performance of a latent thermal energy storage system, Applied Thermal Engineering, 27 (2007) 994-1000.

[32] C.J. Ho, J.Y. Gao, An experimental study on melting heat transfer of paraffin dispersed with Al2O3 nanoparticles in a vertical enclosure, International Journal of Heat and Mass Transfer, 62 (2013) 2-8.

[33] M.-H. Sun, S.-Z. Huang, L.-H. Chen, Y. Li, X.-Y. Yang, Z.-Y. Yuan, B.-L. Su, Applications of hierarchically structured porous materials from energy storage and conversion, catalysis, photocatalysis, adsorption, separation, and sensing to biomedicine, Chemical Society Reviews, 45 (2016) 3479-3563.

[34] P. Zhang, Z.N. Meng, H. Zhu, Y.L. Wang, S.P. Peng, Melting heat transfer characteristics of a composite phase change material fabricated by paraffin and metal foam, Applied Energy, 185 (2017) 1971-1983.

[35] J.A. Weaver, R. Viskanta, Freezing of water saturated porous media in a rectangular cavity, International Communications in Heat and Mass Transfer, 13 (1986) 245-252.

[36] P. Zhang, X. Xiao, Z.N. Meng, M. Li, Heat transfer characteristics of a molten-salt thermal energy storage unit with and without heat transfer enhancement, Applied Energy, 137 (2015) 758-772.

[37] G. Righetti, R. Lazzarin, M. Noro, S. Mancin, Phase change materials embedded in porous matrices for hybrid thermal energy storages: Experimental results and modeling, International Journal of Refrigeration, 106 (2019) 266-277.

[38] A. Mallow, O. Abdelaziz, S. Graham, Thermal charging performance of enhanced phase change material composites for thermal battery design, International Journal of Thermal Sciences, 127 (2018) 19-28.

[39] H.-Q. Jin, L.-W. Fan, M.-J. Liu, Z.-Q. Zhu, Z.-T. Yu, A pore-scale visualized study of melting heat transfer of a paraffin wax saturated in a copper foam: effects of the pore size, International Journal of Heat and Mass Transfer, 112 (2017) 39-44.

[40] X. Xiao, P. Zhang, M. Li, Preparation and thermal characterization of paraffin/metal foam composite phase change material, Applied Energy, 112 (2013) 1357-1366.

[41] J.A. Weaver, R. Viskanta, Melting of frozen, porous media contained in a horizontal or a vertical, cylindrical capsule, International Journal of Heat and Mass Transfer, 29 (1986) 1943-1951.

[42] C. Beckermann, R. Viskanta, Natural convection solid/liquid phase change in porous media, International Journal of Heat and Mass Transfer, 31 (1988) 35-46.

[43] C.Y. Zhao, W. Lu, Y. Tian, Heat transfer enhancement for thermal energy storage using metal foams embedded within phase change materials (PCMs), Solar Energy, 84 (2010) 1402-1412.

[44] Z. Chen, D. Gao, J. Shi, Experimental and numerical study on melting of phase change materials in metal foams at pore scale, International Journal of Heat and Mass Transfer, 72 (2014) 646-655.

[45] G.R. Jackson, T. Fisher, Response of porous foams filled with phase change material under transient heating, in: 45th AIAA Thermophysics Conference., 2015, pp. 2811.

[46] E. Fleming, S. Wen, L. Shi, A.K. da Silva, Experimental and theoretical analysis of an aluminum foam enhanced phase change thermal storage unit, International Journal of Heat and Mass Transfer, 82 (2015) 273-281.

[47] A. Atal, Y. Wang, M. Harsha, S. Sengupta, Effect of porosity of conducting matrix on a phase change energy storage device, International Journal of Heat and Mass Transfer, 93 (2016) 9-16.

[48] Z. Zhang, X. He, Three-dimensional numerical study on solid-liquid phase change within open-celled aluminum foam with porosity gradient, Applied Thermal Engineering, 113 (2017) 298-308.

[49] H. Zheng, C. Wang, Q. Liu, Z. Tian, X. Fan, Thermal performance of copper foam/paraffin composite phase change material, Energy Conversion and Management, 157 (2018) 372-381.

[50] J. Fukai, Y. Hamada, Y. Morozumi, O. Miyatake, Improvement of thermal characteristics of latent heat thermal energy storage units using carbon-fiber brushes: experiments and modeling, International Journal of Heat and Mass Transfer, 46 (2003) 4513-4525.

[51] M. Caliano, N. Bianco, G. Graditi, L. Mongibello, Analysis of a phase change material-based unit and of an aluminum foam/phase change material composite-based unit for cold thermal energy storage by numerical simulation, Applied Energy, 256 (2019) 113921.

[52] X. Yang, Q. Bai, Q. Zhang, W. Hu, L. Jin, J. Yan, Thermal and economic analysis of charging and discharging characteristics of composite phase change materials for cold storage, Applied Energy, 225 (2018) 585-599.

[53] H. Wang, F. Wang, Z. Li, Y. Tang, B. Yu, W. Yuan, Experimental investigation on the thermal performance of a heat sink filled with porous metal fiber sintered felt/paraffin composite phase change material, Applied Energy, 176 (2016) 221-232.

[54] X. Yang, P. Wei, X. Cui, L. Jin, Y.-L. He, Thermal response of annuli filled with metal foam for thermal energy storage: An experimental study, Applied Energy, 250 (2019) 1457-1467.

[55] M. Al-Jethelah, S. Ebadi, K. Venkateshwar, S.H. Tasnim, S. Mahmud, A. Dutta, Charging nanoparticle enhanced bio-based PCM in open cell metallic foams: An experimental investigation, Applied Thermal Engineering, 148 (2019) 1029-1042.

[56] H.T. Cui, Experimental investigation on the heat charging process by paraffin filled with high porosity copper foam, Applied Thermal Engineering, 39 (2012) 26-28.

[57] W.Q. Li, Z.G. Qu, B.L. Zhang, K. Zhao, W.Q. Tao, Thermal behavior of porous stainless-steel fiber felt saturated with phase change material, Energy, 55 (2013) 846-852.

[58] A. Diani, M. Campanale, Transient melting of paraffin waxes embedded in aluminum foams: Experimental results and modeling, International Journal of Thermal Sciences, 144 (2019) 119-128.

[59] K. Venkateshwar, S. Ebadi, H. Simha, S. Mahmud, Influence of Pore Density and Porosity on the Melting Process of Bio-Based Nano-Phase Change Materials Inside Open-Cell Metal Foam, Journal of Thermal Science and Engineering Applications, 11 (2019).

[60] A. Siahpush, J. O'Brien, J. Crepeau, Phase Change Heat Transfer Enhancement Using Copper Porous Foam, Journal of Heat Transfer, 130 (2008).

[61] W.Q. Li, Z.G. Qu, Y.L. He, W.Q. Tao, Experimental and numerical studies on melting phase change heat transfer in open-cell metallic foams filled with paraffin, Applied Thermal Engineering, 37 (2012) 1-9.

[62] J. Yang, L. Yang, C. Xu, X. Du, Experimental study on enhancement of thermal energy storage with phase-change material, Applied Energy, 169 (2016) 164-176.

[63] D. Zhou, C.Y. Zhao, Experimental investigations on heat transfer in phase change materials (PCMs) embedded in porous materials, Applied Thermal Engineering, 31 (2011) 970-977.

[64] R. Cozzolino, D. Chiappini, G. Bella, Experimental characterisation of a novel thermal energy storage based on open-cell copper foams immersed in organic phase change material, Energy Conversion and Management, 200 (2019) 112101.

[65] L.-W. Fan, H.-Q. Jin, Local thermal nonequilibrium during melting of a paraffin filled in an open-cell copper foam: a visualized study at the pore-scale, Journal of Heat Transfer, 139 (2017) 034505.

[66] S. Mancin, A. Diani, L. Doretti, K. Hooman, L. Rossetto, Experimental analysis of phase change phenomenon of paraffin waxes embedded in copper foams, International Journal of Thermal Sciences, 90 (2015) 79-89.

[67] Z. Wang, Z. Zhang, L. Jia, L. Yang, Paraffin and paraffin/aluminum foam composite phase change material heat storage experimental study based on thermal management of Li-ion battery, Applied Thermal Engineering, 78 (2015) 428-436.

[68] X. Xiao, P. Zhang, Numerical and experimental study of heat transfer characteristics of a shell-tube latent heat storage system: Part I–Charging process, Energy, 79 (2015) 337-350.

[69] Y. Yao, H. Wu, Z. Liu, Z. Gao, Pore-scale visualization and measurement of paraffin melting in high porosity open-cell copper foam, International Journal of Thermal Sciences, 123 (2018) 73-85.

[70] M.J. Allen, T.L. Bergman, A. Faghri, N. Sharifi, Robust heat transfer enhancement during melting and solidification of a phase change material using a combined heat pipe-metal foam or foil configuration, Journal of Heat Transfer, 137 (2015) 102301.

[71] T.-u. Rehman, H.M. Ali, Experimental investigation on paraffin wax integrated with copper foam based heat sinks for electronic components thermal cooling, International Communications in Heat and Mass Transfer, 98 (2018) 155-162.

[72] R. Baby, C. Balaji, Experimental investigations on thermal performance enhancement and effect of orientation on porous matrix filled PCM based heat sink, International Communications in Heat and Mass Transfer, 46 (2013) 27-30.

[73] M. Martinelli, F. Bentivoglio, A. Caron-Soupart, R. Couturier, J.-F. Fourmigue, P. Marty, Experimental study of a phase change thermal energy storage with copper foam, Applied Thermal Engineering, 101 (2016) 247-261.

[74] Q. Liu, X.-B. Feng, Y.-L. He, C.-W. Lu, Q.-H. Gu, Three-dimensional multiple-relaxation-time lattice Boltzmann models for single-phase and solid-liquid phase-change heat transfer in porous media at the REV scale, Applied Thermal Engineering, 152 (2019) 319-337.

[75] Y.-L. He, Q. Liu, Q. Li, W.-Q. Tao, Lattice Boltzmann methods for single-phase and solid-liquid phase-change heat transfer in porous media: A review, International Journal of Heat and Mass Transfer, 129 (2019) 160-197.

[76] Q. Ma, Z. Chen, H. Liu, Multiple-relaxation-time lattice Boltzmann simulation for flow, mass transfer, and adsorption in porous media, Physical Review E, 96 (2017) 013313.

[77] S. Krishnan, J.Y. Murthy, S.V. Garimella, A two-temperature model for solid-liquid phase change in metal foams, Journal of Heat Transfer, 127 (2005) 995-1004

[78] Z. Chen, M. Gu, D. Peng, Heat transfer performance analysis of a solar flat-plate collector with an integrated metal foam porous structure filled with paraffin, Applied Thermal Engineering, 30 (2010) 1967-1973.

[79] Y. Tian, C.Y. Zhao, A numerical investigation of heat transfer in phase change materials (PCMs) embedded in porous metals, Energy, 36 (2011) 5539-5546.

[80] Z.G. Qu, W.Q. Li, W.Q. Tao, Numerical model of the passive thermal management system for high-power lithium ion battery by using porous metal foam saturated with phase change material, International Journal of Hydrogen Energy, 39 (2014) 3904-3913.

[81] P.V.S.S. Srivatsa, R. Baby, C. Balaji, Numerical Investigation of PCM Based Heat Sinks with Embedded Metal Foam/Crossed Plate Fins, Numerical Heat Transfer, Part A: Applications, 66 (2014) 1131-1153.

[82] J. Yang, L. Yang, C. Xu, X. Du, Numerical analysis on thermal behavior of solid–liquid phase change within copper foam with varying porosity, International Journal of Heat and Mass Transfer, 84 (2015) 1008-1018.

[83] X. Hu, H. Wan, S.S. Patnaik, Numerical modeling of heat transfer in open-cell micro-foam with phase change material, International Journal of Heat and Mass Transfer, 88 (2015) 617-626.

[84] F. Zhu, C. Zhang, X. Gong, Numerical analysis and comparison of the thermal performance enhancement methods for metal foam/phase change material composite, Applied Thermal Engineering, 109 (2016) 373-383.

[85] F. Zhu, C. Zhang, X. Gong, Numerical analysis on the energy storage efficiency of phase change material embedded in finned metal foam with graded porosity, Applied Thermal Engineering, 123 (2017) 256-265.

[86] X. Yang, Q. Bai, Z. Guo, Z. Niu, C. Yang, L. Jin, T.J. Lu, J. Yan, Comparison of direct numerical simulation with volume-averaged method on composite phase change materials for thermal energy storage, Applied Energy, 229 (2018) 700-714.

[87] Y. Zhao, C.Y. Zhao, Z.G. Xu, H.J. Xu, Modeling metal foam enhanced phase change heat transfer in thermal energy storage by using phase field method, International Journal of Heat and Mass Transfer, 99 (2016) 170-181.

[88] V. Joshi, M.K. Rathod, Thermal performance augmentation of metal foam infused phase change material using a partial filling strategy: An evaluation for fill height ratio and porosity, Applied Energy, 253 (2019) 113621.

[89] K. Lafdi, O. Mesalhy, A. Elgafy, Graphite foams infiltrated with phase change materials as alternative materials for space and terrestrial thermal energy storage applications, Carbon, 46 (2008) 159-168.

[90] Y. Xu, Q. Ren, Z.-J. Zheng, Y.-L. He, Evaluation and optimization of melting performance for a latent heat thermal energy storage unit partially filled with porous media, Applied Energy, 193 (2017) 84-95.

[91] Z. Liu, Y. Yao, H. Wu, Numerical modeling for solid–liquid phase change phenomena in porous media: Shell-and-tube type latent heat thermal energy storage, Applied Energy, 112 (2013) 1222-1232.

[92] K. Nithyanandam, R. Pitchumani, Computational Studies on Metal Foam and Heat Pipe Enhanced Latent Thermal Energy Storage, Journal of Heat Transfer, 136 (2014).

[93] X. Yang, J. Yu, Z. Guo, L. Jin, Y.-L. He, Role of porous metal foam on the heat transfer enhancement for a thermal energy storage tube, Applied Energy, 239 (2019) 142-156.

[94] P.T. Sardari, H.I. Mohammed, D. Giddings, G.S. walker, M. Gillott, D. Grant, Numerical study of a multiple-segment metal foam-PCM latent heat storage unit: Effect of porosity, pore density and location of heat source, Energy, 189 (2019) 116108.

[95] J.M. Mahdi, E.C. Nsofor, Melting enhancement in triplex-tube latent heat energy storage system using nanoparticles-metal foam combination, Applied Energy, 191 (2017) 22-34.

[96] Q. Li, K.H. Luo, Q.J. Kang, Y.L. He, Q. Chen, Q. Liu, Lattice Boltzmann methods for multiphase flow and phase-change heat transfer, Progress in Energy and Combustion Science, 52 (2016) 62-105.

[97] D. Gao, Z. Chen, Lattice Boltzmann simulation of natural convection dominated melting in a rectangular cavity filled with porous media, International Journal of Thermal Sciences, 50 (2011) 493-501.

[98] G.R. McNamara, G. Zanetti, Use of the Boltzmann equation to simulate lattice-gas automata, Physical Review Letters, 61 (1988) 2332.

[99] K. Luo, F.-J. Yao, H.-L. Yi, H.-P. Tan, Lattice Boltzmann simulation of convection melting in complex heat storage systems filled with phase change materials, Applied Thermal Engineering, 86 (2015) 238-250.

[100] W. Zhao, Y. Zhang, B. Xu, P. Li, Z. Wang, S. Jiang, Multiple-Relaxation-Time Lattice Boltzmann Simulation of Flow and Heat Transfer in Porous Volumetric Solar Receivers, Journal of Energy Resources Technology, 140 (2018) 082003.

[101] X. Li, T. Ma, J. Liu, H. Zhang, Q. Wang, Pore-scale investigation of gravity effects on phase change heat transfer characteristics using lattice Boltzmann method, Applied Energy, 222 (2018) 92-103.

[102] Morten, Dan, Tan, Zhong, Lin, Willatzen, Prediction of strong piezoelectricity in 3R-MoS2 multilayer structures, Nano Energy, (2019).

[103] X. Li, Z. Zhu, Z. Xu, T. Ma, H. Zhang, J. Liu, Q. Wang, Effect of supergravity on heat transfer characteristics of PCM with the pore-scale lattice Boltzmann method, Energy Procedia, 158 (2019) 4641-4647.

[104] Q. Ren, F. Meng, P. Guo, A comparative study of PCM melting process in a heat pipe-assisted LHTES unit enhanced with nanoparticles and metal foams by immersed boundary-lattice Boltzmann method at pore-scale, International Journal of Heat and Mass Transfer, 121 (2018) 1214-1228.

[105] Q. Ren, Y.-L. He, K.-Z. Su, C.L. Chan, Investigation of the effect of metal foam characteristics on the PCM melting performance in a latent heat thermal energy storage unit by pore-scale lattice Boltzmann modeling, Numerical Heat Transfer, Part A: Applications, 72 (2017) 745-764.

[106] Y. Huo, Y. Guo, Z. Rao, Investigation on the thermal performance of phase change material/porous medium-based battery thermal management in pore scale, International Journal of Energy Research, 43 (2019) 767-778.

[107] W. Song, Y. Zhang, B. Li, X. Fan, A lattice Boltzmann model for heat and mass transfer phenomena with phase transformations in unsaturated soil during freezing process, International Journal of Heat and Mass Transfer, 94 (2016) 29-38.

[108] S. Jayaraman, A.P. Thompson, O.A. von Lilienfeld, E.J. Maginn, Molecular simulation of the thermal and transport properties of three alkali nitrate salts, Industrial & Engineering Chemistry Research, 49 (2010) 559-571.

[109] H. Ni, J. Wu, Z. Sun, G. Lu, J. Yu, Molecular simulation of the structure and physical properties of alkali nitrate salts for thermal energy storage, Renewable Energy, 136 (2019) 955-967.

[110] G. Qiao, M. Lasfargues, A. Alexiadis, Y. Ding, Simulation and experimental study of the specific heat capacity of molten salt based nanofluids, Applied Thermal Engineering, 111 (2017) 1517-1522.

[111] J. Ding, G. Pan, L. Du, J. Lu, X. Wei, J. Li, W. Wang, J. Yan, Theoretical prediction of the local structures and transport properties of binary alkali chloride salts for concentrating solar power, Nano Energy, 39 (2017) 380-389.

[112] D. Chen, T.S. Totton, J.W.J. Akroyd, S. Mosbach, M. Kraft, Size-dependent melting of polycyclic aromatic hydrocarbon nano-clusters: A molecular dynamics study, Carbon, 67 (2014) 79-91.

[113] G. Höhne, W.F. Hemminger, H.-J. Flammersheim, Differential Scanning Calorimetry, Springer-Verlag, Berlin, 2003.

[114] H. Loulijat, H. Zerradi, S. Mizani, E.m. Achhal, A. Dezairi, S. Ouaskit, The behavior of the thermal conductivity near the melting temperature of copper nanoparticle, Journal of Molecular Liquids, 211 (2015) 695-704.

[115] X. Xiao, P. Zhang, M. Li, Thermal characterization of nitrates and nitrates/expanded graphite mixture phase change materials for solar energy storage, Energy Conversion and Management, 73 (2013) 86-94.

[116] K. Coscia, T. Elliott, S. Mohapatra, A. Oztekin, S. Neti, Binary and Ternary Nitrate Solar Heat Transfer Fluids, Journal of Solar Energy Engineering, 135 (2013).

[117] X. Zhang, J. Tian, K. Xu, Y. Gao, Thermodynamic evaluation of phase equilibria in NaNO 3-KNO 3 system, Journal of phase equilibria, 24 (2003) 441-446.

[118] W.D. Callister, Fundamentals of materials Science and Engineering, John Wiley & Sons, New York, 2001.

[119] R.P. Feynman, R.B. Leighton, M. Sands, The Feynman Lecture on Physics, Addison Wesley Longman, Massachusetts, 1963.

[120] D. Lee, B. Jo, Thermal energy storage characteristics of binary molten salt nanofluids: Specific heat and latent heat, International Journal of Energy Research, 45 (2021) 3231-3241.

[121] A. Awad, H. Navarro, Y. Ding, D. Wen, Thermal-physical properties of nanoparticle-seeded nitrate molten salts, Renewable Energy, 120 (2018) 275-288.

[122] P.D. Myers Jr, T.E. Alam, R. Kamal, D.Y. Goswami, E. Stefanakos, Nitrate salts doped with CuO nanoparticles for thermal energy storage with improved heat transfer, Applied Energy, 165 (2016) 225-233.

[123] B.D. Iverson, S.T. Broome, A.M. Kruizenga, J.G. Cordaro, Thermal and mechanical properties of nitrate thermal storage salts in the solid-phase, Solar Energy, 86 (2012) 2897-2911.

[124] F. Ren, Z. Wang, Z. Ma, J. Su, F. Li, L. Wang, Effects of Fe2O3 concentration on microstructures and properties of SiC-based ceramic foams, Materials Science and Engineering: A, 515 (2009) 113-116.

[125] F. Motte, Q. Falcoz, E. Veron, X. Py, Compatibility tests between Solar Salt and thermal storage ceramics from inorganic industrial wastes, Applied Energy, 155 (2015) 14-22.

[126] I. Ortega-Fernández, Y. Grosu, A. Ocio, P.L. Arias, J. Rodríguez-Aseguinolaza, A. Faik, New insights into the corrosion mechanism between molten nitrate salts and ceramic materials for packed bed thermocline systems: A case study for steel slag and Solar salt, Solar Energy, 173 (2018) 152-159.

[127] K. Chenoweth, A.C.T. van Duin, W.A. Goddard, ReaxFF Reactive Force Field for Molecular Dynamics Simulations of Hydrocarbon Oxidation, The Journal of Physical Chemistry A, 112 (2008) 1040-1053.

[128] K.D. Nielson, A.C.T. Van Duin, J. Oxgaard, W.-Q. Deng, W.A. Goddard, Development of the ReaxFF reactive force field for describing transition metal catalyzed reactions, with application to the initial stages of the catalytic formation of carbon nanotubes, The Journal of Physical Chemistry A, 109 (2005) 493-499.

[129] D. Kumar, V. Jain, B. Rai, Capturing the synergistic effects between corrosion inhibitor molecules using density functional theory and ReaxFF simulations - A case for benzyl azide and butyn-1-ol on Cu surface, Corrosion Science, 195 (2022) 109960.

[130] S. Bhoi, T. Banerjee, K. Mohanty, Molecular dynamic simulation of spontaneous combustion and pyrolysis of brown coal using ReaxFF, Fuel, 136 (2014) 326-333.

[131] O. Assowe, O. Politano, V. Vignal, P. Arnoux, B. Diawara, O. Verners, A.C.T. van Duin, Reactive Molecular Dynamics of the Initial Oxidation Stages of Ni(111) in Pure Water: Effect of an Applied Electric Field, The Journal of Physical Chemistry A, 116 (2012) 11796-11805.

[132] J. Xi, H. Jiang, C. Liu, D. Morgan, I. Szlufarska, Corrosion of Si, C, and SiC in molten salt, Corrosion Science, 146 (2019) 1-9.

[133] D. Hu, T. Gu, Z. Cui, S. Vollebregt, X. Fan, G. Zhang, J. Fan, Insights into the high-sulphur aging of sintered silver nanoparticles: An experimental and ReaxFF study, Corrosion Science, 192 (2021) 109846.

[134] D.A. Newsome, D. Sengupta, H. Foroutan, M.F. Russo, A.C.T. van Duin, Oxidation of Silicon Carbide by O2 and H2O: A ReaxFF Reactive Molecular Dynamics Study, Part I, The Journal of Physical Chemistry C, 116 (2012) 16111-16121.

[135] U. Soy, A. Demir, F. Caliskan, Effect of Bentonite Addition on Fabrication of Reticulated Porous SiC Ceramics for Liquid Metal Infiltration, Ceramics International, 37 (2011) 15-19.

[136] V.A. Izhevskyi, L.A. Genova, J.C. Bressiani, A.H.A. Bressiani, silicon carbide. Structure, properties and processing, Cerâmica, 46 (2000) 4-13.

[137] H. Tanaka, Y. Uemura, Y. Inomata, Observations of holes around dislocation core in SiC crystal, Journal of Crystal Growth, 53 (1981) 630-632.

[138] Q. Fan, C. Chai, Q. Wei, P. Zhou, Y. Yang, Elastic anisotropy and electronic properties of Si3N4 under pressures, AIP Advances, 6 (2016) 085207.

[139] H. Ohsaki, K. Miura, A. Imai, M. Tada, M.A. Aegerter, Structural analysis of SiO 2 gel films by high energy electron diffraction, Journal of Sol-Gel Science and Technology, 2 (1994) 245-249.

[140] H.-z. Chen, B.-r. Li, B. Wen, Q. Ye, N.-q. Zhang, Corrosion resistance of iron-chromium-aluminium steel in eutectic molten salts under thermal cycling conditions, Corrosion Science, 173 (2020) 108798.

[141] Z. Li, R.C. Bradt, Thermal expansion of the cubic (3C) polytype of SiC, Journal of Materials Science, 21 (1986) 4366-4368.

[142] S. Zhang, Y. Yao, Y. Jin, Z. Shang, Y. Yan, Heat transfer characteristics of ceramic foam/molten salt composite phase change material (CPCM) for medium-temperature thermal energy storage, International Journal of Heat and Mass Transfer, 196 (2022) 123262.

[143] Y. Yao, H. Wu, Interfacial heat transfer in metal foam porous media (MFPM) under steady thermal conduction condition and extension of Lemlich foam conductivity theory, International Journal of Heat and Mass Transfer, 169 (2021) 120974.

[144] H. Shabgard, L. Song, W. Zhu, Heat transfer and exergy analysis of a novel solar-powered integrated heating, cooling, and hot water system with latent heat thermal energy storage, Energy Conversion and Management, 175 (2018) 121-131.

[145] Sodium Nitrate Price, 2022, https://www.chemicals.co.uk/sodium-nitrate.

[146] Potassium Nitrate Price, 2022, https://www.lssystems.co.uk/fertilisers-growing-media/straight-fertilisers/potassium-nitrate-npk-137-0-463-48p-25kg-bag.

[147] SiC Ceramic Foam Price, 2022, https://detail.1688.com/offer/524350993657.html.

[148] Q. Li, C. Li, Z. Du, F. Jiang, Y. Ding, A review of performance investigation and enhancement of shell and tube thermal energy storage device containing molten salt based phase change materials for medium and high temperature applications, Applied Energy, 255 (2019) 113806.

[149] X. Yang, P. Wei, X. Wang, Y.-L. He, Gradient design of pore parameters on the melting process in a thermal energy storage unit filled with open-cell metal foam, Applied Energy, 268 (2020) 115019.

[150] Q. Zhang, D. Cao, Z. Ge, X. Du, Response characteristics of external receiver for concentrated solar power to disturbance during operation, Applied Energy, 278 (2020) 115709.

[151] M. Medrano, A. Gil, I. Martorell, X. Potau, L.F. Cabeza, State of the art on high-temperature thermal energy storage for power generation. Part 2—Case studies, Renewable and Sustainable Energy Reviews, 14 (2010) 56-72.

[152] K. Vignarooban, X. Xu, A. Arvay, K. Hsu, A.M. Kannan, Heat transfer fluids for concentrating solar power systems – A review, Applied Energy, 146 (2015) 383-396.

[153] R. Ge, Q. Li, C. Li, Q. Liu, Evaluation of different melting performance enhancement structures in a shell-and-tube latent heat thermal energy storage system, Renewable Energy, (2022).

[154] J.M. Mahdi, H.I. Mohammed, E.T. Hashim, P. Talebizadehsardari, E.C. Nsofor, Solidification enhancement with multiple PCMs, cascaded metal foam and nanoparticles in the shell-and-tube energy storage system, Applied Energy, 257 (2020) 113993.

[155] J. Song, X.-s. Li, X.-d. Ren, C.-w. Gu, Performance analysis and parametric optimization of supercritical carbon dioxide (S-CO2) cycle with bottoming Organic Rankine Cycle (ORC), Energy, 143 (2018) 406-416.

[156] J. Yang, J. Li, Z. Yang, Y. Duan, Thermodynamic analysis and optimization of a solar organic Rankine cycle operating with stable output, Energy Conversion and Management, 187 (2019) 459-471.

[157] H. Yu, H. Helland, X. Yu, T. Gundersen, G. Sin, Optimal design and operation of an Organic Rankine Cycle (ORC) system driven by solar energy with sensible thermal energy storage, Energy Conversion and Management, 244 (2021) 114494.

[158] E. Casati, A. Galli, P. Colonna, Thermal energy storage for solar-powered organic Rankine cycle engines, Solar Energy, 96 (2013) 205-219.

[159] X. Li, H. Tian, G. Shu, M. Zhao, C.N. Markides, C. Hu, Potential of carbon dioxide transcritical power cycle waste-heat recovery systems for heavy-duty truck engines, Applied Energy, 250 (2019) 1581-1599.

[160] S. Zhang, Z. Li, H. Wang, L. Tian, Y. Jin, M. Alston, Y. Yan, Component-dependent thermal properties of molten salt eutectics for solar thermal energy storage: experiments, molecular simulation and applications, Applied Thermal Engineering, (2022) 118333.

[161] S. Zhang, Y. Jin, Y. Yan, Depression of melting point and latent heat of molten salts as inorganic phase change material: Size effect and mechanism, Journal of Molecular Liquids, 20 (2021) 117058.

[162] V.R. Patil, V.I. Biradar, R. Shreyas, P. Garg, M.S. Orosz, N.C. Thirumalai, Techno-economic comparison of solar organic Rankine cycle (ORC) and photovoltaic (PV) systems with energy storage, Renewable Energy, 113 (2017) 1250-1260.

[163] Z. Li, Y. Lu, R. Huang, J. Chang, X. Yu, R. Jiang, X. Yu, A.P. Roskilly, Applications and technological challenges for heat recovery, storage and utilisation with latent thermal energy storage, Applied Energy, 283 (2021) 116277.

[164] SOLCAST API Toolkit: Nottingham Solar Radiation Data, 2022, https://toolkit.solcast.com.au/weather-sites/9dc5-1c0f-02cb-9480/detail.

[165] SOLCAST validation, 2022, https://articles.solcast.com.au/en/articles/2348589-the-difference-between-estimated-actuals-and-forecasts?_ga=2.211077532.822333207.1659944259-1836839917.1652091110.

[166] X. Yu, Z. Li, Y. Lu, R. Huang, A.P. Roskilly, Investigation of organic Rankine cycle integrated with double latent thermal energy storage for engine waste heat recovery, Energy, 170 (2019) 1098-1112.

[167] S.S. Mostafavi Tehrani, Y. Shoraka, K. Nithyanandam, R.A. Taylor, Cyclic performance of cascaded and multi-layered solid-PCM shell-and-tube thermal energy storage systems: A case study of the 19.9 MWe Gemasolar CSP plant, Applied Energy, 228 (2018) 240-253.

[168] C. Prieto, L.F. Cabeza, Thermal energy storage (TES) with phase change materials (PCM) in solar power plants (CSP). Concept and plant performance, Applied Energy, 254 (2019) 113646.

[169] M. Liu, S. Riahi, R. Jacob, M. Belusko, F. Bruno, Design of sensible and latent heat thermal energy storage systems for concentrated solar power plants: Thermal performance analysis, Renewable Energy, 151 (2020) 1286-1297.

Nomenclature

CFD	Computational fluid dynamics
CMC	Carboxymethylcellulose sodium
CPCM	Composite phase change material
DNI	Direct normal irradiance
DNS	Direct numerical simulation
DSC	Differential scanning calorimetry
EDS	Energy-dispersive spectroscopy
FDM	Finite difference method
FEM	Finite element method
FVM	Finite volume method
HTF	Heat transfer fluid
LBM	Lattice Boltzmann method
LHTES	Latent heat thermal energy storage
MD	Molecular dynamics
ORC	Organic Rankine Cycle
PCM	Phase change material
PPI	Pores per inch
PTC	Parabolic trough collector
PU	Polyurethane
RDF	Radial distribution function
REV	Representative elementary volume

SEM	Scanning electron microscope
SHM	Sensible heat storage material
SHTES	Sensible heat thermal energy storage
SiC	Silicon carbide
ss-PCM	Shape-stabilised phase change material
TCTES	Thermochemical reaction storage
TES	Thermal energy storage
XRD	X-ray diffraction
A_c	Collector aperture
A_mushy	Mushy zone constant
$c_\mathrm{p,\ HTF}$	Specific heat capacity of heat transfer fluid
$c_\mathrm{p,\ PCM}$	Specific heat capacity of PCM
$c_\mathrm{p,\ ps}$	Specific heat capacity of porous skeleton
E	Total stored energy
E_bond	Bond energy
E_bulk	Buckingham potential
E_Coulomb	Coulombic energy
$E_\mathrm{H\text{-}bond}$	Hydrogen-bond energy
E_lp	Long-pair energy
E_over	Overcoordination penalty energy
E_tors	Torsion angle energy
E_under	Undercoordination penalty energy
E_val	Valence angle energy

E_{vdW}	Van der Waals energy
Ex_{in}	Input exergy
Ex_{out}	Output exergy
f_{l}	Melting fraction of the entire PCM
F_{l}	Inertial coefficient
G	Direct normal irradiance
k_{ef}	Effective thermal conductivity
$k_{\mathrm{ef,\ PCM}}$	Effective thermal conductivity of PCM
$k_{\mathrm{ef,\ ps}}$	Effective thermal conductivity of porous skeleton
k_{ps}	Thermal conductivity of porous skeleton
k_{PCM}	Thermal conductivity of PCM
K	Permeability
L	Latent heat
m_{c}	Mass flow rate of HTF
n	Total number of cells
p	Pressure
q	Charge of ion
Q_{solar}	Total solar energy absorbed by the solar collector
$r_{\mathrm{t,in}}$, $r_{\mathrm{t,out}}$	Inner and outer radius of the tube
$r_{\mathrm{u,out}}$	Outer radius of the shell-and-tube unit
t	Time
t_{m}	Complete melting time
T	Temperature

T_0	Reference temperature
T_{am}	Ambient temperature
T_{con}	Constant heating temperature
T_{i}	Initial temperature
$T_{\mathrm{in,\ HTF}}$	Temperature of HTF at the inlet of the unit
$T_{\mathrm{i}}(r, z, f_{\mathrm{l}})$	Transient temperature at (r, z)
T_{ml}	The lower limit of melting point
T_{mu}	The upper limit of melting point
$T_{\mathrm{min,\ ORC}}$	Minimum driving temperature of ORC
$T_{\mathrm{solar,\ inlet}}$	Temperature of HTF at the inlet of solar collector
$T_{\mathrm{solar,\ outlet}}$	Temperature of HTF at the outlet of solar collector
$\overline{T(f_{\mathrm{l}})}$	Average temperature of PCM at the melting fraction f_{l}
u, v	Velocity in r, z direction
$\vec{U}, \vec{u}$	Velocity vector
v_{m}	Melting rate
V_{an}	Volume of the annulus
V_{cf}	Volume of ceramic foam
V_{PCM}	Volume of phase change material
w	Energy storage rate
$\kappa_{\mathrm{tor}}, d_{\mathrm{fp}}, d_{\mathrm{fs}}$	Parameters used in calculating permeability

Greek letters

i, j	Atom *i* and *j*
ε	Porosity
ρ	Density
β	Thermal expansion coefficient
η_c	Collector efficiency
μ	Dynamic viscosity
σ	Standard deviation
φ	Melting fraction in each cell
ω	A small number (0.001) to prevent division by zero
η	Exergy efficiency

Subscripts

ef	Effective
ps	Porous skeleton